Electromagnetic Analysis of Horn Antennas in the Terahertz region

Presented by
Mairead Bevan, B.Sc.

A thesis submitted for the Degree of
Master of Science

Department of Experimental Physics
NUI Maynooth
Co. Kildare
Ireland

May 2013

Head of Department
Professor J. A. Murphy

Research Supervisor
Dr Neil Trappe

Table of Contents

Abstract

This thesis is concerned with the application of electromagnetic modelling techniques to the analysis of horn antenna characteristics over the terahertz range, 0.1 THz to 5 THz. The mode matching technique based on a scattering matrix approach to describe beam propagation in both the forward and backward direction is applied to the analysis of conical and pyramidal horn antenna both single and multi-moded, in particular the multi-moded pyramidal horn antenna array of the SAFARI instrument - a far infrared imaging spectrometer to be launched onboard the future SPICA mission. A second electromagnetic method - the finite integration technique is applied to the analysis of simple waveguide structures and characteristics associated with them through commercially available package CST. Where appropriate a quasi-optical approach to the analysis is also applied for comparison and verification of the results, namely Gaussian beam mode analysis. The underlying theory behind these analytical techniques and their implementation is provided along with descriptions of software packages used in the analysis, these are μWave Wizard a commercially available software package based on the mode matching technique, CST Microwave studio commercially available software utilising the finite integration technique and SCATTER code developed at NUI Maynooth using the mode matching technique. Gaussian beam mode propagation using both Gauss-Laguerre and Gauss-Hermite mode sets is implemented by code written within the Mathmatica environment. The effectiveness of each method in its application to particular structures to obtain accurate and computationally feasible results is discussed.

Particular effects inherent is quasi-optical systems, crosstalk and standing wave effects are analysed in addition in later chapters. These effects are analysed both experimentally using a vector network analyser and within appropriate computational models.

Acknowledgements

Firstly, I would like to thank my supervisor Dr. Neil Trappe for his guidance throughout this project. His advice during this time has been invaluable and it is very much appreciated. I would like to thank all the staff of the Experimental Physics department particularly those in the Terahertz research group - Prof. Anthony Murphy, Dr. Creidhe O'Sullivan and Dr. Marcin Gradziel - for their help during my time in Maynooth. I must also express my appreciation to the Physics department for the funding of this project and use of the facilities.

I am extremely grateful for the assistance given by the technical and administrative staff Derek Gleeson, John Kelly, David Watson, Ian McAuley, Pat Seery and Marie Galligan. And of course special thanks to Gráinne Roche for all her help over the past two years. I also wish to acknowledge the help provided by Dr. Niall McKeith, Gerard McMahon and Dr. Tully Peacocke.

My fellow postgraduates have helped me in countless ways over the past two years. I want to thank Brian, Ronan and Francis for keeping the morale up in the office as well as Enda, Robert and Donnacha for the well earned tea breaks. I must also thank the other members of the research group - Stephen D, Stephen S, Colm, Dan, Darragh and Paul - each one of whom has helped me during my time in Maynooth as well as made that time enjoyable.

A very special thank you to my family, my parents Anne and Alun and my brother Ceri for their continuous encouragement over the years. And finally I would like to thank Niall whose advice and support helped me immensely while I worked to complete this thesis.

CHAPTER 1

Introduction

1.1 Introduction - The Terahertz region

This thesis is concerned with the modelling and analysis of optical system components that operate in the terahertz region of the EM spectrum. First a definition of the terahertz region and an explanation of why it is of interest is provided here. Following sections of this chapter introduce the system components of interest, namely horn antennas and important characteristics associated with the antennas that will be discussed in detail throughout the thesis are defined. In section 1.3 a particular instrument operating within the THz range - the SPICA mission and SAFARI instrument - is introduced as part of the thesis is concerned with the analysis of the focal plane array of SAFARI and work undertaken during this project was geared towards analysis of such systems. Finally a brief overview of the following chapters is provided.

The terahertz region (THz) of the EM spectrum has no real clear definition, the stated range can vary considerably within the literature, at the extremes it can be said to extend from 0.1 - 10THz or in wavelengths 30μm - 3mm. More conservatively it is often said to range from 0.3 - 3THz as below 0.3THz millimetre wavelengths are being considered and at the high frequency end the definition is encroaching on the mid-infrared band. The term terahertz is applied to sub-millimetre waves and extends into the far-infrared. Why this region is of so much interest is it is wedged between two regions namely millimetre wave and mid-infrared waves which each have their own well established technologies, in the frequency band between them neither technology is entirely suited to the analysis of terahertz radiation. The terahertz band can be seen in figure 1.1 sandwiched between optical and electronic regimes of the EM spectrum. The terahertz band was once dubbed the "terahertz gap" due to the lack of knowledge surrounding the frequency band. This was due to technical difficulties in producing THz sources and detectors, however in the last few years

recent technological advances have overcame this problem driven by the wide range of potential applications in this area such as scanning systems used for the detection of weapons, medical applications and astrophysics to name a few. It is the latter, its application in astronomy and astrophysics that is mainly of interest here.

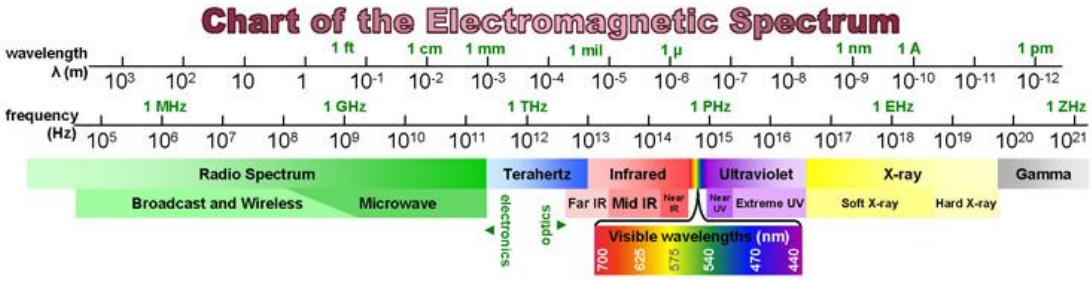

Figure 1.1 The electromagnetic spectrum [wright.edu]

More often called sub-millimetre or far-infrared astronomy (depending on the wavelength), recent developments in technology have meant many next generation telescopes are exploiting the waveband and returning unprecedented results such as the ALMA array and Herschel space observatory. Terahertz radiation is radiated by extremely cold areas of space such as the Cosmic Microwave Background (< 3K), which was first detected at sub-millimetre wavelengths in the 1960's. Mapping the CMB anisotropies with improved sensitivity has been a primary objective of the Planck surveyor launched in 2009 operating at sub-millimetre wavelengths. The Herschel space observatory was the first of its kind to span the entire far-infrared to sub-millimetre range and has been returning images of the coldest and most distant areas of the Universe since its launch in 2009 alongside Planck. Star forming regions of space and evolving galaxies radiate large portions of energy in this spectral band, future missions such as the SPICA mission discussed in more detail in section 1.3, will probe this area as terahertz radiation is ideal for looking through the ISM to areas hidden by dust absorption at other wavelengths.

1.2 Quasi-optical systems - Horn antennas

Optical systems designed to receive terahertz radiation are often called quasi-optical systems due to their nature, many of the system components are similar to those used

in conventional optical systems such as lenses and mirrors etc. but the analysis of propagation through the system must be modified to take diffraction effects into account as the wavelength of radiation is now comparable to the size of the optical components (not a problem in conventional optics as λ~nm), thus they are "quasi-optical".

While quasi-optical systems borrow components from the optical regime at frequencies higher than THz, components conventionally used in electronics are also borrowed from the lower frequency end of the spectrum, thus components from both regimes that the THz gap in wedged between are used. Much of the propagation through a quasi-optical system is through free space with lenses used to refocus the beam as it spreads out due to diffraction, many other components will also be present such as beam splitters, mirrors and polarizers. Conventional electronic instruments use wires to transmit a signal but as the frequency increases wires begin to act more like an antenna radiating much of the signals power into the surrounding space. Waveguides which are essentially hollow pipe conductors are thus employed in millimetre and sub-millimetre wave systems to combat this problem. Waveguides guide the wave propagation in a chosen direction, the wave is guided through the free space within the waveguide and confined by the guides metallic walls. Waveguides commonly used in millimetre/sub-millimetre systems can be of either rectangular or circular cross section, a thorough treatment of the field distribution within waveguides of both cross sections is provided later on in section 2.3. As much of the propagation through the system is via free space short sections of waveguide are generally used only to couple the beam to detectors, this is as the skin effect is not negligible and the waveguides small dimensions make them difficult to manufacture. While the waveguide confines the beam propagation is a chosen direction their aperture dimensions are generally quite small and thus horn antenna which are essentially flared sections of waveguide are coupled to the guide to better transmit or receive the radiation to/from free space, the horn antenna provides a better impedance match to free space as it has a larger aperture than the guide. The free space beam is guided down through the horn antenna toward the waveguide where detectors are mounted. A thorough understanding of the transmission and radiation characteristics of horn

antennas is thus needed for the analysis of quasi-optical systems. Types of horn antenna and their general characteristics are defined in the following sections.

1.2.1 Types of horn antenna

An antenna is defined by [Kraus 2002] as a transition device, or transducer, between a guided wave and a free-space wave, or vice versa. Antennas used in quasi-optical systems are aperture antennas these are antennas where the radiation characteristics are determined solely from the electric and magnetic fields across the aperture [Olver 1994], the aperture is greater than or equal to at least one wavelength. This description includes horn antenna which are the topic of this thesis. In contrast antennas with apertures smaller than the wavelength of received radiation set up currents along the antenna structure that determine the radiation characteristics, these are not of interest in quasi-optical systems and will not be discussed any further.

Figure 1.2 ***Commonly used horn antenna in quasi-optical systems [q-par.com, radiometer-physics.de, millimeterwave.com]***

As was mentioned earlier the horn antenna is essentially a flared section of waveguide, there are many different types of horn antenna of varying cross section and design. Two of the most commonly used in quasi-optical systems are the conical and pyramidal horn, shown in figure 1.2. Conical horn antenna of circular cross section may have either smooth or corrugated internal walls, both types are analysed in chapter 3. Pyramidal horn antenna of rectangular or square cross section and smooth walled are the subject of chapter 4. Other less common choices of horn antenna in quasi-optical systems are the sectoral horn (a special case of the pyramidal horn), the diagonal horn (a flared square pyramidal horn rotated 45˚ about its axis) and the dielectric-loaded horn (a conical horn partially filled with a cone of dielectric material).

Each horn has their own particular advantages and disadvantages that must be considered when designing a quasi-optical system.

Horn antenna may be either single or multi-moded, this refers to mode propagation within the waveguide feeding the horn. If the waveguide is of sufficiently small dimensions so that only one mode (the fundamental or dominant mode) will propagate within the waveguide at the throat of the horn then the horn is said to be single moded or a pure-mode horn. Horns fed by waveguides where the dimensions allow more than one mode to propagate within the guide are said to be multi- or over-moded. Multi-moded horns have the advantage that a greater signal is received at the terminals of the horn where detectors are often placed, although this also causes complications in that the detected modes will be out of phase with each other upon reaching the detector and this must be accounted for in the system analysis. Single moded horns produce radiation patterns that are determined by the fundamental mode whereas the higher order modes propagating within the feeding waveguide of a multi-moded horn as well as the fundamental mode will contribute to the horns radiation pattern, with careful design of the horn this can be used an as advantage to shape the beam pattern to be as desired. Thus both single and multi-moded horns have their own particular advantages and disadvantages. The advantages of multi-moded horns make them a common choice for many high performance systems especially far-infrared astronomical receiver systems such as the PLANCK Surveyor of which the higher frequency channel utilises multi-moded corrugated horns for foreground signal detection, the Herschel space observatory on board which the Spectral and Photometric Imaging Receiver (SPIRE) utilises multi-moded conical horns and the not yet launched SPICA mission whose far-infrared instrument, SAFARI, purposes arrays of multi-moded square aperture pyramidal horns to couple radiation to the transition edge sensors (TES) detectors. The terahertz research group at NUI Maynooth has been involved in the analysis and design of these instruments and analysis of the SAFARI focal plane array forms a large part of the topic of this thesis.

Important performance parameters of horn antennas that will be referred to throughout the thesis are defined in the following section.

1.2.2 Antenna characteristics

In the study of horn antenna an important theorem is invoked to simplify the analysis. Rayleigh's reciprocity theorem applied to horn antenna states that whether an antenna is transmitting or receiving radiation the radiation pattern characteristics are the same in both cases and the power flow is the same both ways [Kraus 2002]. This theorem is invoked throughout the thesis, horn antenna used in many quasi-optical systems may be either transmitting or receiving radiation, the models presented in the following chapters are assumed to be transmitting as it simplifies the analysis.

The radiation pattern of a horn antenna is a representation of the antennas radiated energies spatial distribution as a function of the observers position. The radiation pattern is referred to in two distinct zones depending on the observation distance from the antenna, these are the near and far-field. The near field, also called the Fresnel region is defined as the region of the field where the radiation field predominates and the angular field distribution is dependent on the distance from the antenna. As the radiation propagates further away from the antenna the angular field distribution becomes independent of the distance from the antenna, this region is called the far-field of Fraunhofer region. The definition of the two regions is dependent on the radiation wavelength λ. There is no clear boundary between the two regions, naturally there is a transition region between the two where both near and far field effects are present. For an aperture antenna the far-field region is given by distances greater than $2D^2/\lambda$ [Kraus 2002] where D is the diameter (or largest dimension) of the antenna aperture. The radiation pattern is often normalised with respect to its maximum value and the intensity of the field expressed in decibels. The radiation pattern is referred to consistently throughout the thesis and now important characteristics associated with it are defined as they will be mentioned often over the following chapters. The radiation pattern consists of lobes, the main lobe and minor side lobes which are defined by [Balanis 2005] as "portions of the radiation pattern bounded by regions of relatively weak radiation intensity", this is illustrated in figure 1.3. The main lobe is the direction of maximum radiation while the side lobes represent radiation in undesired directions, if the antenna is receiving a signal from an intended target some unwanted radiation will be received from other areas off the

target, this must be accounted for in the calibration/image processing. Antenna designers wish to minimise these side lobes as much as possible.

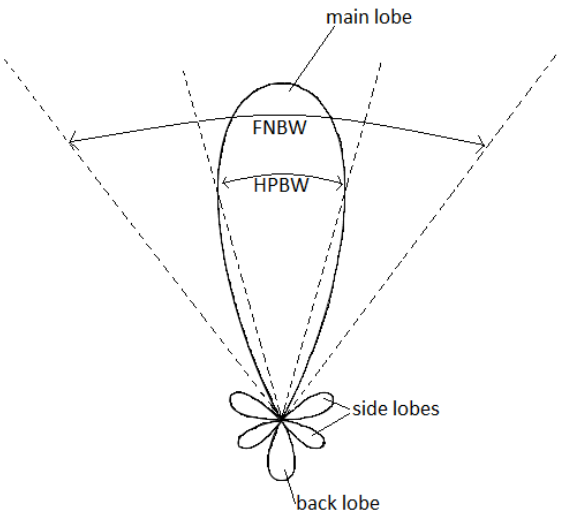

Figure 1.3 Illustration of the radiation pattern of a horn antenna

The beam width of the radiation pattern is the angular separation between two identical points on opposite sides of the pattern maximum, the half-power beam width (HPBW) and first-null beam width (FNBW) are shown in figure 1.3. The resolution capabilities of an antenna are defined by the beam width. The resolution capability of an antenna to distinguish between two sources is equal to half the first-null beam width which is approximately equal to the half-power beam width [Kraus 2002]. If the sources have an angular separation less than this they will not be resolved. There is a trade off however between the beam width and the side lobe levels, as the beam width decreases the side lobe levels increase. The bandwidth describes the frequency band over which the performance of an antenna is designed to operate at. The performance of the antenna will be to a specified standard with respect to certain characteristics such as beam width, directivity etc.

The directivity of an antenna is the ratio of the radiation intensity in a given direction from the antenna to the radiation intensity averaged over all directions. If *U* is the radiation intensity (Watts per unit solid angle) the directivity *D* is given by

$$D = \frac{U(\theta,\phi)}{U(\theta,\phi)_{avg}} = \frac{4\pi U(\theta,\phi)}{P_t} = \frac{4\pi U(\theta,\phi)}{\oiint_\Omega U d\Omega}$$

where P_t is the total radiated power in Watts. If the direction is not specified then the direction of maximum radiation is implied [Huang and Boyle 2008], generally the directivity describes how directive the main beam (lobe) is.

The polarization of an antenna is the same as the polarization of the wave it is transmitting, which is one of three types; linear, circular or elliptical. The antenna is never completely polarized in a single mode so the desired polarization is often referred to as the co-polarization whereas the cross-polarization is the undesired component which is orthogonal to the co-polarization. For example if the antenna is linearly polarized and the co-polarization is vertical the cross polarization is horizontal. Optimally designed horn antenna will have cross polarization levels as low as possible.

A summary of some of the general characteristics of commonly used horn antenna types is given in table 1.1 [Olver 1994].

Type of feed	**Shape of pattern**	**Pattern symmetry**	**Peak Cross-polarization**	**Gain**	**Efficiency**	**Band-width**	**Size and Volume**
Pure-mode horn	Gaussian	Medium	High	Medium	Medium	Medium	Medium
Multimode horn	Shaped	Medium to good	Medium to low	Medium	Medium	Medium	Medium
Corrugated horn	Gaussian	High	Very low	Medium to high	Low	Wide	Large
Dielectric-loaded horn	Gaussian	High	Very low	Medium	Medium	Wide	Large

Table 1.1 General characteristics of four commonly used horn antenna

1.3 Space Infrared Telescope for Cosmology and Astrophysics (SPICA)

SPICA is a proposed next generation mid to far infrared astronomy mission. The astronomical mission is led by JAXA (Japan Aerospace Exploration Agency) with contributions from the ESA, a European consortium and Korea. It follows on (both scientifically and technically) from a previous successful mission AKARI launched in 2006 and the ESA heritage of the Planck mission and the Herschel Space observatory.

SPICA is designed to probe galaxy, star and planetary system formation , as well as the evolution of dust and gas in the interstellar medium of both our own and distant galaxies [ESA SPICA website]. Planned for launch in 2018/2019 with a lifetime of 3 to 5 years, SPICA will have a 3.5m diameter cryogenically-cooled Ritchey-Chrétien telescope operating over the 5µm to 210µm waveband performing imaging and spectroscopic observations.

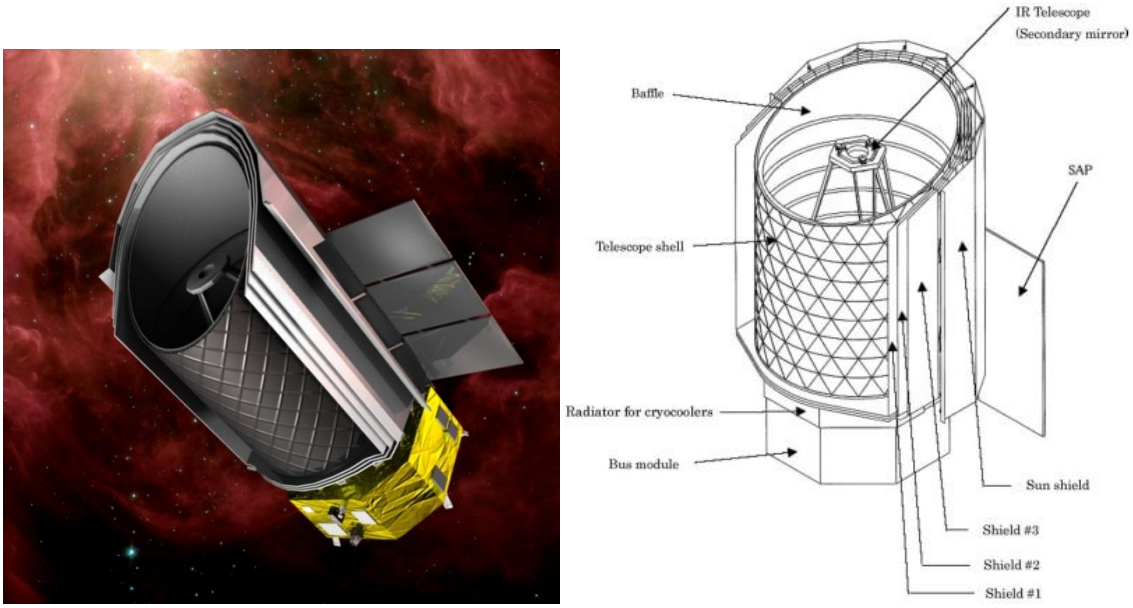

Figure 1.4 ***(Left) Artist's rendering of SPICA spacecraft, (Right) Schematic illustration of the spacecraft design [ESA SPICA website]***

The scientific objectives of SPICA are broad and diverse, it will look at the formation and evolution of planetary systems, amongst other methods using far infrared spectroscopy to examine oxygen and water lines in proto-planetary disks and the atmospheres of young gas giants to explore their role in the formation of planetary systems and habitable planets. It will look at galactic and extragalactic star forming regions hidden by dust absorption using mid and far infrared spectroscopy to detect cooling lines indicative of stellar formation. The formation and evolution of galaxies will be examined as the largest proportion of energy emitted by galaxies during their evolution is within SPICAs spectral range. Luminous infrared galaxies, high red-shift galaxies and AGNs will each be observed. The lifecycle of dust and its origin in the early Universe as well as the very nature of the cosmic infrared background will be observed.

SPICA will utilise a new kind of cooling system that will achieve superior sensitivity compared to previous missions due to its cryogenically-cooled large telescope. Warm telescopes emit infrared radiation due to their heat. This self-emitted radiation is much stronger than the astronomical diffuse radiation the telescope receives and impedes high sensitivity infrared observations. Previous missions have required large tanks of cryogen (liquid helium) to be carried on board, this increases the mass of the spacecraft while decreasing the size of the telescope. SPICA will utilise a new cooling system of effective mechanical cryocoolers and passive radiative cooling, eliminating the need for large cryogen tanks. The self-emitted thermal radiation will be reduced by a factor of a million [JAXA SPICA website] thus producing superior high sensitivity observations. SPICA will be launched at ambient temperature (a "warm launch") and cooled in orbit by the mechanical coolers on board. As SPICA will not have to carry cryogen, this allows for a large 3.5m diameter telescope providing high spatial resolution, cooled to <6K.

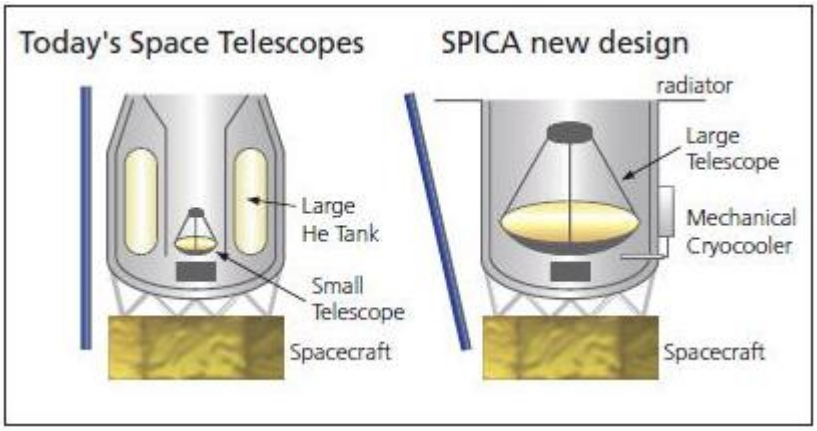

Figure 1.5 ***SPICAs novel mechanical cryocooler design compared to previous missions [JAXA SPICA website]***

SPICA has three main instruments in its payload. A mid infrared coronagraph operating over the 5 - 27µm waveband will enable observations of stellar companions such as planets and proto-planetary disks using both imaging and spectroscopy. A mid infrared camera and spectrometer will perform wide field imaging and both low and medium resolution spectroscopic observations over a wide spectral range (5 - 38µm). And SAFARI, a far infrared imaging spectrometer operating between 35 - 210µm designed to give continuous wavelength coverage in both photometric and spectroscopic modes with high spectral resolution (R ~ 10 to 10,000) and a field of

view of 2' x 2'. An analysis of components of the SAFARI focal plane array was undertaken during this project and will be described in detail in the following chapters.

SAFARI utilises a Mach-Zehnder imaging Fourier Transform Spectrometer. SAFARIs conceptual design can be seen in figure 1.6. The focal plane arrays indicated on the diagram are separated in to short (35-70µm), mid (70-110µm) and long (110-210µm) wavelength FPA units. Each wavelength band has a 2D focal plane array of 0.5 $f\lambda$ spaced pixels that will cover a 2' x 2' field of view, each unit has a diameter of 150mm and height 65mm with a total mass of 1.3kg [Mauskopf 2010].

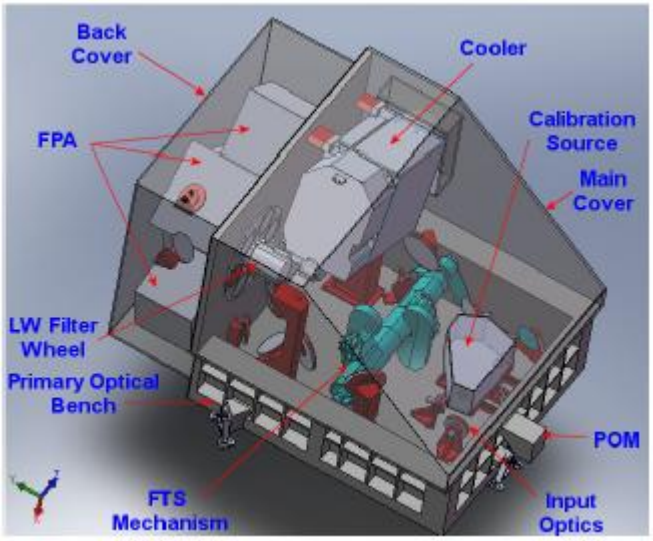

FPA	***Focal Plane Array***
FTS	***Fourier Transform Spectrometer***
POM	***Pick-Off Mirror***

Figure 1.6 Conceptual design of SAFARI focal plane [SPICA assessment study report]

The huge reduction in background power due to the cyro-cooled telescope requires extremely sensitive detectors in the focal plane array to take advantage of the reduction. The focal plane array is made up of the horn array, the detector chip, electrical interconnections and readout electronics as well as the supporting infrastructure and shielding. Each horn of the array feeds a hemispherical cavity which contains the detector with a planar absorber. The SAFARI horns are much smaller than those used for previous instruments and producing the SAFARI array has proved challenging due to their dimensions. The detectors placed in the cavity are Transition Edge Sensor (TES) bolometers. Bolometers are incoherent detectors commonly used in long-wavelength astronomy. They are broad band radiation absorbers that convert incident EM radiation in to heat and the change in temperature is detected by a sensitive thermometer. The thermometer within a TES is a thin superconducting film,

an increase in temperature increases the resistance which reduces the current flowing in the bias circuit. These small changes in current are monitored by a low impedance, low noise Superconducting Quantum Interference Device, SQUID, amplifier. The detector chip of the FPA unit is an array of TES detectors. Radiation is received by the antenna (coupling optics) where it is focused on to the absorber. A schematic of the focal plane array is shown in figure 1.7 [Mauskopf 2010]. An analysis of the S-band antenna horn array is undertaken in chapter 5.

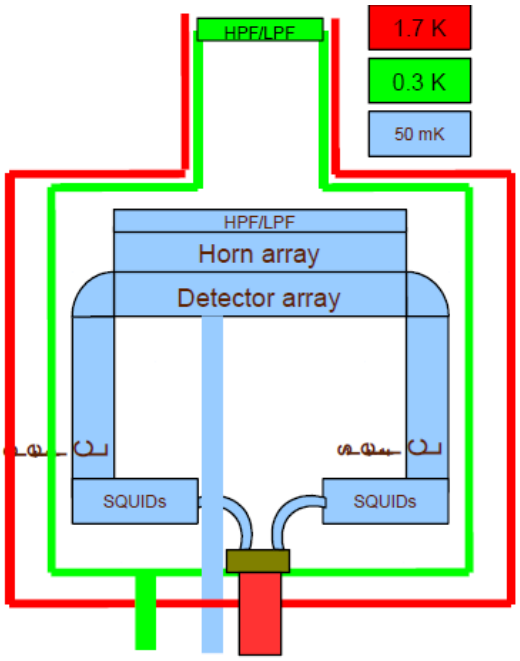

HPF	***High Pass Filter***
LPF	***Low Pass Filter***

Figure 1.7 ***Schematic of the SAFARI focal plane array unit.***

1.4 Chapter overview

Chapter 2 introduces the methods and the underlying theories behind them that are employed throughout the thesis for the analysis of horn antenna characteristics. These methods are (*i*) Gaussian Beam Mode Analysis (*ii*) the Mode Matching Technique and (iii) the Finite Integration Technique. The determination of field distributions within waveguides as well as the how to determine far-field patterns of an antenna from its aperture field are included. Following on from this, a description of the modelling software packages used throughout the analysis is provided, each one

utilising one of the previously described methods. Along with this examples of how to design and implement a model within each package are given.

Chapter 3 starts by introducing conical horns both smooth walled and corrugated. A Gaussian beam mode analysis of a smooth walled conical horn is presented to determine the propagation of a beam from the horn aperture to the far-field. Following this the more rigorous mode matching technique is applied to the analysis of the same smooth walled conical horn to determine the far-field and scattering parameters using both µWW and SCATTER code. A comparison of the methods and packages is discussed. Finally the mode matching technique is applied to the analysis of a corrugated conical horn.

Chapter 4 applies Gaussian beam mode and mode matching techniques to the analysis of pyramidal horn antenna and a discussion on the particular advantages and disadvantages of each method is presented. The SAFARI horn antenna are analysed in isolation within µWW before an analysis of crosstalk in the SAFARI array is undertaken in chapter 5.

Chapter 5 introduces the concept of arrays used in quasi-optical systems and defines mutual coupling or "crosstalk" that occurs within these arrays. Analysis of crosstalk between simple waveguide structures is presented by use of models produced in CST before results from laboratory measurements, taken with a vector network analyser, of crosstalk between waveguide structures and horn antenna over the 75 - 110GHz range are given. Finally the SAFARI array is analysed in terms of crosstalk.

Chapter 6 introduces the concept of standing waves and multiple reflections that occur in quasi-optical systems. Models and laboratory measurements of reflections within cavities formed by corrugated and pyramidal horn antenna placed aperture to aperture are given. This is extended to the analysis of the transmission and reflection properties of two identical corrugated horn antenna placed aperture to aperture when a free space gap is introduced between the two horns, this is analysed in both VNA measurements and models combining the two techniques of mode matching and GBMA to describe the beam propagation through the horn and free space.

CHAPTER 2

Theory of Analysis Techniques

2.1 Introduction

To understand the propagation of an electromagnetic beam through an optical system at sub-millimetre wavelengths an approach called quasi-optics is used as the optical components are only a few wavelengths in diameter and so diffraction effects must be taken into account. In contrast, for systems where the optical components are much larger than the wavelength, such as visual optics telescopes, conventional geometrical optics can be used as diffraction effects are negligible. Various techniques can be applied to the analysis of quasi-optical systems. During this project several software packages have been used in the analysis with differing underlying analytical techniques. This chapter gives an outline of three commonly used techniques - Gaussian Beam Mode Analysis, the Mode Matching Technique and the Finite Integration Technique which were each used during this project. Following the outline of techniques a description of the modelling software and examples of how to build and analyse simple structures in the packages are provided.

2.2 Gaussian Beam Mode Analysis

2.2.1 GBMA Introduction

Gaussian Beam Mode Analysis (GBMA) is a technique developed to accurately describe quasi-optical propagation taking Fresnel diffraction effects into account. It is widely used to propagate beams in free space through optical systems including diffractive spreading of the beam, truncation and aberration effects and optical coupling efficiency calculations. During this project GBMA was used to calculate near and far field radiation patterns of various horn antenna. In doing this GBMA assumes a scalar field in free space representing the field at the horn aperture and this can then be

propagated to the near or far field, or through an optical system in an efficient manner. GBMA is not capable of analysis of the electromagnetic behaviour of an antenna but for many well behaved examples, such as a scalar corrugated horn, the GBM technique is very useful, where the aperture field can be approximated by easily definable fields such as a truncated Bessel function of the zeroth order [Wylde 1984]

Two assumptions must be made in Gaussian Beam Mode Theory when propagating representative beams in free space, these are [Goldsmith 1998]

1. The beam propagation is quasi collimated. There is some diffraction as the beam propagates but with off axis divergence angles of no more than 30˚ (treated approximately as an infinite plane parallel wave).

2) The radiation field can be treated as a scalar field. (e.g. a truncated Bessel approximation for a corrugated horn)

2.2.2 The Paraxial Wave Equation

First consider a beam propagating through free space. This Gaussian beam originates from a source of finite size for example the aperture of a horn. The beam is largely collimated but may also have some transverse variation. The electric and magnetic fields are described respectively by the wave equations,

$$\nabla^2 \boldsymbol{E} = \mu\varepsilon \frac{\partial^2 \boldsymbol{E}}{\partial t^2} \tag{2.2.1}$$

$$\nabla^2 \boldsymbol{H} = -\frac{1}{c^2} \frac{\partial^2 \boldsymbol{H}}{\partial t^2} \tag{2.2.2}$$

If we consider monochromatic radiation and apply the second assumption of GBM theory a single component of the electromagnetic wave satisfies the Helmholtz equation,

$$\nabla^2 \psi + k^2 \psi = 0 \tag{2.2.3}$$

where $k = 2\pi/\lambda$ and ψ can be any component of ***E*** or ***H***. In rectangular coordinates the Helmholtz equation for the electric field is

$$\frac{\partial^2 E}{\partial x^2} + \frac{\partial^2 E}{\partial y^2} + \frac{\partial^2 E}{\partial z^2} + k^2 E = 0 \tag{2.2.4}$$

Although there is some variation in the beam perpendicular to the axis of propagation it can still be said that the *E* and *H* fields are perpendicular to each other and perpendicular to the direction of propagation, as with a plane wave. For a beam propagating in the positive *z* direction any component of the electric field can be written as,

$$E(x, y, z) = u(x, y, z)e^{-jkz} \tag{2.2.5}$$

where $u(x, y, z)$ is a slowly varying function with respect to *z* that defines the non-plane part of the beam. If we substitute this into the Helmholtz equation in rectangular coordinates we get

$$\frac{\partial^2 u}{\partial x^2} + \frac{\partial^2 u}{\partial y^2} + \frac{\partial^2 u}{\partial z^2} - 2jk\frac{\partial u}{\partial z} = 0 \tag{2.2.6}$$

This equation can be reduced by realising that the third term $\frac{\partial^2 u}{\partial z^2}$ is very small compared to the other terms as it is assumed the variation of the amplitude *u* along the direction of propagation is small over distances similar to the wavelength and the axial variation is small compared to the variation perpendicular to this direction. Dropping this third term we now have what is called the paraxial wave equation

$$\frac{\partial^2 u}{\partial x^2} + \frac{\partial^2 u}{\partial y^2} - 2jk\frac{\partial u}{\partial z} = 0 \tag{2.2.7}$$

The complete set of solutions to the paraxial wave equation are the Gaussian beam modes which can be expressed in either Cartesian or cylindrical coordinates, these are discussed in the following section. The choice of coordinate system used will depend on the geometry of the system for example rectangular horns are best described with Cartesian coordinates while cylindrical coordinates best describe conical horns. Numerous examples of the two geometries are found later in the thesis. In cylindrical coordinates where r represents the perpendicular distance from the *z* axis (axis of propagation) and θ is the angular coordinate, the paraxial wave equation is

$$\frac{\partial^2 u}{\partial r^2} + \frac{1}{r}\frac{\partial u}{\partial r} + \frac{1}{r}\frac{\partial^2 u}{\partial \theta^2} - 2jk\frac{\partial u}{\partial z} = 0 \tag{2.2.8}$$

where $u = u(r, \theta, z)$. Axial symmetry is displayed in many situations described by cylindrical coordinates (i.e. corrugated horns and lenses) in which case u is independent of θ and the third term in the equation above goes to zero. This gives the axially symmetric paraxial wave equation,

$$\frac{\partial^2 u}{\partial r^2} + \frac{1}{r}\frac{\partial u}{\partial r} - 2jk\frac{\partial u}{\partial z} = 0 \qquad (2.2.9)$$

2.2.3 Gaussian beam mode solutions

Solutions to the paraxial wave equation can be found in both coordinate systems. In Cartesian coordinates the solutions to the paraxial equation are Hermite Gaussian modes given by [Goldsmith 1998],

$$\Psi_{mn}(x, y, z) = h_m\left(\sqrt{2}x/_W\right) h_n\left(\sqrt{2}y/_W\right) \exp\left[-jk\left(\frac{x^2+y^2}{2R}\right) + j\phi_{mn}\right] \exp[-jkz] \qquad (2.2.10)$$

where

$$h_m\left(\sqrt{2}x/_W\right) = \frac{H_m\left(\sqrt{2}x/_W\right)\exp\left[-x^2/_{W^2}\right]}{\sqrt{2^{m-\frac{1}{2}}m!W\sqrt{\pi}}} \quad \text{and} \quad h_n\left(\sqrt{2}y/_W\right) = \frac{H_n\left(\sqrt{2}y/_W\right)\exp[-y^2/W^2]}{\sqrt{2^{n-\frac{1}{2}}n!W\sqrt{\pi}}}$$

H_m and H_n are Hermite polynomials of order *m/n* and h_m and h_n are normalised Hermite Gaussian functions.

In cylindrical coordinates solutions to the paraxial wave equation are Laguerre Gaussian modes of the form [Goldsmith 1998],

$$\Psi_n^{\alpha,cos/sin}(r, \theta, z) = \sqrt{\frac{2(2-\delta_{0n})n!}{\pi W^2(n+\alpha)!}}\left[2\left(\frac{r}{W}\right)^2\right]^{\frac{\alpha}{2}} L_n^{\alpha}\left[2\left(\frac{r}{W}\right)^2\right]\exp\left[-\left(\frac{r}{W}\right)^2\right]$$

$$\times \exp\left[-jk\left(z + \frac{r^2}{2R}\right) + j(2n+\alpha+1)\phi_0\right]\begin{pmatrix} cos\alpha\phi \\ sin\alpha\phi \end{pmatrix} \qquad (2.2.11)$$

where L_n^{α}(s) is the n^{th} associated Laguerre polynomial of order α.

In cylindrical coordinates if the modes are azimuthally symmetric, independent of θ, the Laguerre Gaussian mode set reduces to

$$\Psi_n(r,z) = \frac{1}{W}\sqrt{\frac{2}{\pi}} L_n\left(\frac{2r^2}{W^2}\right) exp\left(-\frac{r^2}{W^2}\right) exp\left(-jk\left(\frac{r^2}{2R}\right)\right) \exp\left(j\phi_0\right) \qquad (2.2.12)$$

In both coordinate systems *R* is the phase radius of curvature, *W* is the beam radius parameter and ϕ is the phase term, each are dependent on *z*, the propagation distance. $W(z)$ the beam radius or beam width is a measure of the axial extent of the beam, this is illustrated in figure 2.1.

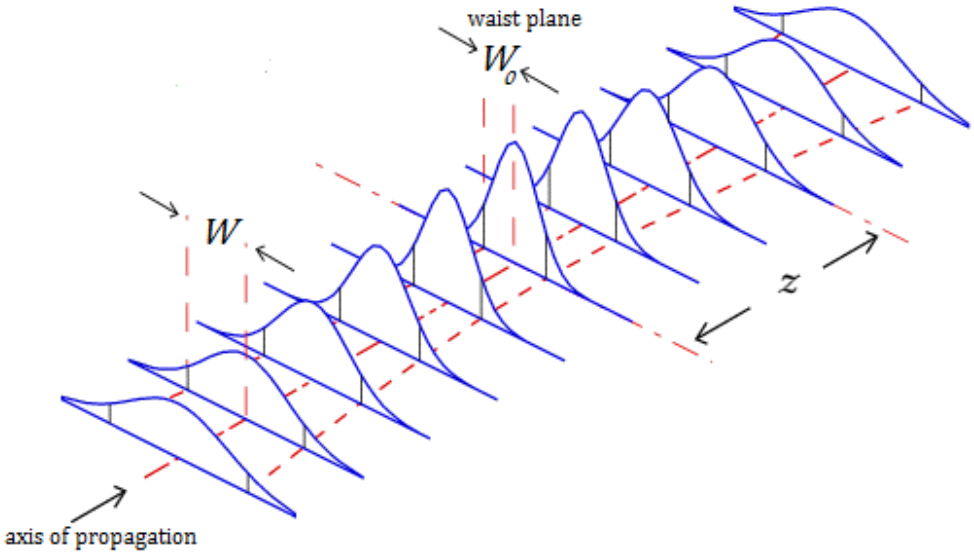

Figure 2.1 ***Gaussian beam propagation indicating the beam waist and beam width***

Its definition is the off axial distance where the field has dropped off in amplitude from its axis value by a factor of $1/e$. W_0 which is the minimum value of W is called the beam waist or beam waist radius, this occurs at $z = 0$ and the propagation distance is measured relative to the waist. W_0 is determined by the dimensions of the aperture the beam originates from. The beam width at any point is given by

$$W^2(z) = W_0^2\left[1 + \left(\frac{z\lambda}{\pi W_0^2}\right)^2\right] \qquad (2.2.13)$$

The phase radius of curvature $R(z)$ describes the equiphase surface of the beam, illustrated in figure 2.2. At the beam waist the phase radius of curvature is taken to be infinite, $R = \infty$, as the beam looks like a plane wave. As the propagation distance

increases the radius of curvature takes on a finite value and at large distances from the origin ($\gg \pi W_0/\lambda$) R begins to approach z. R is given by,

$$R(z) = z\left[1 + \left(\frac{\pi W_0^2}{\lambda z}\right)^2\right] \tag{2.2.14}$$

By convention, diverging beams are said to have positive values of R, whereas converging beams are described by a negative value of R which is approaching the beam waist.

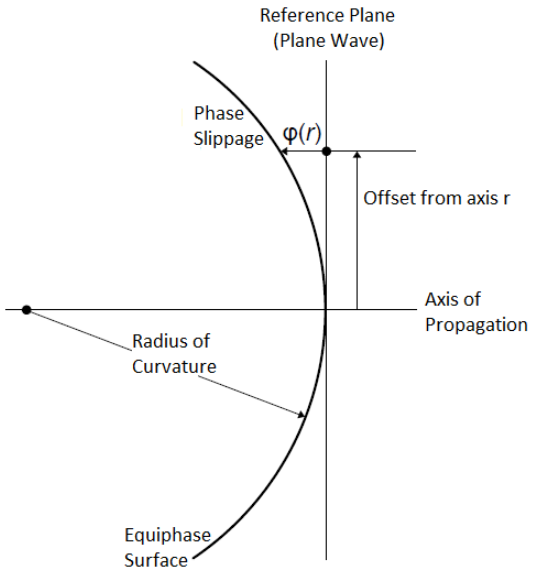

Figure 2.2 ***Illustration of the radius of curvature and phase slippage terms***

The phase slippage term ϕ is mode dependant as well as dependant on the propagation distance. ϕ_{mn} describes the on axis phase of the beam - the phase difference between a Gaussian mode and a plane wave, shown in figure 2.2. For Hermite-Gaussian modes the phase term is given by,

$$\phi_{mn}(z) = (n + m + 1)\tan^{-1}\left(\frac{\pi W^2}{\lambda R}\right) = (n + m + 1)\tan^{-1}\left(\frac{\lambda z}{\pi W_0^2}\right) \tag{2.2.15}$$

and for Laguerre-Gaussian modes it is given by,

$$\phi_{mn}(z) = (2n + m + 1)\tan^{-1}\left(\frac{\pi W^2}{\lambda R}\right) = (2n + m + 1)\tan^{-1}\left(\frac{\lambda z}{\pi W_0^2}\right) \tag{2.2.16}$$

At the origin ($z = 0$), ϕ_{mn} is zero, the modes start out in phase but as they propagate phase slippage begins to occur. For any value of *W* and *R* there exists an infinite set of free space modes which describe the beam.

2.3 Waveguide modes

Waveguides are structures commonly used in sub-millimetre/terahertz optical systems that confine a wave within the waveguide metal structure to propagate in a chosen direction with confinement in the planes transverse to the direction of propagation. Hollow conducting waveguides of circular or rectangular cross-section can be used depending on the system requirements. The guiding of the wave is achieved by a connection between the fields of the wave and the currents and charges on the boundaries of the waveguide. The distribution of the electromagnetic field within the waveguide is of interest and discussed here for the case of both cylindrical and rectangular waveguides.

First consider a waveguide where the direction of propagation is along the *z* axis. The confined wave varies with distance and time and can be described by $e^{(jwt-\gamma z)}$, where γ is the propagation constant. The propagation constant is an important term as it contains information on the waves group velocity, phase variation and attenuation along the guide. The electromagnetic fields within the guide must satisfy the wave equation and the boundary conditions. As discussed earlier (section 2.2.2) the wave equation reduces to the Helmholtz equation

$$\nabla^2 \boldsymbol{E} = -k^2 \boldsymbol{E}, \qquad \nabla^2 \boldsymbol{H} = -k^2 \boldsymbol{H} \tag{2.3.1}$$

and using separation of variables this can be separated into transverse and axial parts

$$\nabla^2 \boldsymbol{E} = \nabla_t^2 \boldsymbol{E} + \frac{\partial^2 \boldsymbol{E}}{\partial z^2} \tag{2.3.2}$$

with the assumed propagation function $e^{-\gamma z}$ in the axial direction

$$\frac{\partial^2 \boldsymbol{E}}{\partial z^2} = \gamma^2 \boldsymbol{E} \tag{2.3.3}$$

The transverse wave equations can be written

$$\nabla_t^2 \boldsymbol{E} = -(\gamma^2 + k^2)\boldsymbol{E} \tag{2.3.4}$$

$$\nabla_t^2 \boldsymbol{H} = -(\gamma^2 + k^2)\boldsymbol{H} \tag{2.3.5}$$

these equations must be satisfied within the waveguide. The boundary conditions imposed on the fields depend on the electrical properties of the boundary. If two components of the field (e.g. the *z* components of ***E*** and ***H***) are known to satisfy the wave equations and the boundary conditions the other field components (transverse) can be found from these using Maxwell's equations. The transverse components in terms of E_z and H_z are given by [Ramo, Whinnery, Van Duzer 1994]

$$E_x = -\frac{j}{k_c^2}\left(\beta \frac{\partial E_z}{\partial x} + \omega\mu \frac{\partial H_z}{\partial y}\right) \tag{2.3.6}$$

$$E_y = \frac{j}{k_c^2}\left(-\beta \frac{\partial E_z}{\partial y} + \omega\mu \frac{\partial H_z}{\partial x}\right) \tag{2.3.7}$$

$$H_x = \frac{j}{k_c^2}\left(\omega\varepsilon \frac{\partial E_z}{\partial y} - \beta \frac{\partial H_z}{\partial x}\right) \tag{2.3.8}$$

$$H_y = -\frac{j}{k_c^2}\left(\omega\varepsilon \frac{\partial E_z}{\partial x} + \beta \frac{\partial H_z}{\partial y}\right) \tag{2.3.9}$$

where $k_c^2 = \gamma^2 + k^2 = k^2 - \beta^2$

k_c is the cut off frequency. The propagation constant γ is equal to $j\beta$ for a propagating wave where β is real if there is no attenuation and imaginary for evanescent modes. The modal solutions can be classified in to four different types

- *Transverse electric* (TE) modes have a magnetic field but no electric field in the direction of propagation. So called because the electric field lies entirely in transverse planes.
- *Transverse magnetic* (TM) modes have an electric field but no magnetic field in the direction of propagation.
- *Transverse electromagnetic* (TEM) modes contain neither electric or magnetic fields in the direction of propagation.
- *Hybrid* modes, which can be considered as a coupling of TE and TM modes by the boundary. The boundary conditions require all field components.

The propagation constant describes how an individual wave changes phase and amplitude as it travels through the guide. Waves with different propagation constants can be superposed at a position and time to give the total resultant field at that point.

Many waveguides feeding horn antenna in sub-millimetre systems are designed so only one mode will propagate within the waveguide (single moded horns) even though many modes may be excited within the horn. Multi-moded horns with more than one mode propagating within the feeding waveguide may also be used in sub-millimetre systems. They have become increasingly popular in recent years in the next generation of far-infrared astronomical receiver systems such as PLANCK [***planck**.esa.int*] and the Herschel Space Observatory [***herschel**.esac.esa.int*].

2.3.1 Rectangular waveguide modes

First consider the fields within a rectangular waveguide of width *a*, height *b* and length *l*, as shown in figure 2.3.

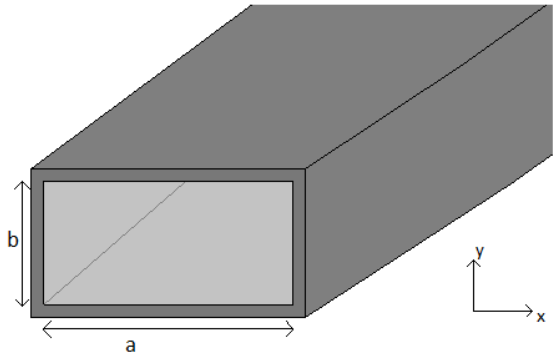

Figure 2.3 ***Rectangular waveguide geometry***

TM modes will have $H_z = 0$. The differential equation in rectangular coordinates is

$$\nabla_t^2 E_z = \frac{\partial^2 E_z}{\partial x^2} + \frac{\partial^2 E_z}{\partial y^2} = -k_c^2 E_z \tag{2.3.10}$$

by separation of variables, solutions are found to have the form [Ramo, Whinnery, Van Duzer 1994]

$$E_z = A \sin k_x x \ \sin k_y y \tag{2.3.11}$$

E_z must be zero at the waveguide wall $x = a$ and $y = b$. This is only true if $A = 0$ or $k_x x$ and $k_y y$ are integral numbers of π.

$$k_x a = m\pi, \quad m = 1, 2, 3 \ldots \tag{2.3.12}$$

$$k_y b = n\pi, \quad n = 1, 2, 3 \ldots \tag{2.3.13}$$

The cut off condition of TM waves with *m* variations in *x* and *n* variations in *y* (TM_{mn}) is

$$k_{c_{m,n}} = \left[\left(\frac{m\pi}{a}\right)^2 + \left(\frac{n\pi}{b}\right)^2\right]^{1/2} \tag{2.3.14}$$

The transverse field components of TM_{mn} modes are found from equations 2.3.6 - 2.3.9 with $H_z = 0$ and equation 2.3.11 from before

$$E_x = -\frac{j\beta k_x}{k_{c_{m,n}}^2} A \cos k_x x \ \cos k_y y \tag{2.3.15}$$

$$E_y = -\frac{j\beta k_y}{k_{c_{m,n}}^2} A \sin k_x x \ \cos k_y y \tag{2.3.16}$$

$$H_x = \frac{j\omega\varepsilon k_y}{k_{c_{m,n}}^2} A \sin k_x x \ \cos k_y y \tag{2.3.17}$$

$$H_y = -\frac{j\omega\varepsilon k_x}{k_{c_{m,n}}^2} A \cos k_x x \ \sin k_y y \tag{2.3.18}$$

Note that from equations (2.3.11 - 13) due to the sine term neither *m* nor *n* can be zero for a TM mode without the mode disappearing entirely.

TE modes will have $E_z = 0$ and non zero values for H_z so the differential equation in rectangular coordinates for TE modes is given by,

$$\nabla_t^2 H_z = \frac{\partial^2 H_z}{\partial x^2} + \frac{\partial^2 H_z}{\partial y^2} = -k_c^2 H_z \tag{2.3.19}$$

Applying the boundary conditions this is found to have solutions

$$H_z = B \cos k_x x \cos k_y y \tag{2.3.20}$$

Similar to the analysis of TM waves E_x must be equal to zero at $y = b$ and E_y equal to zero at $x = a$ so that $k_y b$ and $k_x a$ must be a multiple of π

$$k_x a = m\pi, \qquad k_y b = n\pi \tag{2.3.21}$$

In contrast to TM modes, one but not both of *m* and *n* may be zero without the mode vanishing. The transverse electric and magnetic fields are given by

$$E_x = \frac{j\omega\mu k_y}{k_{c_{m,n}}^2} B \cos k_x x \sin k_y y \tag{2.3.22}$$

$$E_y = -\frac{j\omega\mu k_x}{k_{c_{m,n}}^2} B \sin k_x x \cos k_y y \tag{2.3.23}$$

$$H_x = \frac{j\beta k_x}{k_{c_{m,n}}^2} B \sin k_x x \cos k_y y \tag{2.3.24}$$

$$H_y = \frac{j\beta k_y}{k_{c_{m,n}}^2} B \cos k_x x \sin k_y y \tag{2.3.25}$$

As k_x and k_y have the same form for TM and TE modes (equations 2.3.12, 2.3.13, 2.3.21) equation 2.3.14 applies to TE modes as well. Modes that have different field distributions but the same cut off frequencies are called degenerate modes. The dominant mode within a rectangular waveguide is the TE_{10} mode, this is the first excited mode, with the lowest cut off frequency. In many practical guides (as in chapter 4) the guide has chosen dimensions so that only the TE_{10} mode will propagate within (although more may be excited at the entrance to the guide) to avoid signal distortion caused by multimode propagation. Standard WR-10 waveguides with dimensions 2.54mm x 1.27mm are commonly used at 100GHz. The properties of the TE_{10} mode can be found from equations 2.3.19 - 2.3.24 with *m = 1* and *n = 0*, in this case $k_y = 0$ and $k_c = k_x = \pi/a$.

$$H_z = B \cos k_x x \tag{3.2.26}$$

$$E_y = -\frac{j\omega\mu\beta}{k_x} \sin k_x x \tag{3.2.27}$$

$$H_x = \frac{j\beta B}{k_x} \sin k_x x \tag{3.2.28}$$

all other terms are zero. The cut off frequency, wavelength and wavenumber are given by

$$f_c = \frac{1}{2a\sqrt{\mu\varepsilon}}, \quad \lambda_c = 2a, \quad k_c = \frac{\pi}{a} \tag{3.2.29}$$

2.3.2 Circular waveguide modes

Modes within circular waveguides are now considered, a circular cylindrical guide is shown in figure 2.4. The transverse components of the fields within the guide in cylindrical coordinates are given by

$$E_r = -\frac{j}{k_c^2}\left(\beta \frac{\partial E_z}{\partial r} + \frac{\omega\mu}{r} \frac{\partial H_z}{\partial \phi}\right) \tag{2.3.30}$$

$$E_\phi = \frac{j}{k_c^2}\left(-\frac{\beta}{r}\frac{\partial E_z}{\partial \phi} + \omega\mu\frac{\partial H_z}{\partial r}\right) \quad (2.3.31)$$

$$H_r = \frac{j}{k_c^2}\left(\frac{\omega\varepsilon}{r}\frac{\partial E_z}{\partial \phi} - \beta\frac{\partial H_z}{\partial r}\right) \quad (2.3.32)$$

$$H_\phi = -\frac{j}{k_c^2}\left(\omega\varepsilon\frac{\partial E_z}{\partial r} + \frac{\beta}{r}\frac{\partial H_z}{\partial \phi}\right) \quad (2.3.33)$$

and $k_c^2 = \gamma^2 + k^2 = k^2 - \beta^2$

Figure 2.4 Geometry of circular waveguide

Analysing TM modes ($H_z = 0$), the Helmholtz wave equation reduces to equation 2.3.34 in cylindrical coordinates

$$\nabla_t^2 E_z = \frac{1}{r}\frac{\partial}{\partial r}\left(r\frac{\partial E_z}{\partial r}\right) + \frac{1}{r^2}\frac{\partial^2 E_z}{\partial \phi^2} = -k_c^2 E_z \quad (2.3.34)$$

and using separation of variables the solutions are found to be

$$E_z = AJ_n(k_c r)\cos n\phi \quad (2.3.35)$$

where J_n is an nth order Bessel function of the first kind. The transverse field components are now given by with $H_z = 0$ for TM waves

$$E_r = -\frac{j\beta}{k_c}AJ_n'(k_c r)\cos n\phi \quad (2.3.36)$$

$$E_\phi = \frac{j\beta n}{k_c^2 r}AJ_n(k_c r)\sin n\phi \quad (2.3.37)$$

where J' is the derivative of J. The boundary condition imposed by the guide at the wall requires that $E_z = E_\phi = 0$ at $r = a$. Looking at equation 2.3.35, E_z is zero at the boundary if $k_c a$ is one of the roots of the Bessel function

$$k_c a = \frac{2\pi a}{\lambda_c} = \omega_c\sqrt{\mu\varepsilon}\,a = p_{nl} \quad (2.3.38)$$

p_{nl} is the l^{th} root of $J_n(z)$, $J_n(p_{nl}) = 0$. Equation 2.3.38 gives the cut off frequency or wavelength for any TM mode, TM_{nl} where *n* denotes the angular variations and *l* the radial variations.

The differential equation for TE modes with $E_z = 0$ and non zero H_z in cylindrical coordinates, is

$$\nabla_t^2 H_z = \frac{1}{r}\frac{\partial}{\partial r}\left(r\frac{\partial H_z}{\partial r}\right) + \frac{1}{r^2}\frac{\partial^2 H_z}{\partial \phi^2} = -k_c^2 H_z \tag{2.3.39}$$

The solution has the form

$$H_z(r,\phi) = BJ_n(k_c r)\cos n\phi \tag{2.3.40}$$

Applying this solution to equations 2.3.30, 31, 32, 33 the resulting field components are

$$E_r = \frac{j\omega\mu n}{k_c^2 r} BJ_n(k_c r)\sin n\phi \tag{2.3.41}$$

$$E_\phi = -\frac{j\omega\mu}{k_c} BJ_n'(k_c r)\cos n\phi \tag{2.3.42}$$

The boundary condition in this case is that $E_\phi = 0$ at $r = a$ so

$$k_c a = \frac{2\pi a}{\lambda_c} = \omega_c\sqrt{\mu\varepsilon}\,a = p_{nl}' \tag{2.3.43}$$

where $J_n'(p_{nl}') = 0$. The TE_{11} mode is the dominant mode within a cylindrical waveguide.

TEM modes do not propagate within cylindrical or rectangular waveguides as TEM modes have transverse variations like static fields, and no static field can exist inside a region bounded by a single conductor [Ramo, Whinnery, Van Duzer 1994], such as the hollow pipe waveguides. TEM modes may propagate within other types of waveguide such as conducting parallel plates, these are not of interest in sub-millimetre systems. Plots of several of the modal field distributions within rectangular, square and conical waveguides can be found in [Lee 1985].

2.4 Modal Matching Technique

While the Gaussian beam mode approach discussed in section 2.2 provides an accurate description of the propagation of a quasi optical beam defined initially at a horn aperture and then propagated to the far field or through optics of a quasi-optical system no description of the electromagnetic behaviour of the antenna itself is assumed. A precise description of the internal electric and magnetic fields of a horn is essential to obtaining the reflection and transmission coefficients of the antenna itself and the front end of the system as a whole. The modal matching technique provides an accurate description of the internal fields of a horn in terms of the propagating waveguide modes. From this the transverse fields at the aperture can be determined which in turn can be used to calculate near or far-fields accurately.

The modal matching technique replaces the actual profile of a horn with a series of uniform waveguide sections slowly varying in cross sectional area in the case of smooth walled horns or for corrugated horns the sections are defined by the corrugations and following horn flare section, this is illustrated in figure 2.5. The technique accurately predicts how the internal electric and magnetic fields vary at all points within the horn with the aim to produce the transmission and reflection properties of the horn.

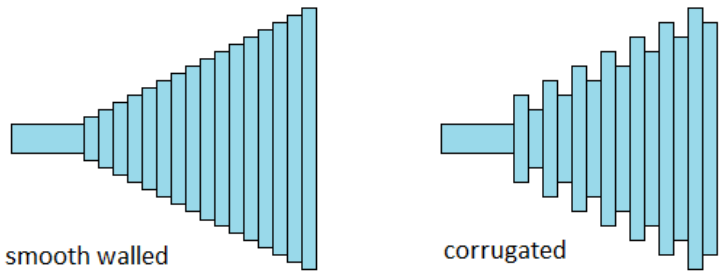

Figure 2.5 ***Uniform waveguide sections replacing the profile of a smooth walled and corrugated horn***

µWave Wizard is commercially available software developed by the company Mician and described in section 2.7.1. SCATTER is code written in Mathmatica and MATLAB developed at NUI Maynooth, introduced in section 2.7.3. Both are based on the underlying technique of mode matching and were used for the analysis of quasi optical components during this project. They both allow for the analysis of rectangular

and circular horn antenna, operating as single or a multi-moded device. A description of these packages can be found in section 2.7 (Description of modelling software).

2.4.1 Scattering parameters

Scattering parameters are an extremely useful description of the power transmitted or reflected by a system. A system can be described as a network of N ports. For example a horn transmitting and/or receiving radiation is a two port network, this is illustrated in the figure 2.6 where the horn is represented by a box.

Figure 2.6 **Diagram representing a two port network where the system is simplified and represented as a box, a1 and a2 are power in while b1 and b2 are power out of the system.**

a1 and *a2* are the input power from ports 1 and 2 respectively while *b1* and *b2* are the output power at these ports. The network is described by scattering parameters. This links the input to the output by [Huang and Boyle 2008]

$$\begin{bmatrix} b1 \\ b2 \end{bmatrix} = \begin{bmatrix} S_{11} & S_{12} \\ S_{21} & S_{22} \end{bmatrix} \begin{bmatrix} a1 \\ a2 \end{bmatrix} \tag{2.4.1}$$

So the reflection coefficients are

$$S_{11} = b1/a1$$
$$S_{22} = b2/a2 \tag{2.4.2}$$

for example S_{11} is the ratio of output power at port 1 due to a signal at port 1.

The transmission coefficients are given by

$$S_{12} = b1/a2$$
$$S_{21} = b2/a1 \tag{2.4.3}$$

S_{12} is the ratio of power output at port 1 due to power input at port 2.

This can be extended to a network of N ports.

2.4.2 Description of the modal matching technique

First consider figure 2.6 where the horn is represented as a box with power potentially propagating in both directions from left to right and vice versa. If there is a forward travelling wave incident at the throat of the horn moving left to right, this results in transmitted and reflected radiation at both the throat and aperture of the horn. The incident field can be represented by a column matrix [*A*] that describes the modal coefficients of the field in the forward direction (S_{12}), while [*B*] is a column matrix containing the modal coefficients of the reflected wave at the horn throat (S_{11}). Likewise, [*C*] and [*D*] contain the modal coefficients of the transmitted and reflected waves at the aperture (S_{21} and S_{22}). The horn is described by the scattering matrix [*S*] or an operator transforming the input coefficients to the output. Thus using the scattering matrix formulation the horn can be represented as

$$\begin{bmatrix}[B]\\[D]\end{bmatrix} = [S]\begin{bmatrix}[A]\\[C]\end{bmatrix} \tag{2.4.4}$$

For example if there is only one mode present at the input, [*A*] will be given by

$$[A] = \begin{bmatrix}1\\0\\0\\\vdots\end{bmatrix} \tag{2.4.5}$$

The length of the column matrix will depend on how many modes are used to represent the propagating field at the input. The elements of [*S*] form square matrices as the same number of modes are used from start to finish in the analysis. These square matrices describe the coupling between all modes at the input with all modes at the output of the horn. And in general we can write

$$[S] = \begin{bmatrix}[S_{11}] & [S_{12}]\\[S_{21}] & [S_{22}]\end{bmatrix} \tag{2.4.6}$$

This approach is applied to the uniform waveguide sections that replace the profile of the horn where [*A*] and [*B*] are now the forward and reflected modal

coefficients looking into a junction at the input and [*C*] and [*D*] are the forward and reflected modal coefficients looking into the junction at the output. The coefficients of modes present at the input to the junction are used to determine the coefficients of modes present at the output to the junction where energy conservation and scattering of power between modes is accounted for. These mode coefficients at the output will subsequently become the inputs to the next junction. [*S*] describes the scattering between mode coefficients in [*A*], [*B*], [*C*] and [*D*] at the junction. Each junction will have its own scattering matrix. In the short waveguide section following each junction the phase evolution of each mode affects the modal coefficients. This is expressed in a separate scattering matrix. These matrices are cascaded together to produce an overall scattering matrix describing the horn.

Cascading scattering matrices is relatively straightforward. If two matrices have elements

$$[S^a] = \begin{bmatrix} [S^a{}_{11}] & [S^a{}_{12}] \\ [S^a{}_{21}] & [S^a{}_{22}] \end{bmatrix} \quad \text{and} \quad [S^b] = \begin{bmatrix} [S^b{}_{11}] & [S^b{}_{12}] \\ [S^b{}_{21}] & [S^b{}_{22}] \end{bmatrix} \tag{2.4.7}$$

the cascaded matrix is [Olver 1994]

$$[S^c] = \begin{bmatrix} [S^c{}_{11}] & [S^c{}_{12}] \\ [S^c{}_{21}] & [S^c{}_{22}] \end{bmatrix} \tag{2.4.8}$$

where

$$[S^c{}_{11}] = [S^a{}_{21}][[\mathrm{I}] - [S^b{}_{11}]\,[S^a{}_{22}]\,]^{-1}\,[S^b{}_{11}]\,[S^a{}_{21}] + [S^a{}_{11}]$$

$$[S^c{}_{12}] = [S^a{}_{12}]\,[[\mathrm{I}] - [S^b{}_{11}]\,[S^a{}_{22}]\,]^{-1}\,[S^b{}_{12}]$$

$$[S^c{}_{21}] = [S^b{}_{21}]\,[[\mathrm{I}] - [S^a{}_{22}]\,[S^b{}_{11}]\,]^{-1}[S^a{}_{21}]$$

$$[S^c{}_{22}] = [S^b{}_{21}]\,[[\mathrm{I}] - [S^a{}_{22}]\,[S^b{}_{11}]\,]^{-1}[S^a{}_{22}]\,[S^b{}_{12}] + [S^b{}_{22}]$$

where $[\mathrm{I}]$ is the identity matrix.

At the aperture of the horn it is assumed that there is no reflection so [*C*] will be zero (this is not true for each waveguide section). From

$$\begin{bmatrix} [B] \\ [D] \end{bmatrix} = \begin{bmatrix} [S_{11}] & [S_{12}] \\ [S_{21}] & [S_{22}] \end{bmatrix} \begin{bmatrix} [A] \\ [C] \end{bmatrix} \tag{2.4.9}$$

it can be seen that the reflected coefficients at the input and the transmitted coefficients at the output are given by

$$[B] = [S_{11}][A] + [S_{12}][C] \quad and \quad [D] = [S_{21}][A] + [S_{22}][C] \qquad (2.4.10)$$

2.4.3 Mode propagation in a uniform waveguide section.

The scattering matrix [*S*] describing a short uniform waveguide section includes the modal phase change as the modes propagate through the guide. The elements of [*S*] are given by

$$[S_{11}] = [S_{22}] = [0]$$

$$[S_{12}] = [S_{21}] = [V] \qquad (2.4.11)$$

Where [*V*] is a diagonal matrix whose size is equal to the number of modes used in the analysis. *V* is given by [Olver 1994]

$$V_{nm} = e^{-j\beta_n L} \qquad (2.4.12)$$

β_n is the propagation constant for a particular mode and *L* is the length of waveguide section. For example the scattering matrix describing a section of waveguide is given by

$$[S] = \begin{bmatrix} [0] & [V] \\ [V] & [0] \end{bmatrix} \qquad (2.4.13)$$

To ensure accuracy in the analysis to represent a horn made up of a large number of sections, the length of the sections of waveguide used to represent a horn should be short enough to accurately describe the internal fields evanescent modes excited by scattering to higher order modes i.e. each representative section should be of the order of one tenth of a wavelength. A sufficient number of modes must also be included in the analysis to accurately describe the field. In chapter 3, the mode matching technique is applied to the analysis of conical horns, the number of waveguide sections used in the analysis is varied and the effects can be seen in the far-field results.

2.4.4 Mode Scattering at a discontinuity

For a step discontinuity as in figure 2.7 where a smaller waveguide meets a larger waveguide at a junction *z = 0* with the cross sectional area of the smaller waveguide being s_L and the larger being s_R it is required that the transverse components of the electric and magnetic fields are continuous across the opening of a junction.

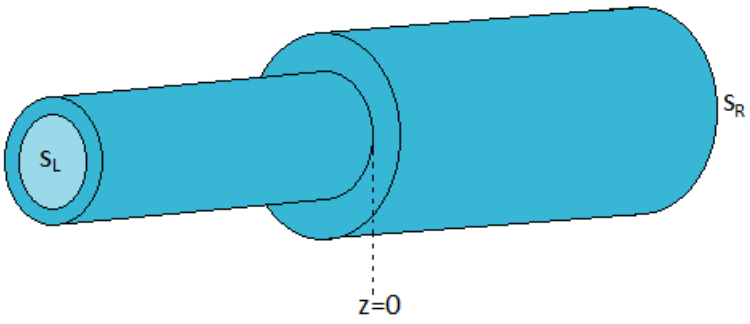

Figure 2.7 ***Junction between to cylindrical sections***

At the metal surface of the junction the transverse electric field and the normal component of the magnetic field must vanish to satisfy Maxwell's equations. To simplify the matching of fields at the discontinuity the same number of modes *N* are considered on both sides of the junction. The electric and magnetic fields in the plane of the discontinuity are given by [Olver 1994]

$$\boldsymbol{E}_L = \sum_{n=1}^{N}\{A_n\, e^{-j\beta_n z} + B_n e^{j\beta_n z}\}\boldsymbol{e}_{nL} \qquad (2.4.14a)$$

$$\boldsymbol{H}_L = \sum_{n=1}^{N}\{A_n\, e^{-j\beta_n z} - B_n e^{j\beta_n z}\}\boldsymbol{h}_{nL} \qquad (2.4.14b)$$

$$\boldsymbol{E}_R = \sum_{n=1}^{N}\{D_n\, e^{-j\beta_n z} + C_n e^{j\beta_n z}\}\boldsymbol{e}_{nR} \qquad (2.4.14c)$$

$$\boldsymbol{H}_R = \sum_{n=1}^{N}\{D_n\, e^{-j\beta_n z} - C_n e^{j\beta_n z}\}\boldsymbol{h}_{nR} \qquad (2.4.14d)$$

where the subscripts *L* and *R* refer to the left and right sides of the discontinuity. A_n and B_n are the forward and reflected amplitude coefficients of the n^{th} mode on the left hand side of the junction. Similarly C_n and D_n are the equivalent coefficients to the right of the junction. $\pm\beta_n$ is the propagation constant whose sign is determined by the direction of propagation. $\boldsymbol{e}_n e^{\pm j\beta z}$ and $\boldsymbol{h}_n e^{\pm j\beta z}$ are the transverse fields for the n^{th} mode. As the total transverse fields must match across the junction at *z = 0*

$$\sum_{n=1}^{N}(A_n + B_n)\boldsymbol{e}_{nL} = \sum_{n=1}^{N}(D_n + C_n)\boldsymbol{e}_{nR} \qquad (2.4.15)$$

$$\sum_{n=1}^{N}(A_n - B_n)\boldsymbol{h}_{nL} = \sum_{n=1}^{N}(D_n - C_n)\boldsymbol{h}_{nR} \tag{2.4.16}$$

As stated earlier the boundary conditions also state that the transverse electric field across the area (s_R - s_L) will be zero. This leads to a pair of simultaneous equations which can be expressed in matrix form as

$$[P]\big[[A] + [B]\big] = [Q]\big[[C] + [D]\big] \tag{2.4.17a}$$

$$[P]^T\big[[D] - [C]\big] = [R]\big[[A] - [B]\big] \tag{2.4.17b}$$

where [*A*] and [*B*] are column matrices containing the unknown modal coefficients of the left hand side of the junction A_1 to A_N and B_1 to B_N. Similarly, [*C*] and [*D*] are column matrices containing the unknown modal coefficients for the right hand side of the junction. [*P*], [*Q*] and [*R*] describe the power coupling between modes. [*P*] is an *N*×*N* square matrix the elements of which are integrals that describe the mutual power coupled between mode *i* on the left hand side and mode *j* on the right hand side.

$$P_{ij} = \int_{sL}\big(\boldsymbol{e}_{iL} \times \boldsymbol{h}_{jR}\big).\,\mathrm{d}s_L \tag{2.4.18}$$

And $[P]^T$ is the transpose of [*P*]. [*Q*] is a diagonal *N*×*N* matrix describing the self coupled power between modes on the right hand side of the junction. The elements have the form

$$Q_{jj} = \int_{sR}\big(\boldsymbol{e}_{jR} \times \boldsymbol{h}_{jR}\big).\,\mathrm{d}s_R \tag{2.4.19}$$

Likewise, [*R*] is also a diagonal *N*×*N* matrix this time describing the self coupled power between modes on the left hand side of the junction with elements

$$R_{ii} = \int_{sL}(\mathbf{e}_{iL} \times \mathbf{h}_{iL}).\,\mathrm{d}s_L \tag{2.4.20}$$

The simultaneous matrix equations expressed above can be rearranged into the scattering matrix form. The elements of [*S*] are thus

$$[S_{11}] = \big[[R] + [P]^T[Q]^{-1}[P]\big]^{-1}\big[[R] - [P]^T[Q]^{-1}[P]\big] \tag{2.4.21a}$$

$$[S_{12}] = 2[[R] + [P]^T[Q]^{-1}[P]]^{-1}[P]^T \tag{2.4.21b}$$

$$[S_{21}] = 2[[Q] + [P][R]^{-1}[P]^T]^{-1}[P] \tag{2.4.21c}$$

$$[S_{22}] = -\big[[Q] + [P][R]^{-1}[P]^T\big]^{-1}\big[[Q] - [P][R]^{-1}[P]^T\big] \tag{2.4.21d}$$

the inverse matrix $[Q]^{-1} = [I]/[Q]$.

The analysis described above is for discontinuities whose right hand side is larger than the left hand side. If this is not true for cases such as corrugated horns then the elements of [*S*] simply become

$$[S] = \begin{bmatrix} [S_{22}] & [S_{21}] \\ [S_{12}] & [S_{11}] \end{bmatrix} \tag{2.4.22}$$

This theory is implemented in code called SCATTER developed at NUI Maynooth and an example analysis and implementation of the code is described in section 2.7.3 to illustrate its operation with a straight forward example.

2.5 Radiation patterns of horn antennas

Having discussed in the previous sections how the aperture field of a horn antenna can either be represented by a scalar field (GBMA) or determined by analysing the full electromagnetic behaviour of the horn (mode matching) one might now be interested in determining the far field radiation pattern of the horn. If the aperture field is known this can be done by use of Fourier transforms and using a number of approximations. Firstly the field equivalence principle is invoked, this means that the antenna can be replaced by equivalent electric and magnetic surface currents that will produce equivalent radiation fields to those produced by the antenna. The equivalent currents are on an imaginary surface in the aperture plane, outside of the aperture the fields are assumed to be zero on the surface. The tangential components of the field are known in the aperture and assumed to exist as a result of equivalent current sources in the aperture. The corresponding electric and magnetic source current densities ***J*** and ***M*** are given by [Olver 1994]

$$\boldsymbol{J}_{ap} = \hat{\boldsymbol{n}} \times \boldsymbol{H}_{ap} \tag{2.5.1}$$

$$\boldsymbol{M}_{ap} = -\hat{\boldsymbol{n}} \times \boldsymbol{E}_{ap} \tag{2.5.2}$$

where, $\boldsymbol{E}_{ap}$ and $\boldsymbol{H}_{ap}$ are the electric and magnetic tangential field components in the aperture and $\hat{\boldsymbol{n}}$ is the normal to the aperture plane. Auxiliary potential functions $\boldsymbol{A}_{ap}$ and $\boldsymbol{F}_{ap}$ generated by the source current densities $\boldsymbol{J}_{ap}$ and $\boldsymbol{M}_{ap}$ are found first which

in turn are used to determine the electric and magnetic field intensities $\boldsymbol{E}$ and $\boldsymbol{H}$. The auxiliary vector potential functions are related to the source current densities by integral relations, for a homogenous isotropic system they are given by

$$\boldsymbol{A}_{ap} = \frac{\mu}{4\pi}\int_S \frac{\boldsymbol{J}_{ap}e^{-jkR}}{R}dS \tag{2.5.3}$$

$$\boldsymbol{F}_{ap} = \frac{\varepsilon}{4\pi}\int_S \frac{\boldsymbol{M}_{ap}e^{-jkR}}{R}dS \tag{2.5.4}$$

where *S* is the surface at the aperture and *dS* represents integration over the aperture. If the aperture fields are known then the far field pattern can be derived from these potentials. The total fields are determined by the superposition of the individual fields due to $\boldsymbol{A}$ and $\boldsymbol{F}$ where $\boldsymbol{E}_a$ and $\boldsymbol{H}_a$ are due to $\boldsymbol{A}$ while $\boldsymbol{E}_f$ and $\boldsymbol{H}_f$ are due to $\boldsymbol{F}$. In the far-field these fields can be expressed as [Balanis 2005]

$$\boldsymbol{E}_A \approx -j\omega\boldsymbol{A} \tag{2.5.5}$$

$$\boldsymbol{H}_A \approx -j\frac{\omega}{\eta}\hat{a}_r \times \boldsymbol{A} \tag{2.5.6}$$

$$\boldsymbol{H}_F \approx -j\omega\boldsymbol{F} \tag{2.5.7}$$

$$\boldsymbol{E}_F \approx j\omega\eta\hat{a}_r \times \boldsymbol{F} \tag{2.5.8}$$

where $\eta = \sqrt{\mu/\varepsilon}$ is the intrinsic impedance of the medium. $\boldsymbol{E} = \boldsymbol{E}_A + \boldsymbol{E}_F$ and $\boldsymbol{H} = \boldsymbol{H}_A + \boldsymbol{H}_F$. The corresponding far-field E and H field components are orthogonal to each other and form a TEM mode. The field distribution in the far field is the Fourier Transform of the field distribution at the aperture and vice versa. Figure 2.8 indicates the coordinate geometries.

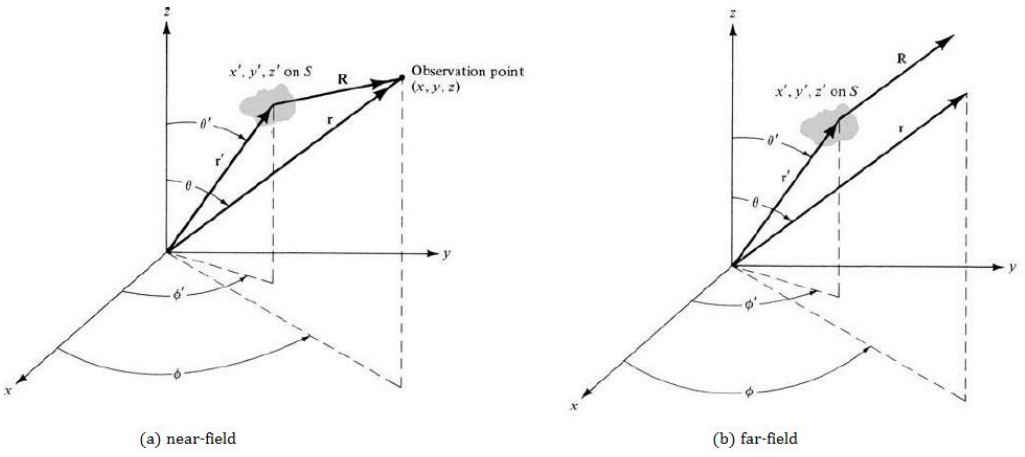

Figure 2.8 ***Near and far-field coordinate systems [Balanis 2005]***

R can be approximated by $R \approx r - r' \cos\psi$ for phase variations and $R \approx r$ for amplitude variations where ψ is the angle between the vectors $\boldsymbol{r}$ and $\boldsymbol{r}'$. The primed coordinates represent the space occupied by the sources $\boldsymbol{J}_{ap}$ and $\boldsymbol{M}_{ap}$, over which the integration is performed. The un-primed coordinates represent the observation point. The fields radiated by antennas of finite size are spherical waves thus spherical coordinates are introduced for the observation plane in the far field.

$$R = r - r' \sin\theta \cos(\phi - \phi') \tag{2.5.9}$$

The two dimensional Fourier Transform of the aperture field $\boldsymbol{E}_{ap}$ is

$$\boldsymbol{f}(\theta, \phi) = \iint_{S'} \boldsymbol{E}_{ap}(x', y') e^{jkR} dS \tag{2.5.10}$$

The Fourier Transform of the aperture field can be split into its Cartesian components,

$$f_x(\theta, \phi) = \int_{x'} \int_{y'} \boldsymbol{E}_{ax}(x', y') \exp\left[jk\{r' \sin\theta \cos(\phi - \phi')\}\right] r' dr' d\phi' \tag{2.5.11}$$

$$f_y(\theta, \phi) = \int_{x'} \int_{y'} \boldsymbol{E}_{ay}(x', y') \exp\left[jk\{r' \sin\theta \cos(\phi - \phi')\}\right] r' dr' d\phi' \tag{2.5.12}$$

From this it can be seen that if the field across the aperture of a antenna is known the far-field can be calculated by use of Fourier Transforms.

Another method of determining radiation patterns of antennas in both the near and far-field is by the use of spherical wave analysis. Spherical wave analysis can also be used to determine the internal electromagnetic behaviour of the horn similar to the cylindrical wave analysis mode matching technique described in section 2.4 although as it is more complicated its major advantage is in the determination of radiation patterns. It has the advantage over aperture theory described above that no approximations are involved in computing the near field radiation pattern. In spherical wave analysis the fields at the aperture of the horn are represented as a sum of spherical waves which are then projected into the radiation sphere and the fields can be computed at any distance in front of the horn. The fields in the radial direction are given by equations of the form [Olver 1994]

$$E_R = A \frac{v(v+1)}{jkR^2} h_v^{(2)}(kR) P_v^m(\cos\theta) \cos m\phi \tag{2.5.13}$$

$$H_R = B \frac{v(v+1)}{jkR^2} h_v^{(2)}(kR) P_v^m(\cos\theta) \sin m\phi \tag{2.5.14}$$

where $P_v^m(\cos\theta)$ is an associated Legendre function of order *m* and degree *v*, and $h_v^{(2)}(kR)$ is a spherical Hankel function of order *v*. The eigenfunction *v* is determined from the boundary conditions. Spherical wave expansion along with boundary contour mode matching (BCMM) is the method used by the modelling software Microwave Wizard (section 2.7.1) for the calculation of near and far-field patterns.

2.6 Finite Integration Technique

The Finite Integration Technique (FIT) is the third and final analytical technique used during this project for the analysis of quasi-optical system components. It is the method used by the software CST (section 2.7.4) for the determination of scattering parameters and radiation patterns. The finite integration technique is a generalisation of the finite-difference time domain method, FDTD is a grid based differential time domain numerical modelling method in which the problem domain is discretized by a grid and the time-dependant partial differential Maxwell equations are solved within each cell to give an overall description of the problem domain. FIT discretizes the integral form of Maxwell's equations (instead of the differential) on a pair of interlaced discretization grids. The integral form of Maxell's equations are given by

$$\oint_{\partial A} \mathbf{E}.\, d\boldsymbol{s} = -\int_A \frac{\partial \mathbf{B}}{\partial t}.\, d\mathbf{A} \tag{2.6.1}$$

$$\oint_{\partial A} \mathbf{H}.\, d\boldsymbol{s} = \int_A \left(\frac{\partial \mathbf{D}}{\partial t} + \mathbf{J}\right).\, d\mathbf{A} \tag{2.6.2}$$

$$\oint_{\partial V} \mathbf{D}.\, d\mathbf{A} = \int_V \rho\, dV \tag{2.6.3}$$

$$\oint_{\partial V} \mathbf{B}.\, d\mathbf{A} = 0 \tag{2.6.4}$$

The structure being analysed is discretized into mesh cells (cuboids) and a second mesh is set up orthogonally to the first one, this is illustrated in figure 2.9 below where *e* are the electric grid voltages and *h* are the magnetic grid voltages.

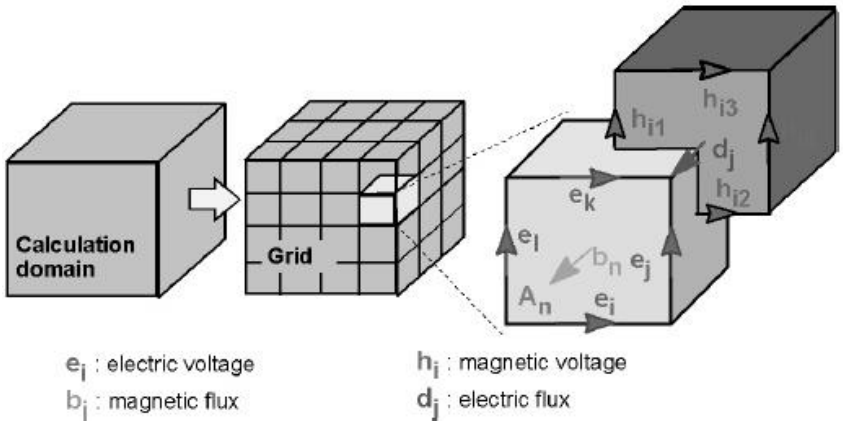

Figure 2.9 ***Illustration of discretization grid used within the Finite Integration Technique [CST MWS Advanced topics]***

Maxwell's equations are formulated for each of the cells separately. Properties of the material (i.e. μ, ε, σ) are easily incorporated in to the method, as they appear in Maxwell's equations. After discretization the material property relations become

$$d = M_\epsilon e, \qquad b = M_\mu h, \qquad j = M_\sigma e + j_s \tag{2.6.5}$$

where M_ϵ, M_μ, M_σ are matrices describing the material properties. These material matrices however contain unavoidable approximations. Values of *e* and *h* are sampled in a leap frog manner at times separated by half a time step - *e* field updates are conducted midway during each time step between successive *h* field updates and conversely, this eliminates the need to solve simultaneous equations. The recursion is stable if the time step inside an equidistant grid meets the Courant criterion

$$\Delta t \leq \frac{1}{c\sqrt{\frac{1}{\Delta x^2}+\frac{1}{\Delta y^2}+\frac{1}{\Delta z^2}}} \tag{2.6.6}$$

In this way an overall description of the problem domain enclosed by the grid is obtained. The accuracy of the results depend on the cell size and time step. FIT can be applied to many electromagnetic problems and all frequency ranges, from static field to high frequency calculations in the time or frequency domain.

2.7 Description of the modelling software

Several developed software techniques and commercial packages have been used throughout this project for the analysis of horn antenna and quasi-optical system components. Using techniques based on different methods of analysis provides verification of the results obtained and allows estimates of the accuracy obtainable with each technique (e.g. GBM theory is only a scalar approximation and cannot be used to the same degree of accuracy as a full electromagnetic description utilised in the CST environment). In addition the technique or software package applied to different components might be more or less suited and this also needs to be accounted for in assessing the results obtained. A description of the software theory and implementation is provided here. Examples are also included to illustrate how the user implements the software/technique and obtains the results.

2.7.1 µWave Wizard (µWW)

µWave Wizard is a software package developed by the company Mician for the use of Microwave Engineers with the aim of providing fast and accurate design tools [www.mician.com]. The program allows the user to model complex waveguide structures selected from a comprehensive library of elements. Both mode matching and 3D finite element methods (similar to the FIT although discretizing Maxwell's equations in differential form) are used to calculate the response of waveguide structures in the millimetre and sub-millimetre range. Near and far-field radiation patterns are calculated using spherical wave expansion from section 2.5. Transmission and reflection coefficients of systems are also calculated, these multimodal scattering parameters are shown in the frequency response plot graph which shows the reflected or transmitted radiation for each propagating mode. There are also a number of tools included in the package such as optimization and filter analysis tools etc to aid in the design process.

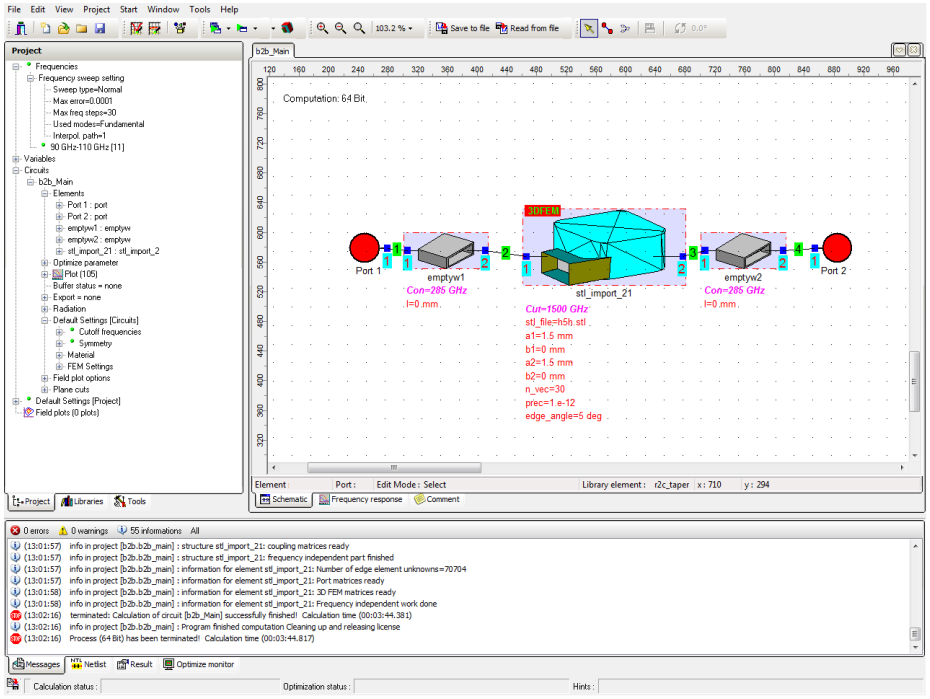

Figure 2.10 ***Screenshot of the Microwave wizard graphical user interface***

Figure 2.10 shows the Microwave wizard graphical user interface. On the left hand side of the GUI the project tree view contains all information about the current project, under another tab this is also where the library of elements (used to construct system models) is found. Elements are selected from the library and placed on the schematic editor to the right. At the bottom of the screen an info panel and status bar display messages related to the project as it is running and the current status of the analysis. µWW has an extensive library (figure 2.11a) from which the building blocks of the system are chosen such as horn antenna, irises, waveguides, resonators etc. The parameters of these building blocks such as length, radius, cut-off frequency etc. must be entered by the user using the element editor (figure 2.11b). Each element must be separated on the schematic editor by an empty waveguide (these are indicated on figure 2.10) which can be selected from the library. These empty waveguides can be given a length of zero so as to have no effect of the system. Their use is in ensuring that the number of modes throughout the system is constant. The fields within an empty waveguide can also be plotted using the field plot option thus the internal EM field at any point along the structure where an empty waveguide is placed, such as at the horn aperture, can be visualized in the analysis.

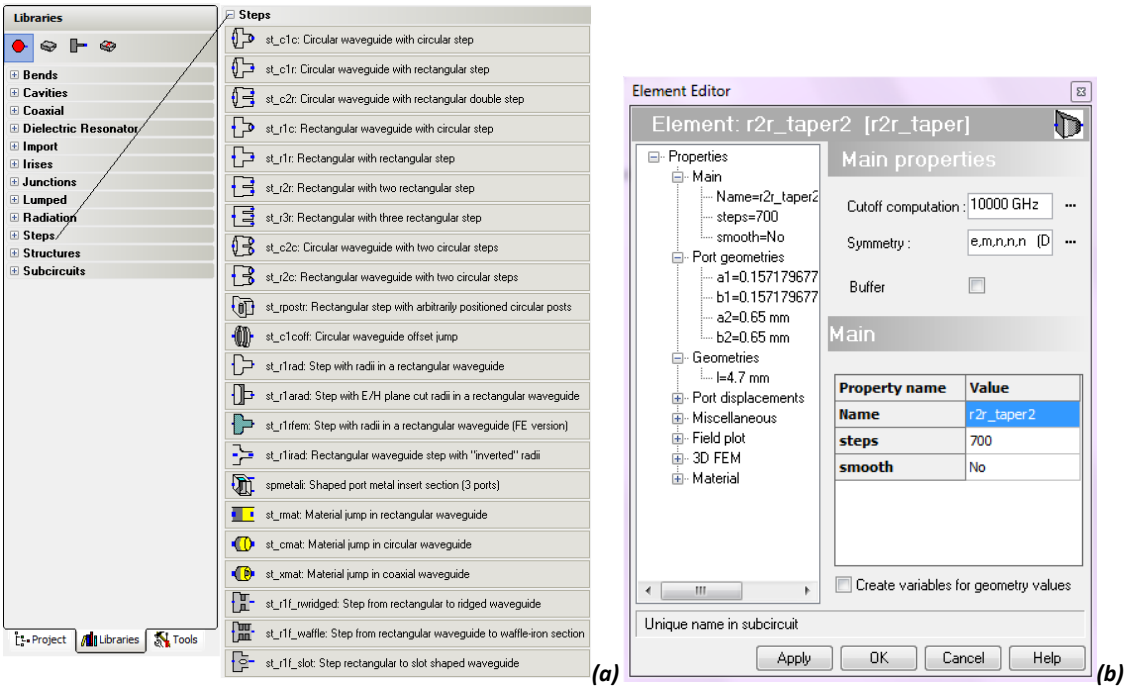

Figure 2.11 (a) A sample of the µWW library. (b) The element editor within µWW

An important input parameter in Microwave Wizard is the cut-off frequency of all elements in the project. This specifies how many modes will propagate within the element. There are two input fields the computation cut-off frequency, which specifies how many modes will propagate, and the percentage of cut-off frequency used, which can be varied for each element, used to ensure the same number of modes are propagating throughout the system as the system components dimensions vary. As an example consider a conical horn, more modes will propagate at the aperture of the horn than at the throat of the horn as the radius is larger. The percentage of cut-off frequency used should be lowered in the empty waveguide at the aperture of the horn and increased at the throat waveguide end to ensure modes into the horn match modes out of the horn. This can be checked by right clicking an empty waveguide and selecting 'View list of modes', this will show propagating and attenuated modes up to the percentage of cut-off frequency selected, the Waveguide tool within µWW works in the same way. Symmetry can also be set for all elements of the system in both Cartesian and circular coordinates. Depending on the symmetry of the mode polarisation, symmetry can be set in the x-y, y-z and x-z plane this effectively reduces the computation domain by 1/2, 1/4 or 1/8. This is desirable as it can lead to a

significant decrease in computation time and particularly useful for a single moded horn which µWW in primarily designed to analyse.

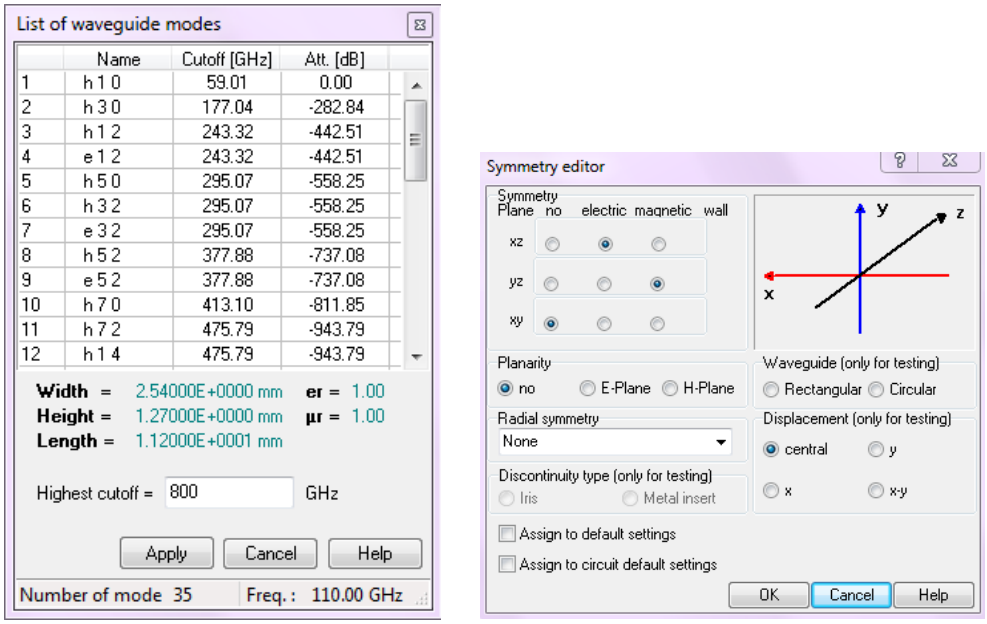

Figure 2.12 ***Left, list of modes showing the mode, cut-off frequency and attenuation of each. Right, the symmetry editor of µWW***

2.7.2 Example- Building a simple structure in µWW

Consider building a simple smooth walled conical horn radiating into free space. With this example both the scattering parameters and the far/near field pattern of the horn can be obtained. The horn is designed to operate at 100 GHz and will be analysed over the 90 - 110 GHz waveband. System components are selected from the library tab on the left hand side of the GUI. Elements are sorted into sections such as bends, cavities, junctions, steps, etc. The conical horn antenna should be selected from the radiation group and placed on the workspace. The radiation element should also be selected and placed, this element simulates radiation from a circular aperture into free space. With the current version 7.8, there is no radiation from a square aperture available so for examples such as a radiating pyramidal horn a step from square to circular waveguide must be connected between elements. A port is also required to provide an excitation signal, in this example of a horn radiating into free space only one port is necessary although multiple ports can be placed if needed. The empty waveguides separating each element must also be placed. These empty waveguides are useful in keeping the number of connection modes between each element

constant. Each element must be connected using the connect modulus at the top of the screen. Once all desired elements are placed on the schematic editor their parameters must be set. By double clicking on an element a properties box is shown where important input parameters must be set such as cut-off frequency, symmetry and geometry. The cut-off frequency of a 100 GHz horn should be ~ 1000 GHz, Mician suggest a cut-off frequency of 10 times the operating frequency although as will be discussed later on in chapter 3 this rule can be relaxed a little at higher operating frequencies.

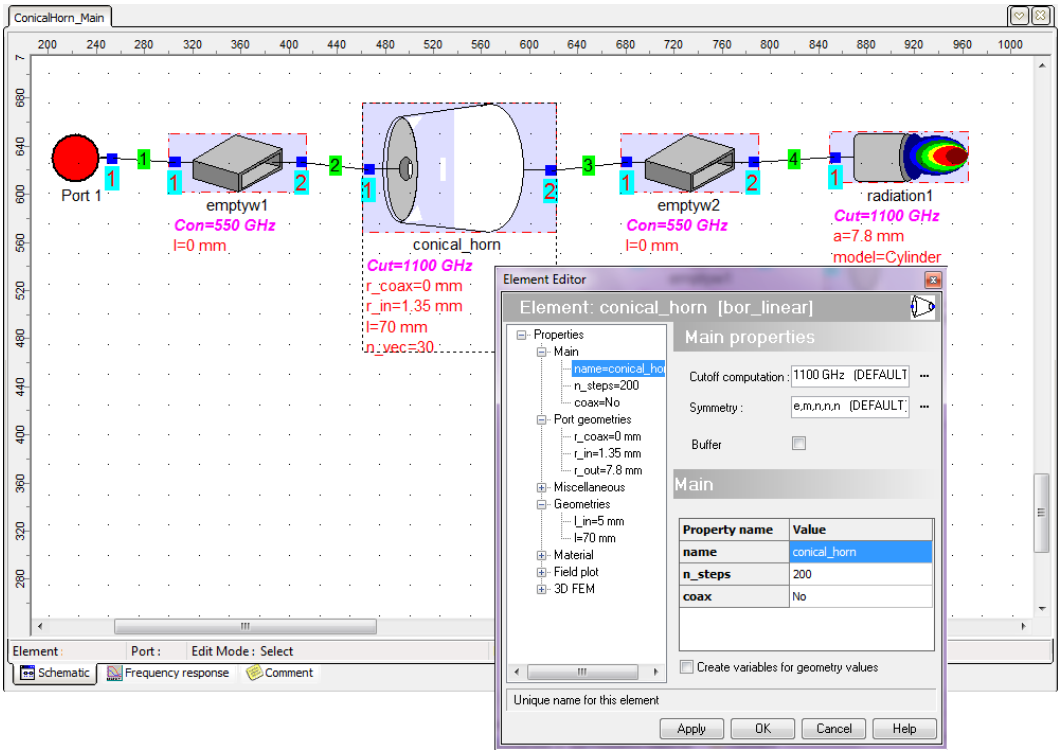

Figure 2.13 ***µWave Wizard Schematic editor of the GUI showing a smooth walled conical horn radiating in to free space and the element editor of the conical horn were all relevant parameters are set.***

The radiation element has several input parameters. The radiation model depends the shape of the radiating element e.g. sphere is used for radiation from a truncated sphere, conical radiation from a conical element etc. Flange width around the aperture is also set by the user as well as distance from aperture to coordinate origin. A small change to just one of these input parameters can produce a significant change in the far field results. Far field radius, phase centre, co- and cross polarization for the radiation element are entered using the project tree view. Once all relevant parameters are set the project can be ran by simply selecting Start -> Run Project.

Once the analysis is finished the scattering parameters will be displayed on the screen and the radiation pattern can be selected from the project tree view.

The cut off frequency can have a significant effect on the results. A cut off frequency of at least ten times the mid operating frequency is recommended, this should be increased and the project ran again until it is seen that the results are convergent. An implementation of this is given in section 3.3 in the analysis of a conical horn where the effects of varying the cut-off frequency can be seen on the scattering parameters obtained for the system.

2.7.3 SCATTER

SCATTER is software developed at NUI Maynooth for the analysis of quasi-optical system components. It is code written in Mathmatica a fully integrated technical software package based on the C programming language. SCATTER utilises the mode-matching technique described in section 2.4. It was originally developed by Dr. Ruth Colgan and Dr. Emily Gleeson, an extensive description of the software can be found in [Colgan 2001] and [Gleeson 2004]. It has developed further since then and currently smooth walled circular, corrugated circular and pyramidal antenna both single and multi-moded can be modelled.

The first step in SCATTER is a geometry file describing the horn must be read in. As described earlier, during modal analysis the horn is divided into sections of waveguide with lengths much less than the wavelength of operation. A file describing the geometry of the horn that is the number of sections, each sections length and radius, along with the operating frequency and mode azimuthal order is generated. Table 2.1 illustrates a typical format, for a simple smooth walled conical horn.

Operating Frequency	100
Azimuthal order	1
Number of sections	5
Length of 1st section	0.3
Length of 2nd section	0.3
Length of 3rd section	0.3
Length of 4th section	0.3
Length of 5th section	0.3
Radius of 1st section	1.535
Radius of 2ndsection	2.535
Radius of 3rd section	3.535
Radius of 4th section	6.535
Radius of 5th section	7.535

Table 2.1 ***Example of the format of a typical geometry file to be read in to SCATTER***

In the case of smooth walled horns each section will be increasing in radius whereas corrugated geometry files alternate between corrugation and horn flare radius. This file can be generated easily using Mathmatica or prepared in EXCEL. Examples of smooth and corrugated horn profiles generated are plotted below in figure 2.14. These horns are designed to operate at 100 GHz, the corrugated horn has a typical aperture radius of 8 mm and length 65 mm fed by a waveguide of length 5 mm.

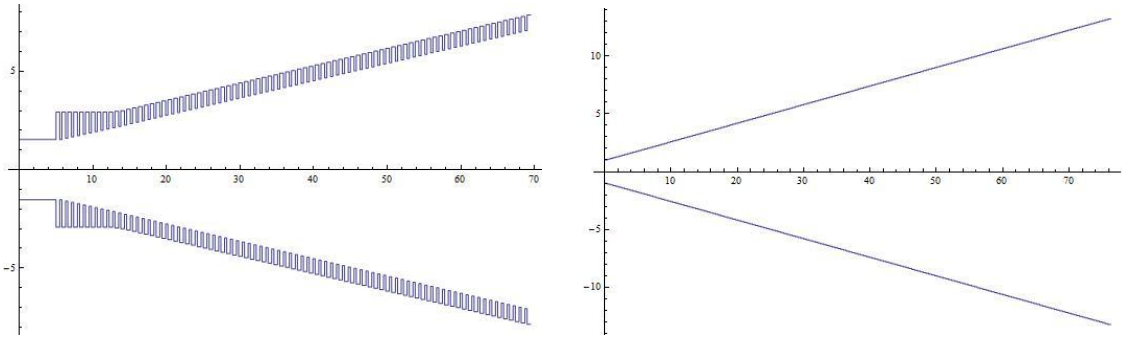

Figure 2.14 ***Plots of geometry files generated in Mathmatica of corrugated (left) and smooth walled (right) horn antenna***

Once the geometry file is read to SCATTER the modal coefficients of the horn structure are calculated using the scattering matrix formulation described in section 2.4 above. From this scattering matrix formulism including all four S parameter matrices and both near and far field patterns with amplitude and phase can be plotted. Data can also be output to MS EXCEL if needed. The reflection and transmission properties of the system can be obtained over a frequency range by running the code at several different frequencies over the operating band.

Since its development at NUIM SCATTER has continuously been tested and verified against industry standard millimetre wave modelling packages. Examples of it used in the analysis of specific horns is given in chapters 3 and 4.

2.7.4 Computer Simulation Technology Studio Suite (CST)

CST studio suite is electromagnetic simulation software that uses finite integration techniques (FIT) to perform simulations [www.cst.com]. CST is comprised of several modules, the Microwave studio used for this project provides 3D simulation of high frequency devices. FIT discretises Maxwell's equations in integral form. Structures are divided up by mesh cells this splits up the calculation domain into several grid cells. The coarseness of this mesh is set by the user and can be viewed on the GUI. CST internally sets up a second grid orthogonal to the first. Maxwell's equations are solved for each cell separately in both the original and orthogonal grid. Solutions are 'stitched' together to give an overall description of the system. In this way both S parameters and far-field radiation pattern results can be obtained.

CST Microwave Studio (MWS) uses Computer Aided Design to model structures. Microwave components such as horn antenna, cavities, etc can be modelled from 3 dimensional volumes. Bricks, cylinders, spheres, cones and tori are defined on the GUI and additional structures are added or subtracted, components can be manipulated using a variety of operations such as hollow, extrude etc. to create numerous complex structures that can visualised with the 3D viewer. Figure 2.15 shows a typical 100 GHz pyramidal horn modelled in CST MWS, the horn has

dimensions aperture height 20 mm, aperture width 27 mm, length 63.5 mm and is fed by a standard WR-10 waveguide (1.27 x 2.54 mm)

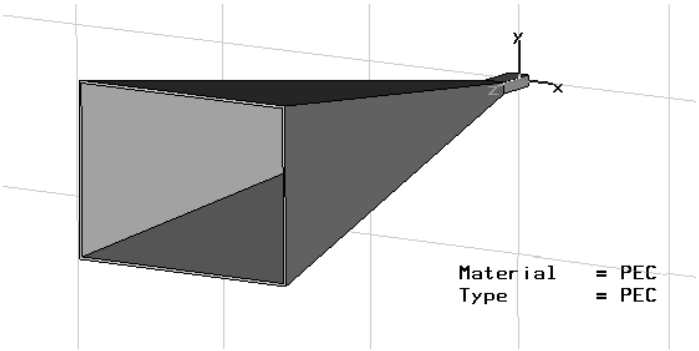

Figure 2.15 Pyramidal horn modelled in CST MWS which utilises computer aided design

A simple horn such as this can be modelled by defining two rectangular bricks - the waveguide and the aperture - separated by the length of the horn, the two bricks are then joined together using the loft option - this gives the shape of the horn. The horn is then simply shelled where the thickness of the horn walls is specified and the structure is hollowed out leaving the horn structure. The next step is to define the coarseness of the mesh to be used in the computation, this describes how small each grid cell within which Maxwell's equations are solved are. A courser mesh corresponds to higher accuracy.

While CST MWS solver techniques produce proven accurate results the computational power and time can be quite extensive when applied to quasi-optical systems of interest here as the structures are many wavelengths in dimension and so the large meshes required become a computational issue. In theory this technique can be applied but in practise it become difficult for large waveguide structures or horn antenna. For this reason CST was used only for the analysis of small structures during this project.

2.8 Conclusion

This chapter begins with a thorough explanation of the theory utilised throughout the thesis in the analysis of horn antenna. Gaussian beam mode analysis was introduced as a technique to propagate quasi-optical beams through free space and the optics of terahertz systems. Gaussian beam mode solutions in Cartesian and cylindrical coordinates are presented in the form of Hermite and Laguerre Gaussian mode sets. Following on from this the electromagnetic field distribution of waveguide modes were discussed and field components were derived for both rectangular and cylindrical waveguides. A second analysis method, the mode matching technique, was presented as a method of accurately describing the internal electromagnetic behaviour of quasi-optical components through the use of cascaded scattering matrices describing the forward and backward propagation of modes at discontinuities and uniform waveguide sections providing the overall reflection and transmission properties of a quasi-optical component. The mode matching technique is used throughout the thesis, in chapters 3 and 4 conical and pyramidal horns are analysed using mode matching methods and the results are compared against the aforementioned GBMA results. GBMA and mode matching methods are combined together in chapter 6 for the analysis of multiple reflections between two horn antenna. The final analysis method, the finite integration technique, discretizes a structure into meshcells and utilises Maxwell's equations in integral form to solve for the electromagnetic behaviour of the structure, this method is used throughout chapter 5 in the analysis of simple waveguide structures. The chapter concludes with a description of modelling and analysis software used throughout the thesis along with examples of how to build simple structures within these packages - Microwave Wizard and SCATTER both utilising the mode matching technique and Computer Simulation Technology (CST) Microwave studio employing the finite integration technique.

CHAPTER 3

Analysis of Conical Horns

3.1 Introduction - Smooth walled and corrugated conical horns

This chapter examines methods for modelling and analysis of conical horns using techniques described in chapter 2 namely Gaussian beam mode analysis and mode matching. Conical horns are essentially flared sections of circular waveguides that couple radiation from free space to the waveguide detectors for example, in an astronomical receiver system. A transition region may be included to couple the conical horn to a rectangular waveguide in the throat of the horn, standard WR-10 waveguide flange components are widely used in W-band measurements. The walls of conical horns can be either smooth or corrugated as shown in figure 3.1. Both types are used in sub-millimetre quasi-optical systems each with their own particular advantage that will be discussed in the following sections.

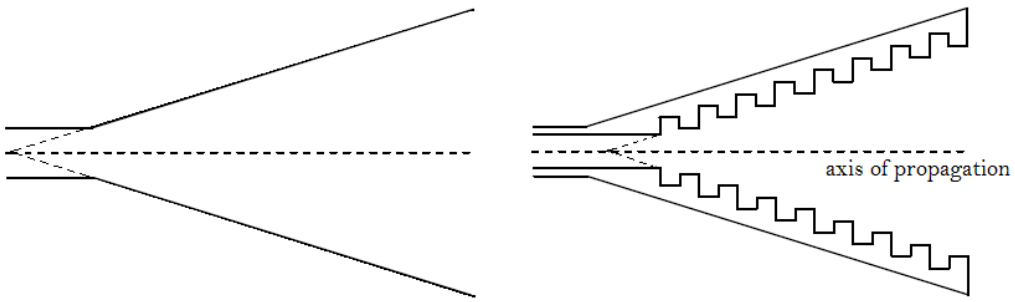

Figure 3.1 *Diagram of a cross section of a smooth walled (left) and corrugated (right) conical horn*

3.1.1 Smooth walled conical horns

A single moded smooth walled conical horn (see figure 3.2) fed by a circular waveguide will propagate only the dominant TE_{11} mode at the waveguide end when the radius of the throat of the horn is of the correct dimensions for the frequency of interest.

Smooth walled conical horns are easier to manufacture than their corrugated counterparts however when single moded they also produce lower quality beam patterns with asymmetric patterns, higher levels of side lobes and poorer polarisation purity [Goldsmith 1998]. These poor pattern characteristics compared to the more desirable quality of a corrugated horn beam can be explained by the field distribution. As the waveguide is assumed to be perfectly conducting the boundary conditions state that the field lines are perpendicular to the walls as the tangential E component is zero [Goldsmith 1998]. The adopted convention using cylindrical coordinates at $\theta = 0°$ also called the H-plane, the transverse E field must fall to zero at the boundary and so the field is highly tapered in this plane. At $\theta = 90°$ called the E-plane, the field does not fall to zero and so is less tapered in this direction. This explains the asymmetric patterns produced and the sharp edge to the distribution in the E-plane accounts for higher side lobes in this plane compared with the H-plane. A typical far-field pattern illustrating these characteristics is shown in the figure 3.6. Despite their relatively poor beam characteristics compared to corrugated horns they are still sufficient for many applications especially when multi-moded as the presence of higher order modes modifies the beam pattern, this is discussed in more detail in chapter 4 in the context of multi-moded pyramidal horns. Smooth walled conical horns are widely used due to their ease of manufacture especially at shorter wavelengths where manufacturing corrugations becomes complicated as is explained in the following section.

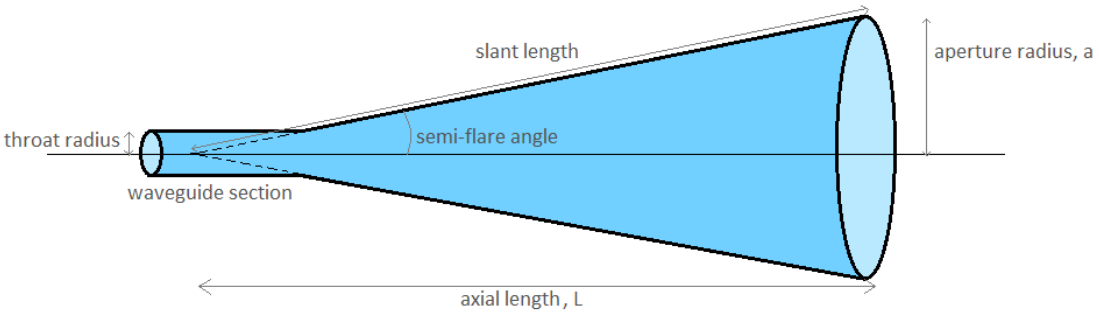

Figure 3.2 ***Geometry of a smooth walled conical horn***

3.1.2 Corrugated conical horns

Corrugated conical horns consist of a flared waveguide section with grooves or corrugations etched into the internal horn surface. The corrugations can be either perpendicular to the axis of propagation or perpendicular to the horn flared surface as shown in figure 3.3. The former are the subject of analysis in this chapter, they more common and easier to produce. The horns are usually fed by a smooth walled circular waveguide but there may also be a transition region to rectangular waveguide preceding this (standard WR-10 waveguide widely used for the frequencies of interest here). Where the aperture diameter is greater than 2λ [Colgan 2001] the optimum groove depth is λ/4 although at the throat of the horn the groove depth should be λ/2 slowly transitioning to λ/4 this ensures the TE_{11} mode of the smooth walled waveguide is well matched to the hybrid HE_{11} mode of the corrugated region so there is low return loss at the transition. The purpose of the corrugations is to force the boundary conditions to be the same for both the electric and magnetic fields unlike the smooth walled conical horn. This has the effect of tapering the field distribution equally in all directions at the aperture thus producing a symmetric field pattern with low levels of side lobes and cross polarisation. The boundary conditions imply that propagating TE or TM modes are equivalent to the symmetric hybrid HE_{11} mode as at the transition between the horn taper and corrugation the TE_{11} and TM_{11} modes have equal phase velocities [Clarricoats and Saha 1971], this combination forms the hybrid HE_{11}, mode when the mode phases are equal, which is the dominant mode of a single moded corrugated conical horn and offers a high quality beam in terms of symmetry and low cross polar levels. If the TE_{11} and TM_{11} modes are out of phase by 180˚ the hybrid mode is the EH_{11} mode. To understand how the corrugations achieve this balanced hybrid condition consider the tangential E field is zero and the transverse E field non zero for the smooth walled horn this causes the transverse E field to be completely out of phase at points 1/2λ apart. Thus a potential difference is created. With the corrugations present the current must flow an extra distance (λ/4), two currents flowing in opposite directions are now 180˚ out of phase. At the boundary both the tangential and transverse E field are now zero as any field is cancelled by an equal and opposite field. There should be many corrugations per wavelength [Colgan 2001] states that 3 per λ is sufficient.

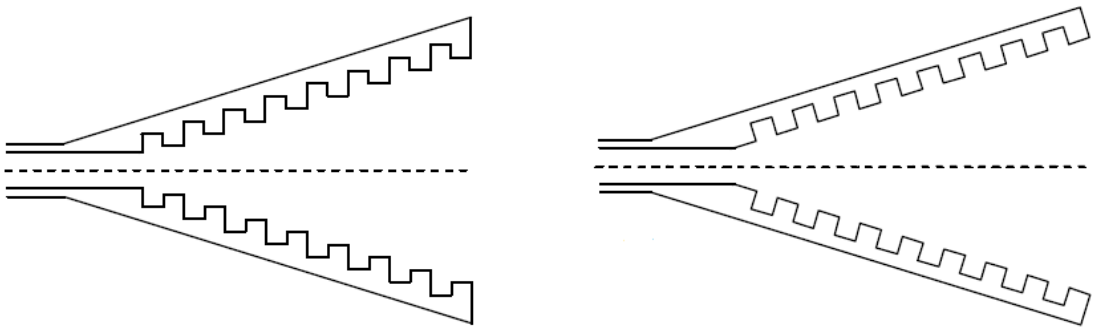

Figure 3.3 ***Cross section of a corrugated horn with the grooves perpendicular to the axis of propagation (left) and perpendicular to the horn flared surface (right)***

Corrugated horns at millimetre and sub-millimetre wavelengths are manufactured by electroforming. An aluminium mandrel with the inverse groove pattern is turned then metal that the horn is made from usually copper is electroformed onto the mandrel. The mandrel can then be chemically removed. A discussion on problems with the method and other forms of manufacturing can be found in [Clarricoats and Olver, 1984]. As the corrugation depth depends on the wavelength of radiation the horn is made to receive, at shorter wavelengths the manufacture of corrugated horns becomes difficult as the corrugations are so small. This also limits the bandwidth over which a corrugated horn operates while still offering the beam quality of the designed frequency.

3.2 GBMA of a smooth walled conical horn

As discussed in section 2.2 Gaussian beam mode analysis which propagates beams through ideal optical systems from a horn antenna begins with the assumption that the electric field at the horn aperture can be represented by a scalar field. In the case of a single moded smooth walled conical horn TE_{11} is the fundamental mode. The field at the aperture of the horn is essentially the TE_{11} mode with a spherical wave front due to the flare of the horn, $exp\left[-j\frac{kr^2}{2L}\right]$ [Olver 1994] where L is the axial length of the horn. For a horn of aperture radius a the field can be expressed in cylindrical coordinates as [Murphy 1988],

$$E_{ap}(r,\theta) = A\left[\left[J_0\left(x\frac{r}{a}\right) + J_2\left(x\frac{r}{a}\right)cos2\theta\right]\hat{\imath} + \left[J_2\left(x\frac{r}{a}\right)sin2\theta\right]\hat{\jmath}\right]exp\left[-j\frac{kr^2}{2L}\right] \quad (3.1)$$

Where J_0 and J_2 are the 0th and 2nd order Bessel functions and $x = 1.841$.

At any point, although most appropriately at the horn aperture, the field can be written as a linear combination of either Hermite Gaussian or Laguerre Gaussian modes discussed in section 2.2. As the horn is conical the Laguerre Gaussian mode set will be used for simplicity. For cylindrically symmetric beams the aperture field can be written [Murphy and Egan, 1992],

$$E(r,\theta) = \sum_{n=0}^{\infty} A_n \Psi_n\big(r, z; W(z), R(z)\big) \quad (3.2)$$

Ψ_n are the Laguerre Gaussian modes given by equation 2.11 and A_n are the normalised mode coefficients for the mode set determined by the overlap integral between the TE_{11} mode described by 0 and 2nd order Bessel functions (equation 3.1) and the Laguerre Gaussian modes,

$$A_n = \iint E(r', z_0)\big[\Psi_n\big(r', z_0; W(z_0), R(z_0)\big)\big]2\pi r' dr' \quad (3.3)$$

From this the field can be described at any other point in both the near and far field by propagating the individual modes and re-summing equation 3.2. As only n = 0 and 2 modes couple to the TE_{11} field, E can be expressed at any point by equation 3.4 where z is the axis of propagation [Murphy 1988],

$$E(r,\theta,z) =$$
$$exp\left(-\frac{r^2}{W(z)^2} - j\frac{\pi r^2}{\lambda R(z)} - jkz + j\emptyset_0(z)\right)\left[\sum_m A_{m0}L_m\left(\frac{2r^2}{W(z)^2}\right)\exp(2mj\emptyset_0)\,\hat{\imath} + \right.$$
$$m2r2Wz2m2Lm22r2Wz2\exp 2m+2j\emptyset 0z[Am2cos2\theta i+Am2sin2\theta j] \quad (3.4)$$

There are an infinite number of solutions to the Laguerre Gaussian modes however a finite set of modes can be used to represent the field, this is more computationally efficient. It is desirable to use as few modes as possible to decrease computation time while still accurately representing the field. Within the model, the choice of beam width W_{in} and the phase radius of curvature at the aperture R_{in} given

by equations 2.13 and 2.14 are crucial to provide an accurate description of the field and the optimum choice of W in particular depends on the mode set used [White 2006]. W can be chosen so that the power in the fundamental mode is maximised but this is only accurate if it is a simple Gaussian propagating. In the case of a smooth walled conical horn the power coupling must be maximised to the total number of modes used. [Goldsmith 1998] states that the optimum choice for a smooth walled conical horn where the beam is symmetric is $W = 0.76a$. However for an asymmetric beam $W_x = 0.88a$ and $W_y = 0.64a$ (assuming a Hermite Gaussian set of modes is used, where there are two values of W are used due to the asymmetry), where W is written in terms of the aperture radius a. This can be explained by the fact the field at the aperture is highly tapered in the H plane as discussed in section 3.1.1, see figure 3.4, hence the beam width for optimum coupling is larger along one axis. The radius of curvature can be taken to be the slant length of the horn.

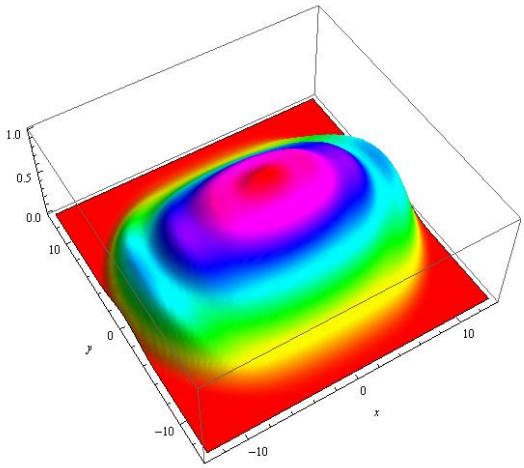

Figure 3.4 Aperture field of a smooth walled conical horn

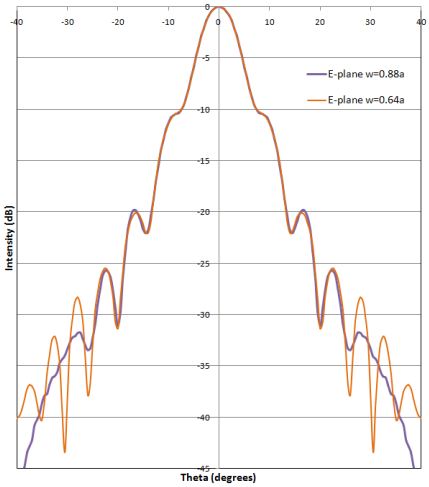

Figure 3.5 Far field E-plane of a conical horn vary values of W

Code written in Mathmatica using the Gaussian beam mode technique was developed to investigate the near and far field properties of a smooth walled conical horn of aperture radius 4.41 λ and length 29.667 λ where λ = 3mm. Figure 3.5 above shows the E-plane far field results of optimum coupling for both axes. There is not much difference between the two values, effects are only seen in the side lobes at low levels of power where 30 modes are used in the calculation. Figure 3.6 shows both the E and H-plane results for the same horn using 30 modes and a value of $W = 0.64a$. The asymmetry of the field can be seen as well as the presence of the first side lobe at -10

dB in the E-plane. GBMA far-field results are compared and verified against results obtained using the more rigorous mode matching technique in the following sections.

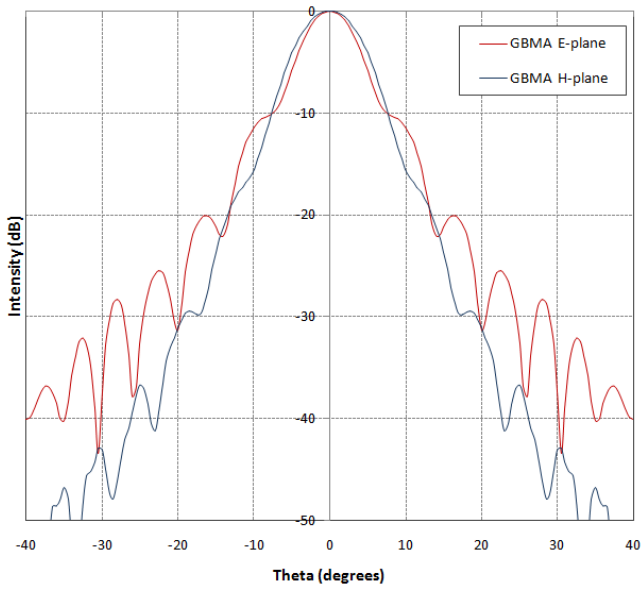

Figure 3.6 ***Far-field pattern of a smooth walled conical horn produced by GBMA, λ=3mm***

3.3 Mode matching technique applied to smooth walled conical horns

A smooth walled conical horn of the same geometry as in the previous section was modelled in µWW following the description of the software provided in section 2.7.2. Again the dimensions are given by - throat radius = 0.4583λ, aperture radius = 4.41λ and length = 29.667λ where λ = 3 mm. The horn was analysed over the bandwidth 90 GHz to 110 GHz. Important input parameters in µWW for analysis using the mode matching technique such as the cut off frequency, modes used and steps for modal analysis were found through empirical methods, testing previously established rules and comparing predictions with SCATTER where an accurate beam pattern was already calculated.

In determining the number of waveguide sections used in modal analysis a rule of thumb developed by [Kühn and Hombach 1983] states that for horns with aperture diameter greater than 1λ (as in this case) the horn should be divided into 30 sections for every wavelength change in diameter. If the aperture is less than 1λ in diameter

the diameter difference between consecutive junctions should be 1/30th the diameter of the waveguide at the horn throat. The far field patterns and S_{11} of several models with increasing modal steps were analysed in µWW. Once the results are seen to converge a sufficient number of steps is determined for the analysis. The far-field beam pattern results at 100 GHz are shown in figure 3.7. Any increase beyond 200 steps produces only slight changes in the results while 50 waveguide sections describing the horn produces very poor results. According to Kühn and Hombachs rule 240 sections should be sufficient for this horn.

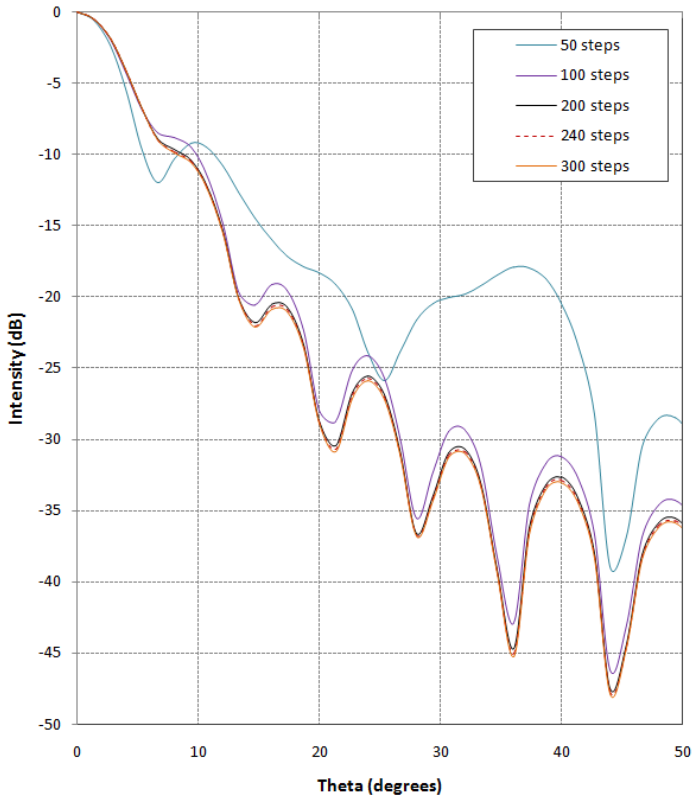

Figure 3.7 ***Far field E-plane of a smooth walled conical horn for increasing steps used in the modal analysis modelled in µWW***

The same approach is used in determining the cut off frequency. Mician suggest a cut off frequency 10 times the mid-point analysis frequency as a suitable starting point for the analysis and that this should then be increased until the results are seen to converge. Results obtained for each increase in cut off frequency are shown in figure 3.8. The greatest difference is seen at a cut-off frequency of 600 GHz (6 times the operating frequency) although the results are still quite similar. Beyond 1000 GHz the change in S_{11} is very small. Increasing the cut-off frequency has the greatest effect on

computation time compared to increasing modes or modal steps. The number of modes used in the analysis is specified by the percentage of the cut-off frequency that will be used for each element, modes above the cut-off frequency percentage do not propagate, 60 modes were used in the analysis.

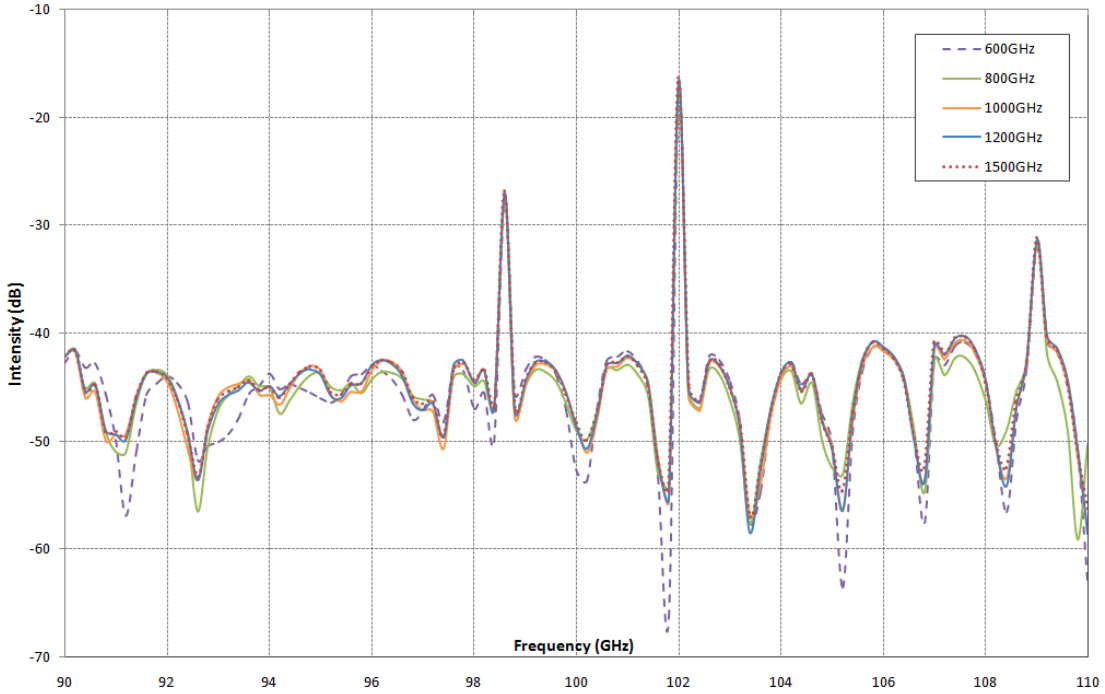

Figure 3.8 ***S_{11} of a smooth walled conical horn modelled in µWW with increasing cut-off frequency***

A similar approach was taken in modelling the horn in SCATTER, increasing the steps and modes used in the analysis until results converged, although there is no cut off frequency input in SCATTER. Using this method 300 modal steps and 60 modes were found to produce convergent results consistent with µWW. The far field and scattering parameters of the horn determined using SCATTER are compared against µWW results in figures 3.9 and 3.10. Looking figure 3.9, the far field results, there is good agreement between the two packages although there is some disagreement in the side lobe intensity this is most noticeable in the H-plane. In determining the scattering parameters µWW performs a frequency sweep between 90 GHz and 110 GHz in 101 steps taking 90 minutes for convergent results while SCATTER calculates the results one frequency point at a time. The frequency must be changed and the code ran again for each frequency point. In this case this takes about 4 minutes to calculate the S-parameters at each point using SCATTER.

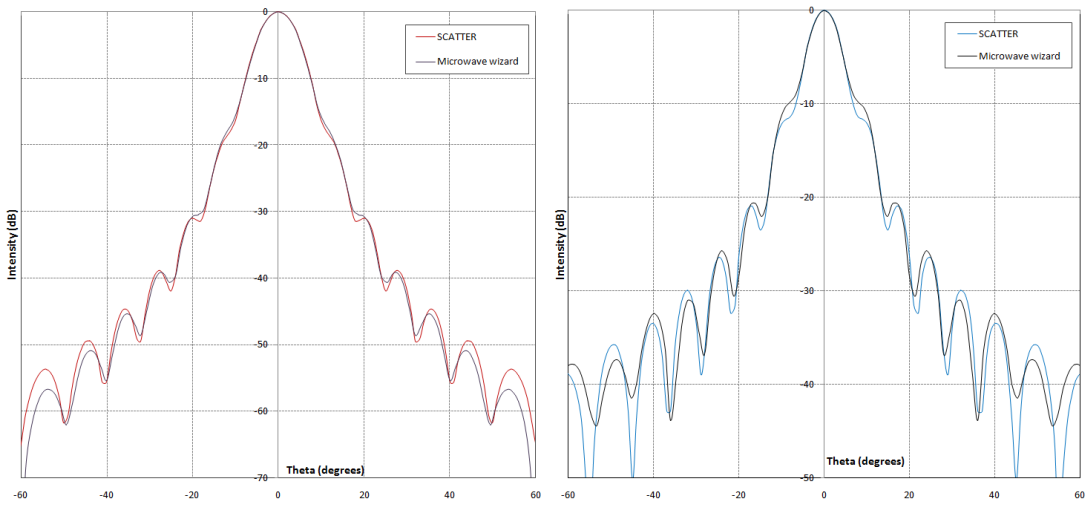

Figure 3.9 ***H-plane (left) and E-plane (right) far field results of a smooth walled conical horn modelled in Microwave wizard and SCATTER.***

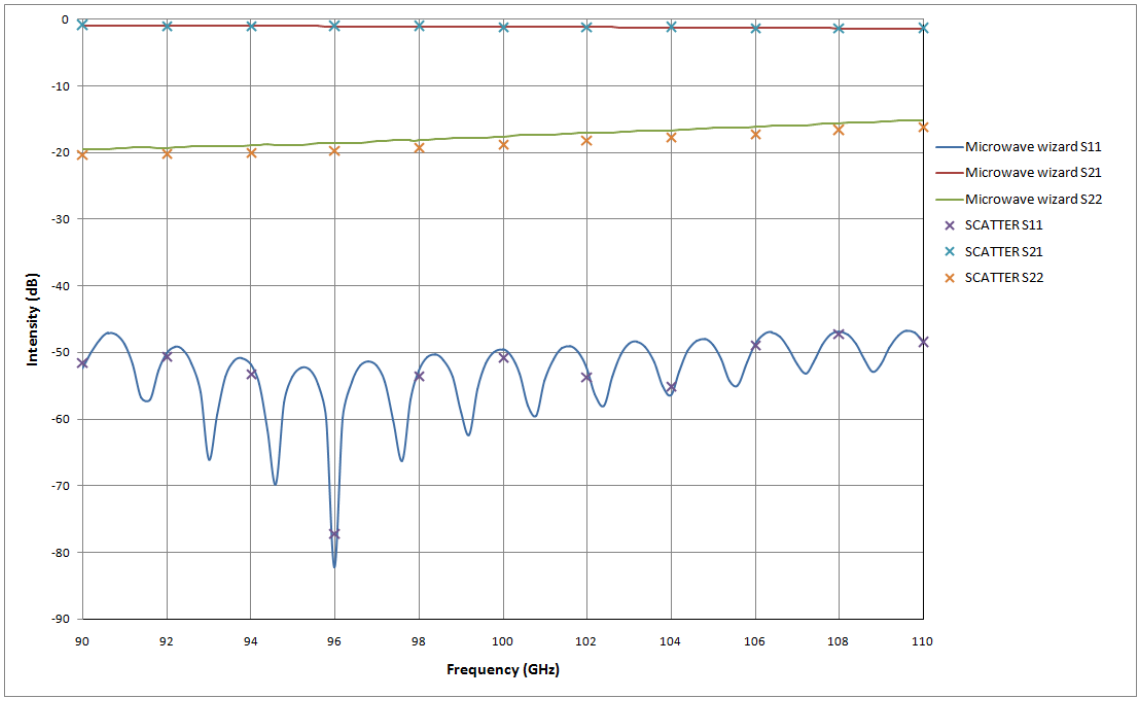

Figure 3.10 ***Fundamental TE_{11} mode scattering parameters of a smooth walled conical horn modelled in both Microwave wizard and SCATTER***

Figure 3.11 shows the far field E-plane results of the same smooth walled conical horn operating at 100 GHz determined by Gaussian beam mode analysis and the two packages using the mode matching techniques Microwave wizard and SCATTER. The GBM approach agrees well with the µWW results and it appears that the initial discrepancy between the two mode matching methods may be due to implementation within SCATTER. Although GBMA is based on approximations it still

produces accurate results as can be seen when compared against the more extensive mode matching techniques, this method is also by far the quickest to perform the analysis taking less than half minute to determine the far field results compared to 3 - 4 minutes for µWW and SCATTER to calculate far field results.

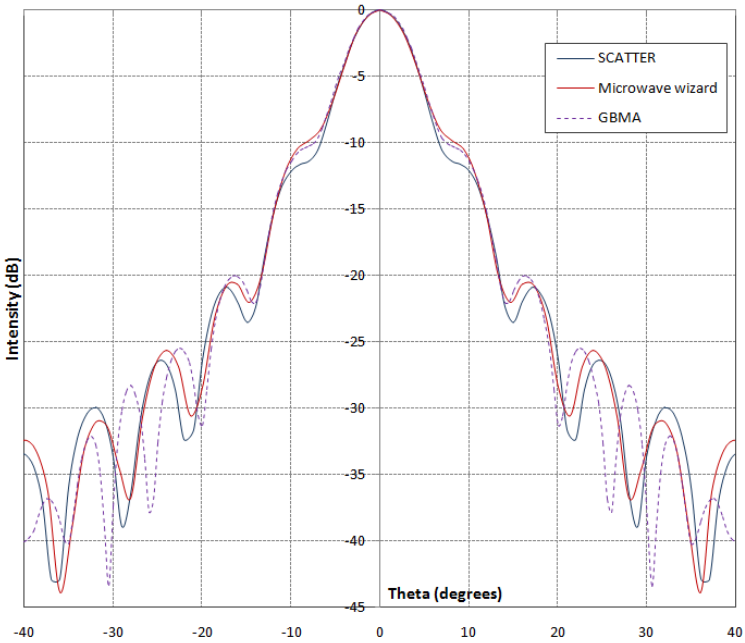

Figure 3.11 ***Far field pattern of a smooth walled conical horn operating at 100GHz modelled in SCATTER, Microwave wizard and using Gaussian beam mode analysis.***

Once a suitable cut off frequency had been determined for a horn operating at 100 GHz models of horns operating at higher frequencies were produced to investigate the effects of cut off frequency within µWW at higher frequencies. The conical horns were suitably scaled, for example a horn operating at 300 GHz (3 times the original 100 GHz frequency) has length and aperture dimensions that are that of the original horn divided by three. Another horn to operate at 600 GHz was also modelled (original dimensions divided by six), these horns can be seen in figure 3.12a and b.

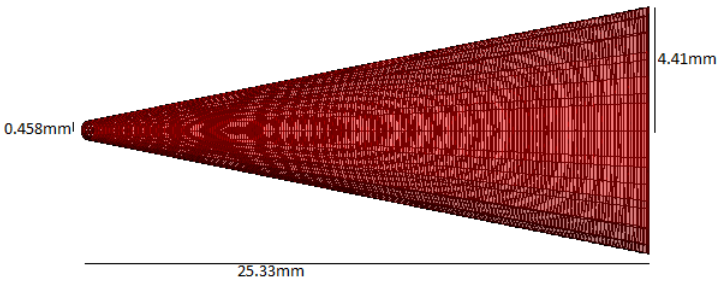

Figure 3.12a ***300GHz conical horn***

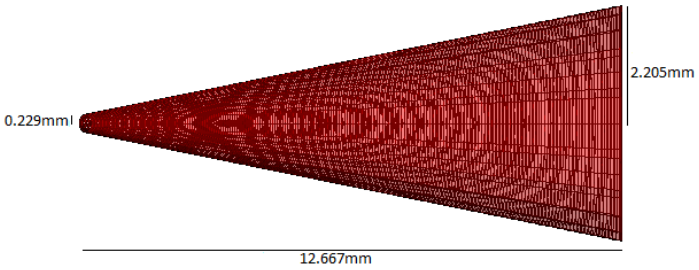

Figure 3.12b 600GHz conical horn

Models were ran using varying cut-off frequencies for each horn until convergence was seen in the results, in the same way as above. It was determined that as operating frequency increases the computation cut-off frequency can be lowered below the recommended 10 times the operating frequency. While the cut-off frequency is known to specify how many modes will propagate through the system its exact implementation and effect within µWW is unknown, the recommended rule is given for systems operating at microwave frequencies. In the following chapters horns operating at THz frequencies are modelled and consistent with these results it was found that the cut-off frequency could be lowered considerably from the recommendation at these much higher operating frequencies. The results found are summarized in table 3.1 below. Steps used in the modal analysis to represent the waveguide sections replacing the profile of the horn must still be sufficiently short (λ/10) to accurately describe evanescent modes excited by scattering to higher order modes.

Wavelength	Operating frequency	Cut-off frequency	Rule established
3 mm	100 GHz	1000 GHz	10 × operating freq
1 mm	300 GHz	2000 GHz	6.6 × operating freq
0.5 mm	600 GHz	4000 GHz	6.6 × operating freq
70 µm	4 THz	12000 GHz	3 × operating freq

Table 3.1 Microwave wizard cut-off frequency in relation to operating frequency

3.4 Mode matching technique applied to corrugated horns

A similar approach as described in the analysis of smooth walled conical horns (section 3.3) is taken in the analysis of corrugated horns using the mode matching technique although this time the number of circular waveguide sections defining the profile of the horn does not need to be specified as it is the corrugations of the horn itself that defines this.

Inputting the geometry and modelling a corrugated horn within μWW can be done in several different ways. There are corrugated horn elements in the library although there use is somewhat limited as it may not be possible to describe the exact profile of a particular horn using the given input parameters. Another option is to read in a file describing the geometry of the horn. The import .stl file (STereo Lithography) option will perform the finite element method of analysis on the horn however this option was found to be not ideal for larger horns operating at high frequencies (100GHz) due to memory constraints imposed by the finite element method of analysis. There is also an option to read in the external data profile of a circular horn, the S-parameters of the horn are calculated using the mode matching technique and this method was found to be the most suitable in this case.

The horn has dimensions r_{in} = 1.2578 mm, r_{out} = 8.7 mm, length = 149.25 mm with 191 corrugations and operating between 85 GHz and 115 GHz. The results of the far field analysis, at the mid frequency point 100 GHz, from both μWW and SCATTER are shown in figure 3.13. It can be seen that there is excellent agreement between the two packages in both the E and H planes. Analysing the far field pattern it is seen from the E and H plane cuts that the beam pattern is symmetric also the first side lobes are at a very low level (-40 dB) as would be expected for a corrugated conical horn. The S_{11} of the fundamental hybrid HE_{11} mode produced by both packages are shown in figure 3.14 and it can also be seen here that there is excellent agreement between the packages. Within the horn structure, after the fundamental mode limiting entrance, the presence of higher order modes will cause power to be scattered between the fundamental and these higher order modes and also between the higher order modes themselves. This is seen in the S_{21} and S_{22} scattering parameters. Microwave wizard and SCATTER show the same agreement in power scattering from these higher order modes as well.

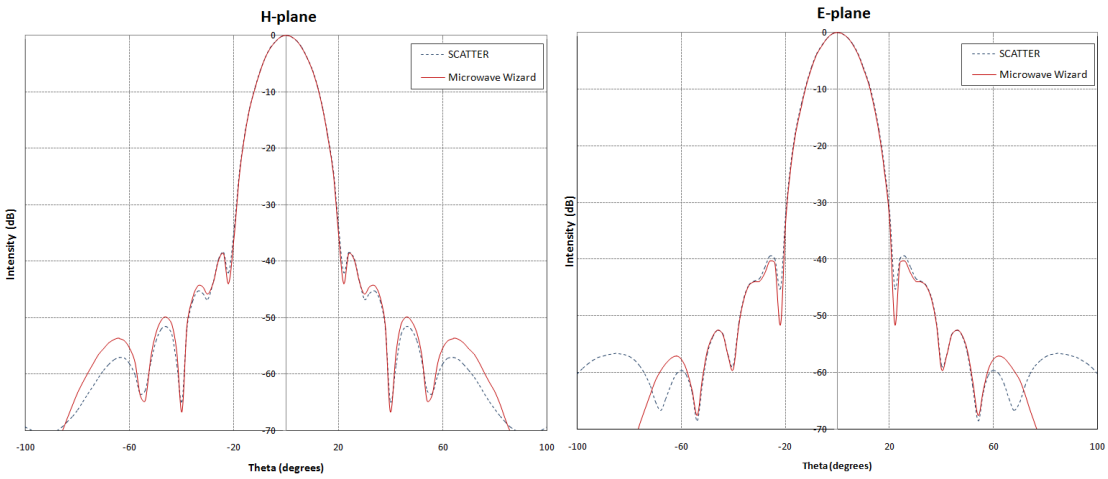

Figure 3.13 ***Left E-plane and right H-plane far field radiation patterns for a corrugated conical horn produced in both SCATTER and µWW***

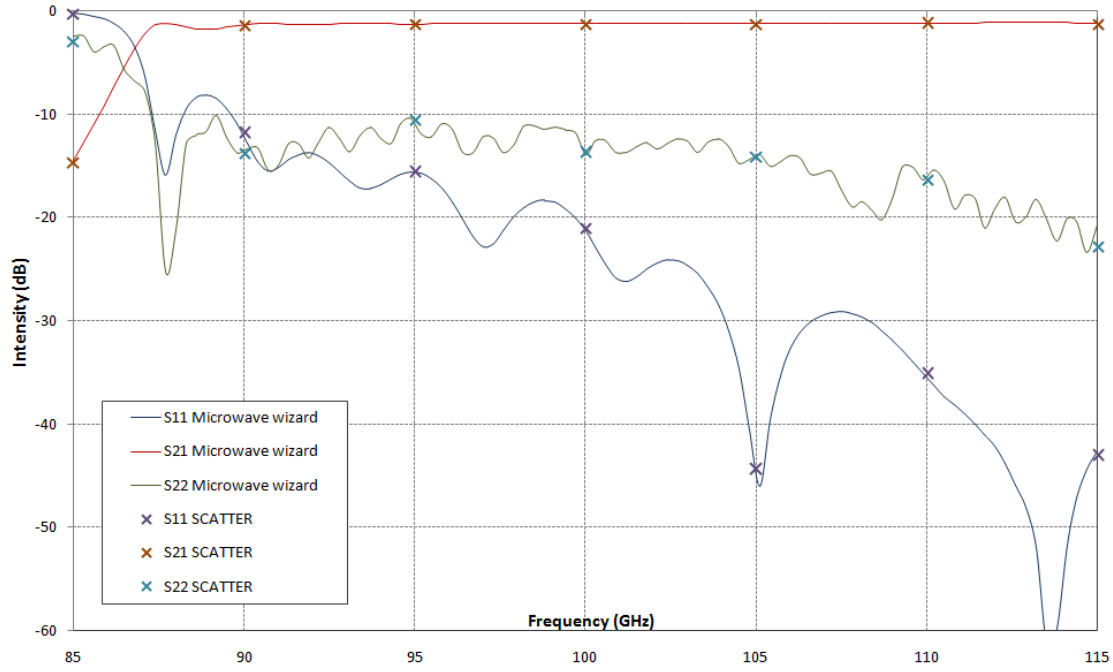

Figure 3.14 ***Scattering parameters of the fundamental HE_{11} mode for a corrugated horn in both µWW and SCATTER***

Analysing figure 3.14 it is evident that the corrugated horn is not designed to operate at 85 GHz as the transmission through the horn is low (-15 dB) and the reflection at both ports is higher than the transmitted power. Above ~87.5 GHz transmission through the horn increases and reflected power decreases signifying the horn was originally designed to operate above 90 GHz.

3.5 Conclusion

In this chapter both smooth walled and corrugated conical horn antenna were analysed using two very different techniques, Gaussian beam mode analysis and the mode matching technique. The mode matching technique was implemented by two separate packages, a commercially available software package Microwave Wizard and SCATTER code written and developed at NUI Maynooth. In the mode matching analysis both far-field and scattering parameters of the smooth walled and corrugated conical horn are produced and good agreement is seen between the two packages, providing verification to the NUI Maynooth developed code. Gaussian beam mode analysis utilising the Laguerre Gaussian mode set was used to obtain a far-field pattern of the same smooth walled conical horn analysed by the mode matching technique and again there is good agreement between the different methods. Comments on the efficiency and speed with which each package can produce results are made within the work. While the GBM approach cannot be used to the same level of accuracy and gives no information on the transmission and reflection properties of the horn, the results shown prove it is sufficient at accurately reproducing the radiation pattern of a conical horn antenna, its computation time is far quicker than that of the more exhaustive mode matching technique while still providing accurate results. This method can be extended to model further propagation of the beam through quasi-optical components.

CHAPTER 4

Analysis of Pyramidal Horns

4.1 Introduction

In this chapter Gaussian beam mode analysis and mode matching techniques described in chapter 2 are applied to the analysis of pyramidal horns for the prediction of field patterns and return loss S_{11} parameters. Pyramidal horns are essentially flared sections of rectangular waveguides, flared in both the E and H planes to differing degrees. Variables associated with the geometry of a pyramidal horn are shown in figure 4.1. *a* and *b* are the width and height of the waveguide feeding the horn (commonly a WR-10 waveguide 2.54 mm x 1.27 mm), *A* and *B* are the aperture width (H plane) and height (E plane). There are generally two different values of horn flare angle θ and axial length *L* depending on whether the E or H plane is being referenced although the aperture of the horn may be either rectangular or square (with $A = B$). The differing flare and aperture widths in the orthogonal planes are used to compensate for the far-field shape asymmetry between the E and H planes. The walls of the horn are generally smooth, although corrugated pyramidal horns have been manufactured they are uncommon in the sub-millimetre region and will not be discussed here.

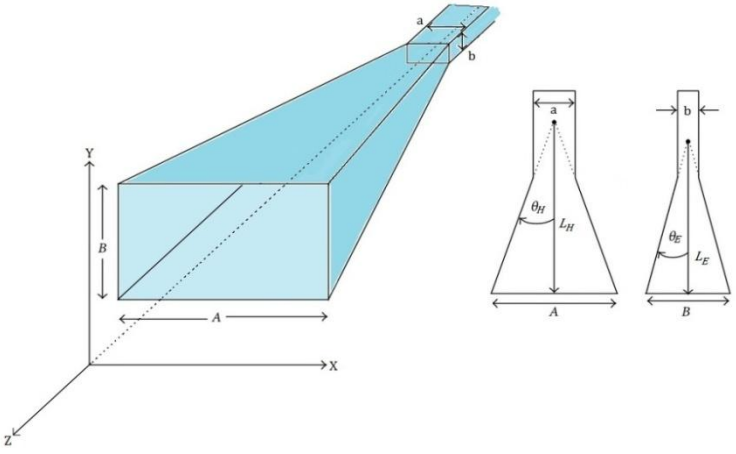

Figure 4.1 ***Geometry of a pyramidal horn***

The flared waveguide couples radiation from free space to the waveguide detectors, with the large aperture (compared to the wavelength) producing higher directivity and a better impedance match to free space than a simple waveguide as with the conical horns discussed in chapter 3. For a single moded pyramidal horn, for example one designed to operate at 100 GHz fed by a WR-10 waveguide, the TE_{10} mode is the dominant mode i.e. the only mode that will propagate within the throat of the horn towards the detector via a single mode waveguide where all modes but the fundamental mode are evanescent. For multi-moded horns the next highest order mode is determined by the ratio of *a/b*. Many millimetre and sub-millimetre single-moded rectangular waveguides have dimensions *a = 2b*, as with the WR-10. The field distribution of the TE_{10} mode was found in section 2.3 (waveguide modes), the only component of the electric field of the TE_{10} mode is the E_y component which has the form,

$$E_y = E_0 \cos\frac{\pi x}{a} \tag{4.1}$$

In the E-plane the electric field is similar to a uniformly illuminated slit while the in the H-plane it varies sinusoidally and is symmetrical about the central axis. Thus for a single moded pyramidal horn the aperture field is essentially the TE_{10} field with an extra phase term determined by the influence of the flare angles of the horn. Where θ_H and θ_E are the flare angles and L_H and L_E are the axial lengths in both planes, the aperture field is given by [Olver 1994]

$$E_a(x', y') = E'_y(x', y') = E_0 \cos\left(\frac{\pi x'}{A}\right) exp\left[-j\left(\frac{k}{2}\left(\frac{x'^2}{L_H} + \frac{y'^2}{L_E}\right)\right)\right] \tag{4.2}$$

The electric field is uniform in the E-plane but tapers to zero in the H-plane across the aperture. If the antenna aperture in both E- and H- planes is larger than 1λ, the pattern in one plane is largely independent of the aperture dimension in the other plane [Kraus 2002]. Pyramidal horns produce high side lobe levels particularly in the E plane due to the non-tapered field distribution at the aperture, cross polarisation levels are low. Due to differing flare angles the phase centre is not the same in both planes meaning it is not possible to define a single position from which the radiation is considered to emerge from, this impairs the efficiency of the pyramidal horn and makes it an uncommon choice as a feed for reflector antennas, although still common

in many other quasi-optical systems. It was mentioned earlier there is a special case of pyramidal horn where *A = B* such that the horn has a square aperture. These square aperture pyramidal horns have the same flare angle and aperture length in both planes thus eliminating the phase centre problem and making them suitable candidates for quasi-optical systems such as the focal plane array of the SAFARI instrument discussed in section 4.4. Firstly an analysis of the characteristics of a single moded pyramidal horn antenna with a rectangular aperture is provided using the mode matching technique and then Gaussian beam mode analysis.

4.2 Analysis of a pyramidal horn using mode matching technique

A pyramidal horn designed to operate over the 75 - 110 GHz frequency band with dimensions *A* = 27 mm, *B* = 20 mm and slant length 63.5 mm fed by a WR-10 waveguide of length 11.2 mm was modelled within µWave Wizard whose analysis is based on the mode matching technique. As with the conical horn modelled in section 3.3 cut-off frequency, modes used in the analysis and the number of uniform waveguide sections used to replace the profile of the horn are important input parameters in the µWW model and must be chosen carefully to accurately describe the system without unnecessarily increasing computation time. With each waveguide section of the order of 1/10th of the wavelength, 200 waveguide sections were used in the model to replace the horn profile. Due to memory requirements the cut-off frequency was unable to be increased above 850 GHz (8.5 times the mid-point operating frequency) without decreasing the modal steps, these values were found to be sufficient for the analysis with 40 modes used. The far-field pattern is shown in figure 4.2.

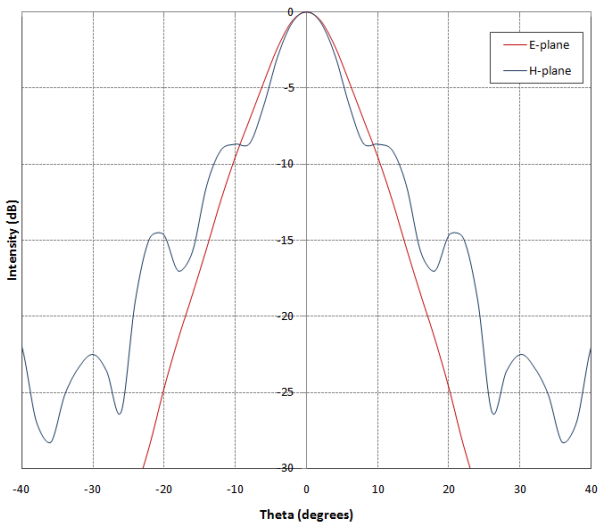

Figure 4.2 ***Far-field pattern of a single moded pyramidal horn produced in µWave Wizard***

Analysis of a pyramidal horn within µWW proved quite computationally inefficient compared to a conical horn, this led to memory constraints and extremely long computation times suggesting µWW is not entirely suitable for the analysis electrically large pyramidal structures at high frequencies. Computation of the single moded pyramidal horn designed to operate at 100 GHz took several days running a 64-bit computation on a computer with 12 GB of RAM, in comparison a single moded smooth walled conical horn operating at 100 GHz will run is less than two hours on the same machine. Due to boundary conditions imposed by the walls of the horn, mode distributions within pyramidal horns require longer computation times as the fields do not simplify as easily compared to the symmetric boundary conditions within conical horns.

The far-field pattern produced in µWW is compared against those obtained by SCATTER code using the mode matching technique applied to pyramidal horns, the results can be seen in figure 4.3. Reasonable agreement can be seen between the two packages although it should be noted that computation within µWW was restricted by computational power. The mode matching technique used within SCATTER is as is described in section 2.4 but differs from that used in the analysis of a conical horn (section 3.3) in the calculation of the mode field components. Fields within cylindrical and rectangular waveguides were found in section 2.3, in the cylindrical waveguide analysis field distributions simplify to Bessel functions of the first kind and their

derivatives, however with rectangular waveguides replacing the pyramidal horn boundary conditions lead to $2n^2$ modes to be calculated. This explains why the mode matching technique applied to pyramidal horns is computationally extensive leading to memory constraints and long computation times. While both SCATTER and µWW are applying the mode matching technique to a pyramidal structure, the SCATTER codes computation time is still significantly shorter than that of µWW and has the benefit that the source code is available, the underlying methods and techniques can easily be investigated.

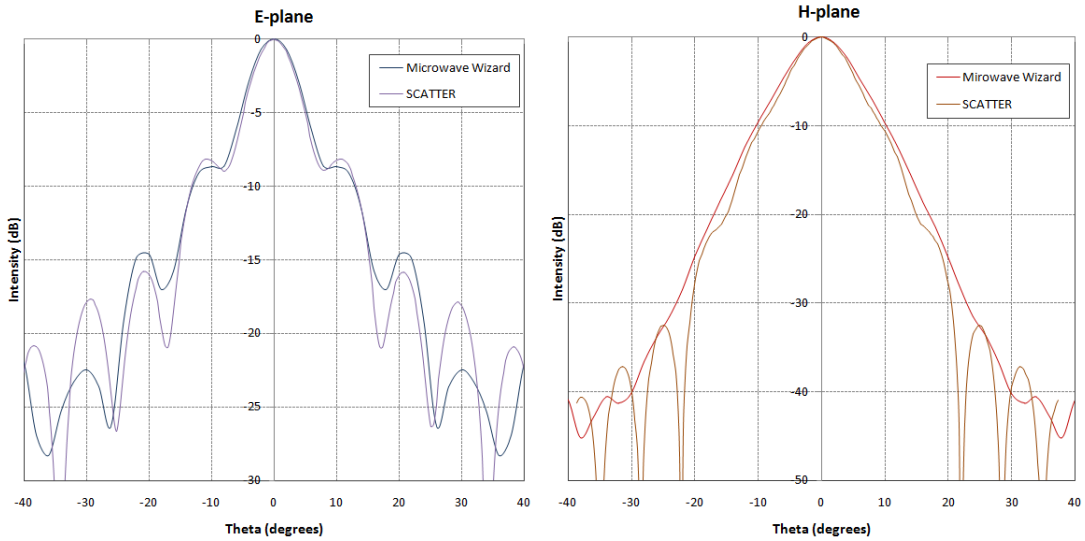

Figure 4.3 ***E- and H-plane far-field of a pyramidal horn produced in µWW and SCATTER, both using the mode matching technique.***

4.3 GBMA of a pyramidal horn

GBMA of the same pyramidal horn described in the preceding section was undertaken using code written within Mathmatica. The field at the aperture of the horn is given by equation 4.2 previously as,

$$E_a(x',y') = E'_y(x',y') = E_0 \cos\left(\frac{\pi x}{A}\right) exp\left[-j\left(\frac{k}{2}\left(\frac{x'^2}{L_H}+\frac{y'^2}{L_E}\right)\right)\right]$$

where L_H and L_E are as defined in figure 4.1. This is the product of the TE_{10} field distribution and a phase front caused by the horn flare, where the primed coordinates represent the aperture coordinates. The Hermite Gaussian mode set is best used to describe propagation from rectangular apertures. The normalized Hermite coefficients

are determined at the aperture by computation of an overlap integral between the aperture field E_a and the Hermite Gaussian mode set Ψ_{mn}. The mode set is given in section 2.2.3 as

$$\Psi_{mn}(x,y,z) = h_m\left(\sqrt{2}x/_W\right) h_n\left(\sqrt{2}y/_W\right) \exp\left[-jk\left(\frac{x^2+y^2}{2R}\right) + j\phi_{mn}\right] \exp[-jkz] \quad (4.3)$$

where

$$h_m\left(\sqrt{2}x/_W\right) = \frac{H_m\left(\sqrt{2}x/_W\right)\exp\left[-x^2/_{W^2}\right]}{\sqrt{2^{m-\frac{1}{2}}m!W\sqrt{\pi}}} \quad \text{and} \quad h_n\left(\sqrt{2}y/_W\right) = \frac{H_n\left(\sqrt{2}y/_W\right)\exp[-y^2/W^2]}{\sqrt{2^{n-\frac{1}{2}}n!W\sqrt{\pi}}}$$

H_m and H_n are Hermite polynomials of order *m/n* and h_m and h_n are normalised Hermite Gaussian functions. W, R and ϕ have their usual meanings within GBMA. The overlap integral is given by [Murphy and Egan 1992]

$$A_{mn} = \iint E(x',y',z_0)\,[\Psi_{mn}(x',y',z_0;W(z_0),R(z_0)]^* dx'dy' \quad (4.4)$$

The individual modes are propagated to the near or far field and equation 4.5 is re-summed to give the radiation pattern at that point,

$$E_f(x,y,z) = \sum_{n=0}^{\infty}\sum_{m=0}^{\infty} A_{mn}\Psi_{mn}(x,y,z;W(z),R(z)) \quad (4.5)$$

where *z* is the propagation distance, z_0 is the *z* origin at the aperture and primed coordinates represent the aperture coordinates and un-primed coordinates the point to where the field is propagated. In this way both the near and far field of pyramidal horns can be calculated by GBMA using the Hermite Gaussian mode set.

The far-field of the pyramidal horn described earlier was found using this method with 30 modes used in the analysis and a value of *w/A* = 0.13. The pattern at 100 GHz is shown in figure 4.4, it can be seen that the E-plane is less tapered and shows more side lobe structure than the H-plane.

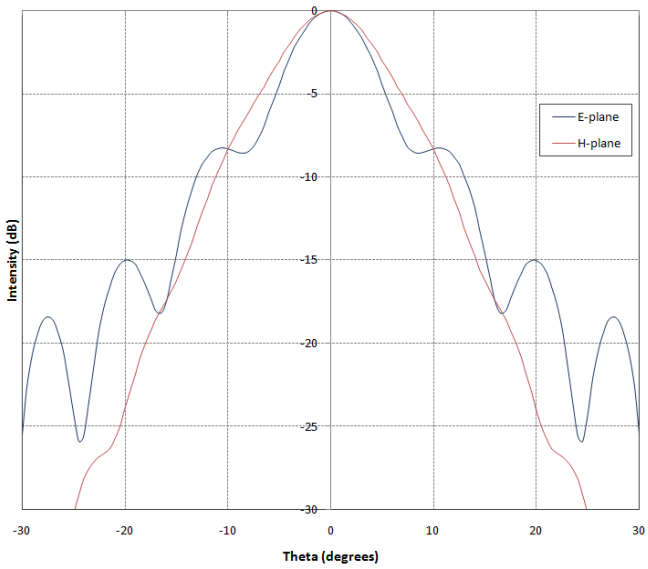

Figure 4.4 ***Far-field pattern of a pyramidal horn at 100GHz obtained using GBMA***

When compared with far-field patterns of the same horn obtained using the mode matching technique, figure 4.5, good agreement is seen between the two methods particularly in main lobe and first side-lobe levels of the E-plane. The H-plane shows less agreement, with the GBMA slightly over estimating the beam width. The E-plane field has a simple uniform distribution whereas the H-plane field's profile is harder to reproduce within the model in terms of Hermite modes, the correct choice of beam mode set and trying to reproduce highly tapered profiles. The GBM analysis is of course more approximate than the full modal matching description and cannot be used to the same degree of accuracy, the program is however significantly quicker to run and has many applications when approximating the field shape to the first order may be useful to quickly estimate the horn's response (e.g. the first order estimation of a field coupling to an optical system).

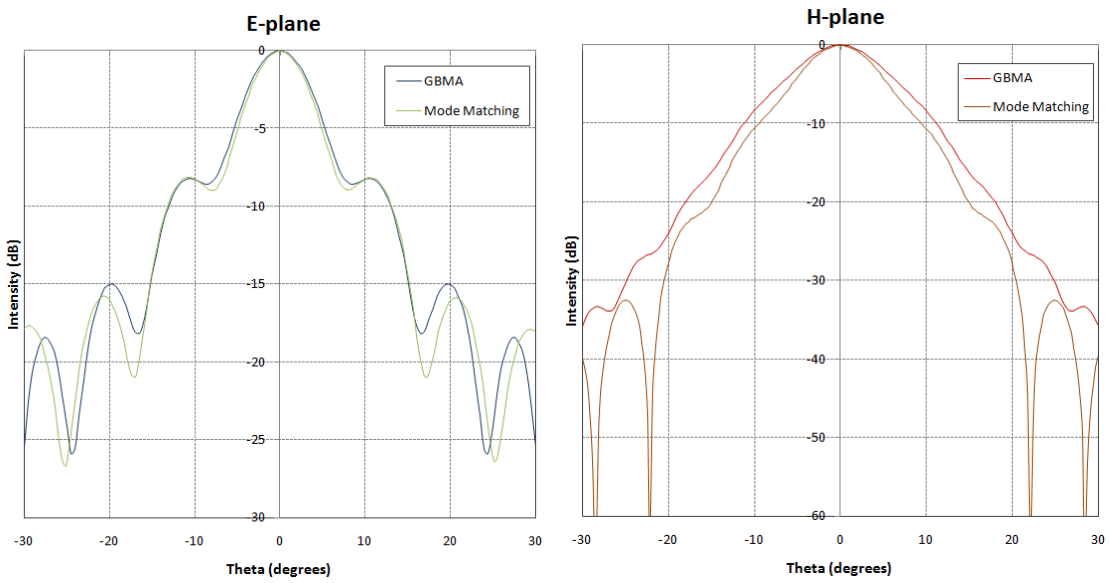

Figure 4.5 ***Far-field pattern of a pyramidal horn at 100 GHz produced by GBMA and mode matching techniques***

4.4 SAFARI horn

The SAFARI instrument of SPICA was first introduced in chapter 1, the SAFARI S-band focal plane consists of an array of SAFARI S-band horns that couple radiation to absorbers within a cavity placed at the throat of each horn. An analysis of the array of SAFARI horns, specifically the crosstalk between them, is presented in chapter 5 (section 5.5). Firstly a µWave Wizard model of a single isolated SAFARI horn was produced to determine suitable cut-off frequencies, modal steps and number of modes used in the analysis for a single horn before being modelled as part of an array. The SAFARI horn antennas have a square aperture and so are the special case of pyramidal horns discussed earlier where $A = B$, thus a single flare angle and a single axial length describe the horn in both planes. The SAFARI horns are two flared square waveguide sections with differing flare angles coupled together, this can be seen in figure 4.6.

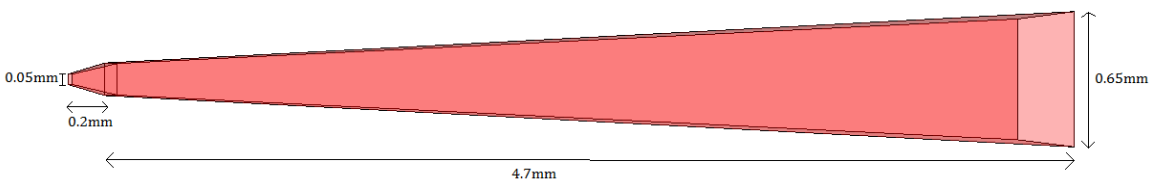

Figure 4.6 ***Geometry of the SAFARI S-band horn antenna***

The tip of the horn has a wide flare angle of 30˚ and length 0.2 mm this is coupled to a longer 4.7 mm long section of flare angle 6˚, the entrance aperture of the horn has a diameter of 0.65 mm and exit aperture (at the throat of the horn) of 0.05 mm. The stepped tip of the horn is required to improve thermal conduction during manufacturing, reducing burning and improving tip quality [Griffin, Technical note to the ESA]. The horns operate over the 35 µm - 70 µm waveband, this corresponds to a frequency range of 4.285 - 8.57 THz, this is significantly higher than the 100 GHz horns modelled previously and the microwave systems µWW was originally designed to operate at with millimetre wavelengths.

The horns are multi-moded meaning the horns radiate or receive more than one coherent mode, that is more than one mode will propagate through the throat of the horn to where the detectors are placed. With multi-moded horns, the higher order modes are used to enhance radiation patterns of the horn and/or produce extra information at the horn terminals i.e. receive a greater signal at the detectors placed at the throat of the horn. This makes them a common choice in astronomical receiver systems such as SPICA where the horns are receiving very faint signals from the sky.

4.4.1 SAFARI horn scattering parameters

The horn operates over a relatively large range, cut-off frequency and modal steps to be used in the analysis will increase with operating frequency. Separate models were run over narrower frequency bands to increase computational efficiency. For example initially suitable cut-off frequencies and modal steps were determined over the 4.285 - 5 THz range. The general rule of dividing the horn into waveguide sections 1/10th of the wavelength was found to hold true at these higher frequencies and produced convergent results with 700 taper steps in the longer waveguide. Following on from results found in chapter 3 it was established that the cut-off frequency does not have to be set as high as is recommended by Mician for these higher operating frequencies, (the recommended rule of 10× the operating frequency is suggested for microwave systems that the package was originally designed for). At THz frequencies a cut-off of just 3× the operating frequency was found to be sufficient within the longer taper. Any further increases in cut-off significantly increased the

computation time while still producing convergent results. The fundamental TE_{10} mode is the dominant mode. The S-parameters of the fundamental mode over this range are shown in figure 4.7. The S_{21} shows there is high transmission through the horn (~ -0.3 dB), the S_{11} shows the reflected power at the throat of the horn, for the TE_{10} mode this is ~ -47 dB at the mid-point frequency and there is ~ -26 dB reflected power at the aperture of the antenna (S_{22}) at this mid-point.

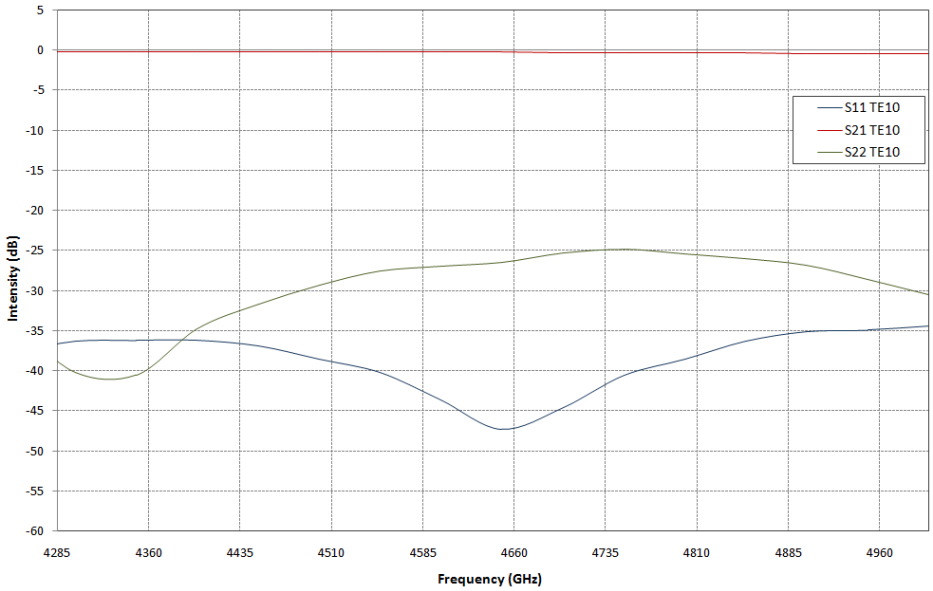

Figure 4.7 ***S-parameters for the fundamental TE_{10} mode of the SAFARI horn over the 4.285 - 5.0THz band.***

At the lower end of the frequency band, 4.285 THz, four modes propagate within the throat of the horn. Power has the potential to be scattered between each propagating mode at the throat of the horn before reaching the detector. The four propagating modes and the following six attenuated modes at a frequency of 4.285 THz are listed in table 4.1. As the operating frequency increases higher order modes will "switch on" (begin to propagate within the throat of the horn). For example, at a frequency of 6 THz the TE_{20} and TE_{02} modes are no longer below the cut-off frequency and so will propagate at the horn throat.

	Mode	Cut-off (GHz)	Attenuates at (dB)
1	TE_{10}	2997.92	0.00
2	TE_{01}	2997.92	0.00
3	TE_{11}	4239.71	0.00
4	TM_{11}	4239.71	0.00
5	TE_{20}	5995.85	-381.74
6	TE_{02}	5995.85	-381.74
7	TE_{21}	6703.56	-469.24
8	TE_{12}	6703.56	-469.24
9	TM_{21}	6703.56	-469.24
10	TM_{12}	6703.56	-469.24

Table 4.1 ***First ten modes, propagating and attenuated, at the throat of the SAFARI horn at an operating frequency of 4.285 THz***

As can be seen from table 4.1 some modes have the same cut-off frequencies, these modes are said to be degenerate. At higher frequencies with more modes propagating there is higher potential for power scattering between modes at the throat of the horn. At the highest operating frequency of 8.57 THz the twelve propagating and the next three attenuated modes at the throat of the horn are shown in table 4.2.

	Mode	Cut-off (GHz)	Attenuates at (dB)				
1	TE_{10}	2997.92	0.00				
2	TE_{01}	2997.92	0.00				
3	TE_{11}	4239.71	0.00				
4	TM_{11}	4239.71	0.00				
5	TE_{20}	5995.85	0.00				
6	TE_{02}	5995.85	0.00		11	TE_{22}	8479.41	0.00
7	TE_{21}	6703.56	0.00		12	TM_{22}	8479.41	0.00
8	TE_{12}	6703.56	0.00		13	TE_{30}	8993.77	-248.04
9	TM_{21}	6703.56	0.00		14	TE_{03}	8993.77	-248.04
10	TM_{12}	6703.56	0.00		15	TE_{31}	9480.27	-368.76

Table 4.2 ***First fifteen propagating and attenuated modes at the throat of the SAFARI horn at an operating frequency of 8.57 THz***

The return loss (S_{11}) of each mode at the throat of the horn over the 4.285 - 5.285 THz range is shown in figure 4.8. The TE_{10} (red line) and TE_{01} (blue dotted line) are degenerate modes and have the same levels of return loss at the horn throat.

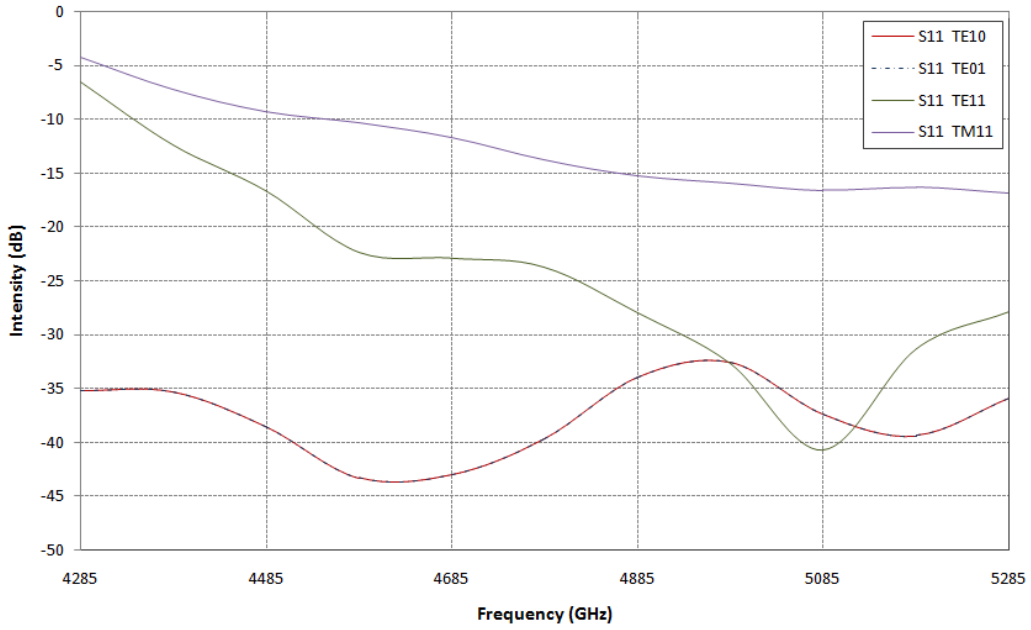

Figure 4.8 ***S_{11} return loss at the horn throat for each propagating mode at 4.285 - 5.285 THz***

The return loss of power scattered between modes at the horn throat is shown in figure 4.9. These have much lower power levels ($< -290\ dB$) compared to the mode scattering to itself as would be expected.

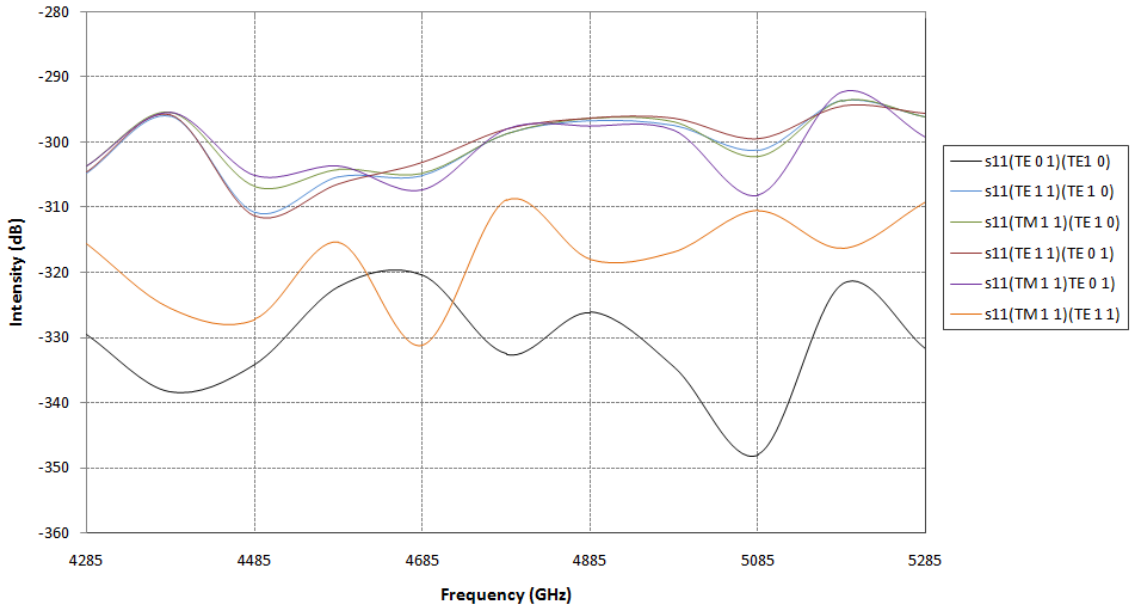

Figure 4.9 ***S_{11} return loss at the throat of the horn for power scattered between modes***

4.4.2 SAFARI horn far-field

The high side lobe levels in the E-plane and the asymmetry between the E- and H-plane fields demonstrated in the preceding sections for single moded pyramidal horns makes them an uncommon choice for high performance quasi-optical systems such as SPICA, these problems are overcame by use of multi-moded horns. As the SAFARI horns are placed in an array shaping of the beam pattern is required for optimum performance of the array.

The aperture field distribution caused by the dominant mode field, given by,

$$E_y = E_0 \cos\frac{\pi x}{a} \qquad E_x = 0 \tag{4.6}$$

can be modified by the addition of higher order modes to produce the desired radiation pattern characteristics. The addition of TE_{1m} and TM_{1m} modes will modify the E-plane distribution as these modes have the form (from section 2.3)

$$E_y = A_m sin\frac{\pi x}{a} cos\frac{my\pi}{b} \tag{4.7}$$

this causes no change to the H-plane distribution. Only even values of *m* have symmetric field distributions that will produce symmetric patterns . TE_{12} and TM_{12} modes each have a non zero E_x field however they may be excited as a pair such that the total E_x is zero. The total distribution may then be written as [Rudge 1982],

$$E_y = sin\frac{\pi x}{a}(1 + Acos\frac{2\pi y}{b}) \tag{4.8}$$

where *A* is chosen appropriately for a given purpose such as the cancellation of E-plane side lobes, this would require A to be real such that two modes must be in phase in the aperture.

This principle is invoked in the SAFARI horns where the addition higher order modes modifies and broadens the far-field pattern. In a multi-moded horn the modes propagate independently and are therefore incoherent relative to one another, to produce a composite far-field pattern the modes must be added in quadrature and the total field is an incoherent summation. The separate H-plane far-fields of each propagating mode at 4.835 THz are shown in figure 4.10, it can be seen that the TE_{10} far-field has a form similar to the far-field of a single moded pyramidal horn produced

in the preceding sections with a tapered H-plane distribution (phi = 0.0 deg). It can also be seen that as was mentioned above the TE_{11} and TM_{11} far-fields contribute very little to the H-plane distribution, this is also true of the TE_{01} field.

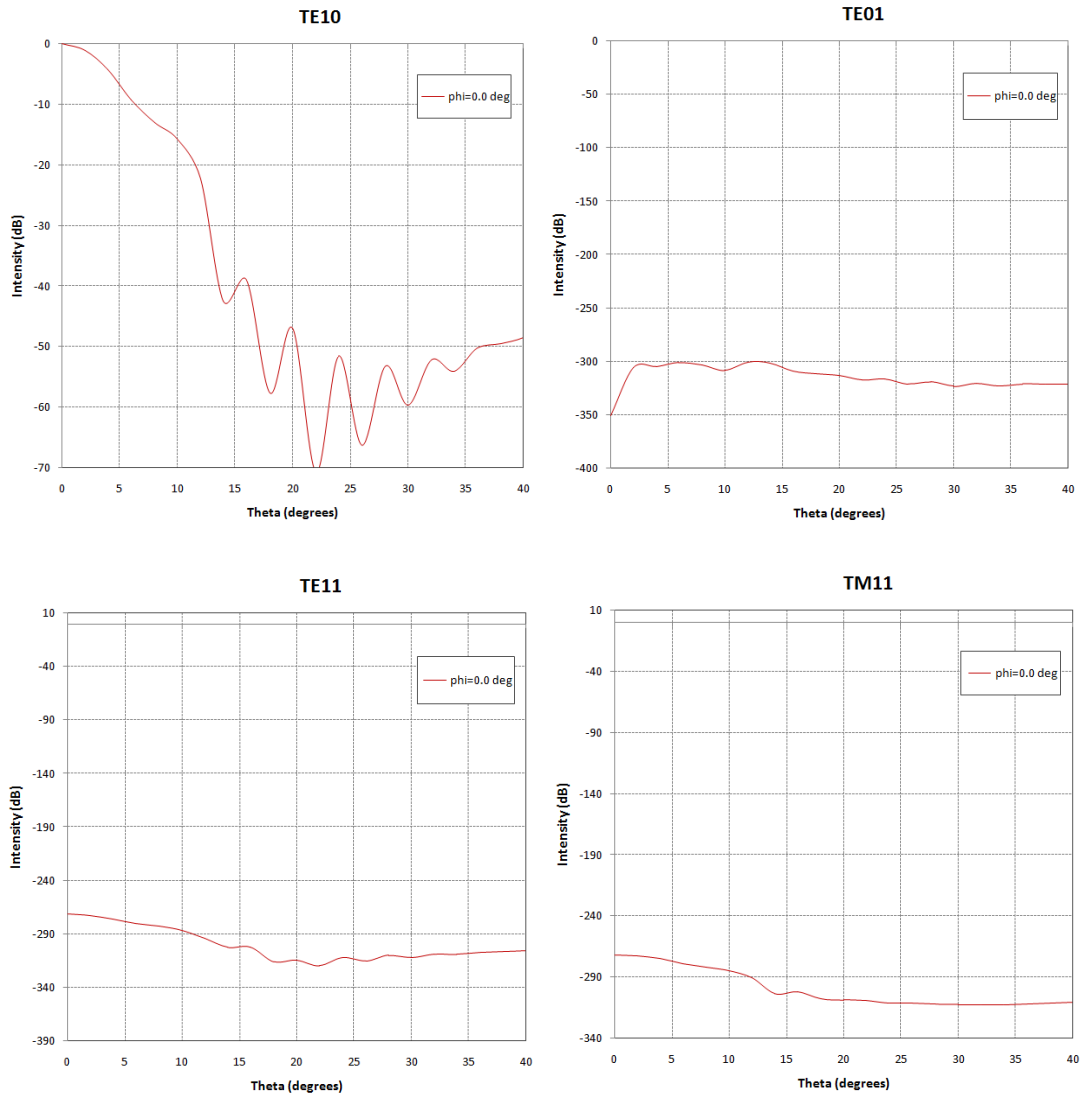

Figure 4.10 ***H-plane cut of the far-field of each propagating mode at the throat of the SAFARI horn at 4.835 THz***

The total far-field of the horn contains contributions from all modes that propagate within the throat of the horn. With the far-field calculated for each mode separately, the contributions are then summed together in quadrature to give the total far-field of the horn. The total H-plane far-field at 4.835 THz is shown in figure 4.11. This is the sum of the TE_{10}, TE_{01}, TE_{11} and TM_{11} mode far-fields shown in figure 4.10. In an astronomical receiver such as SAFARI even though the main mode couples maximally to the beam coming from an astronomical source on the sky the other modes that

propagate also couple additional power to the bolometer detectors increasing the sensitivity of the instrument. Generally the more modes that can propagate the more power that can couple to the detectors until the geometrical approximation is reached and an infinite number of modes. Practically much better signal can be achieved with tens to hundreds of modes, following this reasoning as SAFARI is intended to observe very weak signals the more multi-moded the horn becomes the higher the gains in sensitivity.

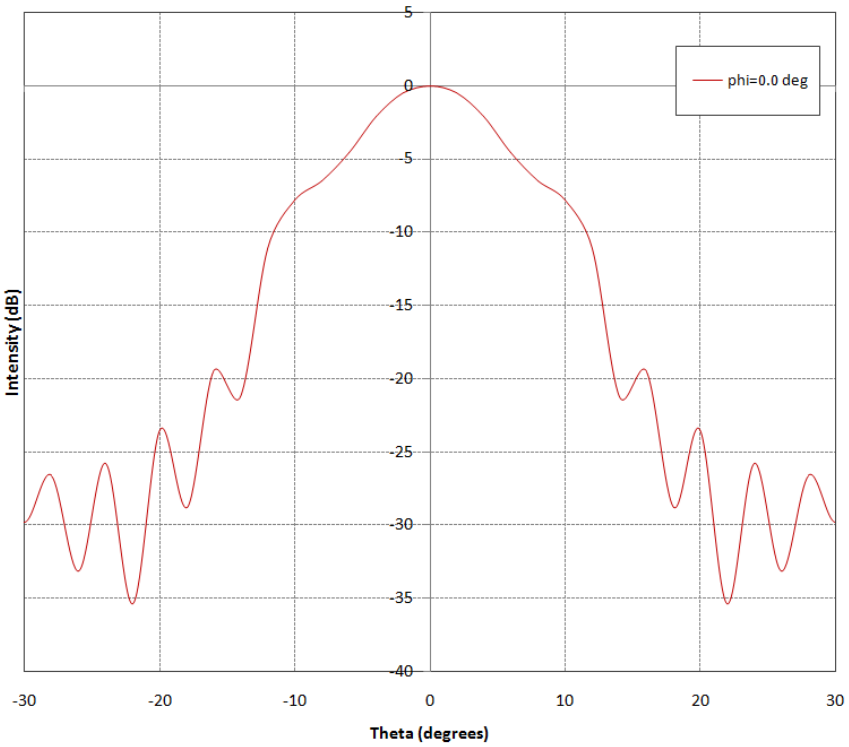

Figure 4.11 ***Total H-plane far-field radiation pattern of the SAFARI S-band horn at 4.835 THz***

Once suitable models of an isolated SAFARI horn were produced the horn was modelled as part of an array, this is discussed in more detail in section 5.5.

4.5 Conclusion

Following on from the analysis of chapter 3, this chapter applies GBMA and mode matching techniques to the analysis of pyramidal horn antenna. Firstly the techniques were applied to the calculation of far-field patterns of single moded pyramidal horns and comparisons were made between each package. While the analysis of pyramidal

structures is known to be complicated (compared to conical analysis) due to the boundary conditions imposed, it was concluded that while producing accurate results of the far-field the computation of high frequency, electrically large pyramidal structures within Microwave Wizard is computationally exhaustive leading to memory constraints and extremely long computation times. While SCATTER code developed for rectangular waveguide structures also utilises the mode matching technique it has quicker computation times while still producing accurate far-field predictions. A Hermite Gaussian mode set was used within the GBMA to predict far-field patterns of the same pyramidal horn with reasonable accuracy and quick computation times. The SAFARI S-band horn, a multi-moded square aperture pyramidal horn, was analysed using the mode matching technique of Microwave Wizard operating at terahertz frequencies. While it was noted earlier that SCATTER is perhaps more suited to the analysis of pyramidal horns due to shorter computation times, as the eventual goal is to measure the crosstalk between two SAFARI horns these kind of off-axis transmission properties of a system are not producible within SCATTER, thus μWW was used for the analysis. Multi-moded scattering parameters of the horn were produced and the multi-moded far-field was calculated as a summation of each propagating modes far-field added in quadrature. The advantages of multi-moded horns especially there use in astronomical receiver systems due to the higher signals received and shaped beam patterns was discussed and illustrated.

CHAPTER 5

Crosstalk Analysis

5.1 Introduction

In the previous chapters the beam characteristics of single horn antenna operating in isolation with no outside influences have been discussed. However in many terahertz or sub-millimetre systems such as the SPICA instrument (section 5.5) the antennas are arranged in to an array to improve resolution and the overall sensitivity of the instrument. Many pixels operating together in the focal plane of a single telescope and receiving system offer better sensitivity where each antenna in the array couples to a single pixel. This increased sensitivity is required for the next generation telescopes which are targeting astronomical sources and receiving very faint signals. Recent astronomy projects propose array sizes with hundreds or thousands of pixels as realistic goals for sub-millimetre wave receivers. The presence of a second antenna (or any number more neighbouring a single antenna) also causes a potential interaction between each antenna potentially leading to leakage of power or signal and noise. The proximity of the second antenna affects the current distribution on both antennae and due to this, the input impedance could potentially be altered as well as the radiation pattern. This interaction called mutual coupling or crosstalk is the subject of the analysis carried out in this chapter. Mutual coupling can be created in a number of different ways, direct space coupling between elements in the array, indirect coupling caused by scattering from nearby objects or optical components in the receiver and also the feed network that connects the array elements provides another path for coupling [Stutzman and Thiele 2012] although this can be minimized by proper impedance matching at each element. Indirect coupling can also be minimized by isolating the array from stray light reflections or standing waves from the optical system in front of the array. In sub-millimetre/terahertz instruments this is often done by coating reflective surfaces with stycast or anti-reflecting material to minimise

reflections onto the array. It is the first type direct coupling that will be discussed in the following sections.

5.1.1 Description of direct mutual coupling

As an initial example of how one can analyse mutual coupling or crosstalk consider two horn antennas as in figure 5.1, with antenna one transmitting (a) while antenna two is inactive (passive). When power from the first horn radiates it will be transmitted in to free space (c) although some power will also be scattered/propagate in the direction of antenna two (d) this power will in turn will be radiated in free space (e) some radiation can potentially 'leak' into the second horn and manifest itself as crosstalk with its neighbouring horn (f). That is power arriving at the throat (where a detector may be present) of the second antenna after being transmitted from the first antenna. For each antenna also considered in isolation there is a return loss (b) or reflected power (S_{11} component in S parameter description) within the antenna itself which does not radiate into free space and is always present internally within the horn.

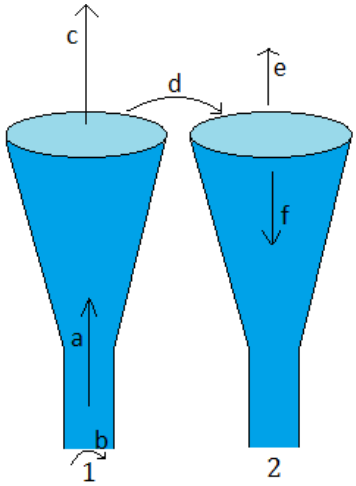

Figure 5.1 Direct coupling between two antenna in an array

If the second antenna is also transmitting the same will be true for antenna two leaking to antenna one and so on for all elements in the array, with the closest neighbours having the largest crosstalk component while further away neighbours could also suffer a lower level of power leakage. It can be seen from this example that in an array of antenna there may be high levels of crosstalk with each element

registering excess signal at a detector placed at the throat of the horn. We wish to quantify this excess power caused by mutual coupling so that it can be minimised or at least understood during the design process and/or accounted for at a later stage during calibration for example. In terms of scattering parameters the S_{21} component is the amount of power that arrives at port 2 (e) due to this transmitted signal from port 1 (a) which is of interest here, this is the crosstalk between the two horns. This power is then considered to be an identical level for the horns if the radiating and passive horns are reversed.

5.1.2 Mutual coupling using circuit concepts

A single isolated horn antenna has an input impedance, when part of an array there is both an input (or self) impedance and also a mutual impedance caused by the presence of one or more antenna. If the array is considered in terms of circuit concepts where an array of *N* horn antenna elements is considered an *N* port network and each antenna is considered a current source the self impedance of the *n*th element is given by [Huang and Boyle 2008]

$$Z_{nn} = \frac{V_n}{I_n}, n = 1, 2, 3, \dots N \tag{5.1}$$

if all other elements are open circuited where I_n is the current at the *n*th element and V_n is the voltage generated at the *n*th element. This is the same as the input impedance of a single isolated antenna element (not part of an array). The mutual impedance between two elements *m* and *n* in the array is given by equation 5.2. By reciprocity $Z_{mn} = Z_{nm}$

$$Z_{mn} = \frac{V_m}{I_n} \tag{5.2}$$

The voltage generated at each element is

$$\begin{aligned} V_1 &= Z_{11}I_1 + Z_{12}I_2 + \dots + Z_{1N}I_N \\ V_2 &= Z_{21}I_1 + Z_{22}I_2 + \dots + Z_{2N}I_N \\ &\vdots \\ V_N &= Z_{N1}I_1 + Z_{N2}I_2 + \dots + Z_{NN}I_N \end{aligned} \tag{5.3}$$

Taking mutual coupling into account the input impedance of the *n*th element in the array is

$$Z_n = \frac{V_n}{I_n} = Z_{11}\frac{I_1}{I_n} + Z_{12}\frac{I_2}{I_n} + \cdots + Z_{1N}\frac{I_N}{I_n} \tag{5.4}$$

The extent of mutual coupling between elements depends on the physical separation between them, their orientation relative to each other (which is often parallel but the array may also be oriented over a curved focal plane) and the radiation characteristics of each element (i.e. how directional the beam is which is associated with the horn geometry and design). For identical array elements with uniform amplitude excitation the effects of increasing separation and changing the element orientation is examined here for the simple case of rectangular and circular waveguides. This is one of the most extreme examples of crosstalk as the field emerging from the waveguide is not directional (can be approximated as something like a point source) and radiates significant levels of energy in the half hemisphere in front of the waveguide, the energy propagates laterally potentially interacting with the neighbouring element.

5.2 Crosstalk between rectangular waveguides in an array

Standard WR-10 waveguides with dimensions 2.54 mm by 1.27 mm and length 10 mm operating at 100 GHz were modelled using CST MWS (section 2.5.4). The TE_{10} mode (fundamental mode) is the only propagating mode within the waveguide at this frequency shown in figure 5.2. The electric field within tapers to zero at the boundary in the H-plane. There is no drop of in intensity however in the E-plane and the field falls sharply to zero at the boundary. The far field of a single isolated rectangular waveguide predicted by CST in the E and H plane and the 3D radiation pattern are shown in figure 5.3.

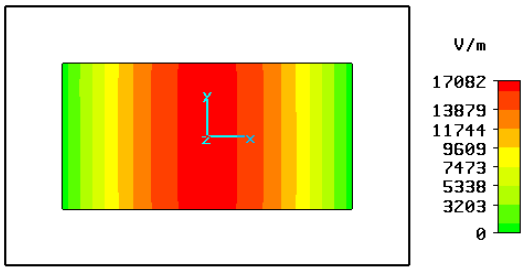

Figure 5.2 *TE_{10} field distribution at WR-10 waveguide opening*

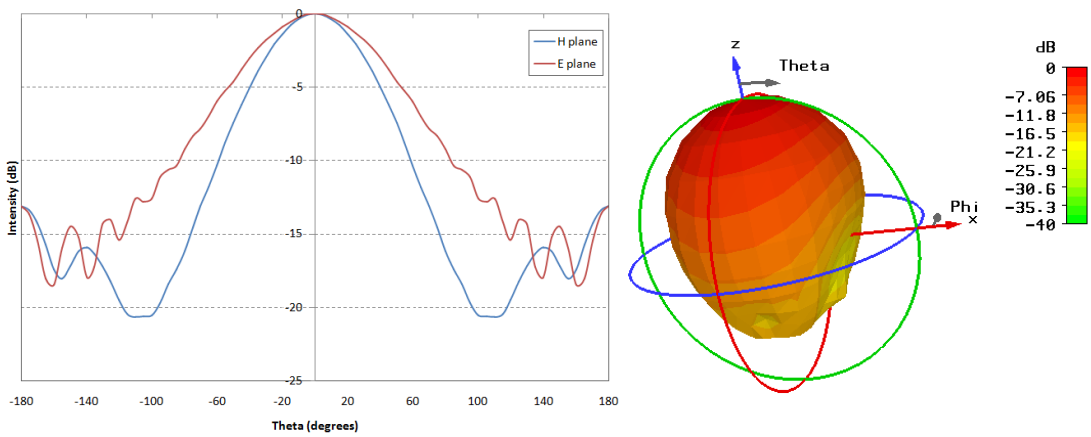

Figure 5.3 *(Left) Far field of a single isolated WR-10 waveguide showing low directionality of the waveguide, (Right) 3D representation of the far field*

The orientation (horizontal or vertical) of rectangular waveguides (or similarly single moded pyramidal horns) in an array can have significant effects on the crosstalk due to this tapered field distribution. Two horizontally arranged WR-10 waveguides modelled in CST are shown in figure 5.4a, the waveguide walls are of thickness 0.5 mm and the waveguide openings are separated by a distance of 1 mm. This means the waveguides

are in electrical contact with each other as would be the case in many practical arrays. The model assumes the waveguides are made from a perfect electrical conductor and they are surrounded by a vacuum. Each waveguide has its own port providing the excitation signal. The S_{21} and S_{11} parameters for this configuration are shown in figure 5.4b, due to the symmetry of the system the S_{21} is the same as S_{12} parameter. Similarly $S_{11} = S_{22}$.

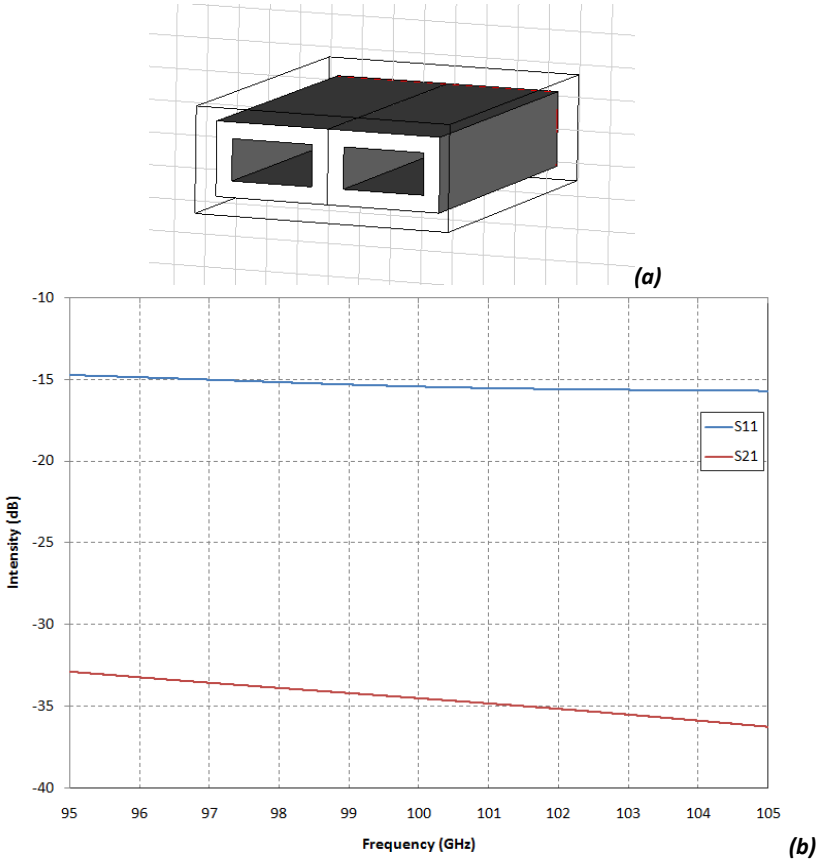

Figure 5.4 ***(a) WR-10 waveguides in a horizontal configuration modelled in CST (b) S parameters of the waveguides shown in (a)***

When the gap between waveguide openings is λ/3 the S_{21} is -34.5 dB at 100 GHz this is about 0.0015% of the power that was launched through the first waveguide at port one has been scattered and transmitted through waveguide two to be received as a signal at port two. With the waveguides arranged vertically so the coupling is in the direction that the E field does not taper to zero in there is quite a significant effect on the S_{21} parameter as shown in figure 5.5. While the S_{11} remains the same the S_{21} is now -19.5 dB this is higher than with the waveguides in a horizontal configuration, at 0.01% of the original power.

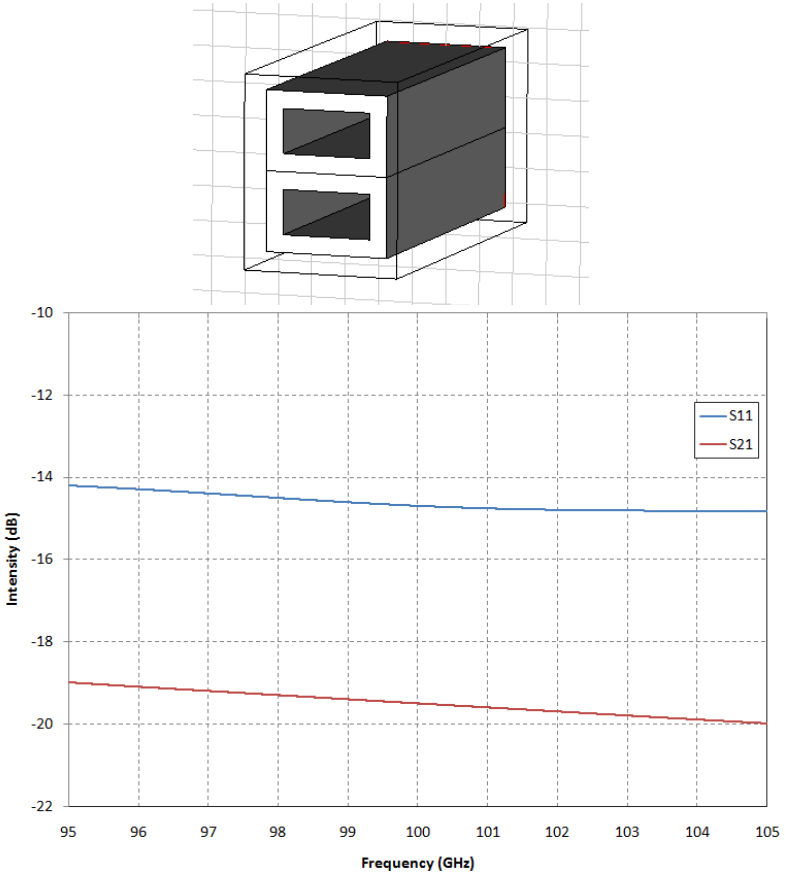

Figure 5.5 ***(a) WR-10 waveguides in a vertical configuration modelled in CST (b) S parameters of the waveguides shown in (a)***

As single moded pyramidal horn antenna have similar tapered field distributions at the horn aperture comparable trends in the crosstalk would be expected between two pyramidal horns although the crosstalk is expected to be lower due to the horns higher directivity. This illustrates how the orientation of elements in an array affects the mutual coupling in the single moded case between rectangular/pyramidal elements. The effects of increasing the physical separation between the waveguides is now analysed. The gap between the waveguides for both configurations was increased to 4 mm so it is now larger than the wavelength of received radiation. The results are shown in figure 5.6. For the horizontal configuration the S_{21} decreases from -34.5 dB to -50.3 dB with this increase in distance. In the vertical configuration it decreases from -19.5 dB to -28.6 dB.

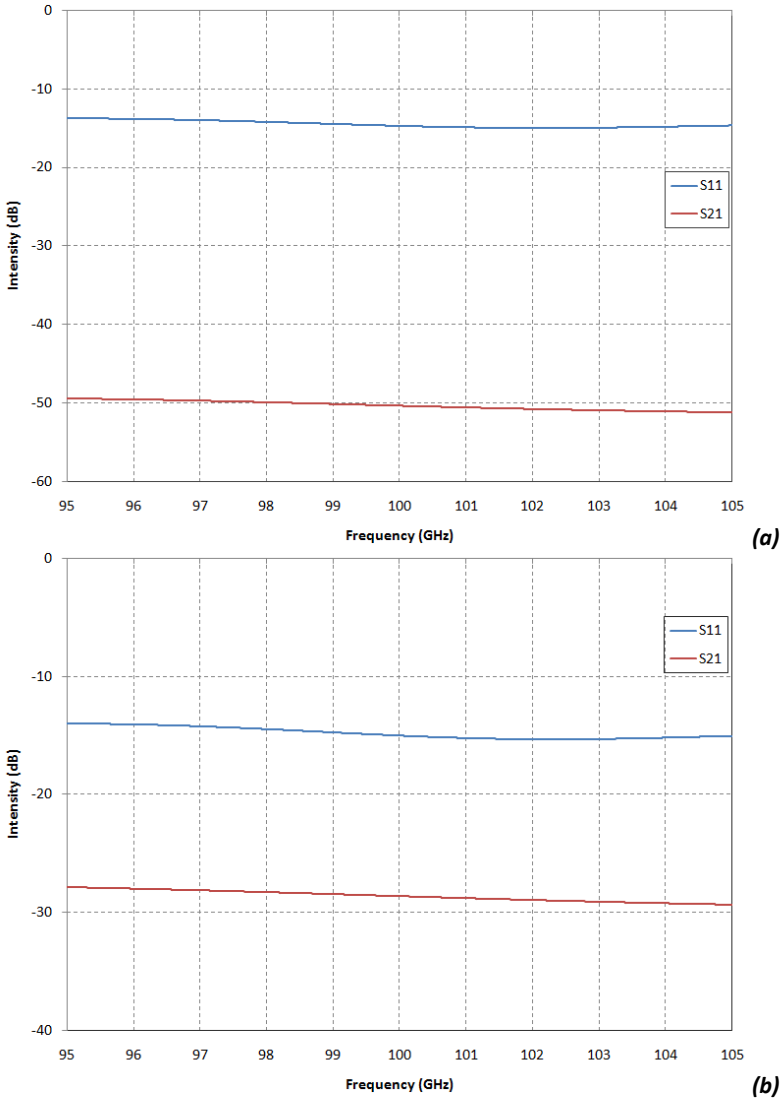

Figure 5.6 ***S_{21} (red line) of WR-10 waveguides in a horizontal configuration (a) and vertical (b) with a 4 mm gap between waveguides***

Increasing the distance between elements in the array decreases the crosstalk between them although this increased distance may also lead to unwanted beam characteristics. For the required sensitivity, distance between elements should be minimized to receive as much of the beam through the telescope as possible potentially from very weak astronomical sources. There may also be restrictions on the array size to fit into compact instruments. Focal plane sizes are also limited due to aberrations associated with the telescope being limited the further off axis the pixel in the array is from the central pixel. For example in the CoRE mission, a proposed CMB polarisation instrument, for a channel centred at 100GHz, the focal plane size is limited to a circle of 350mm diameter [www.core-mission.org].

5.3 Crosstalk between circular waveguides in an array

An equivalent analysis was performed on circular waveguides being part of an array. The waveguides inner radius is 1 mm, the circular wall has a thickness of 0.5 mm and an overall length of 10 mm (to dissipate evanescent modes) again operating at 100 GHz. The model assumes the guides are made from a perfect electrical conductor metal surrounded by a vacuum. Each waveguide has its own port in the analysis and one mode (the fundamental TE_{11} mode) was launched through the waveguide length. The field at the waveguide opening is shown in figure 5.7. In the H-plane the field tapers to zero at the boundary. There is less tapering in the E-plane and an abrupt drop to zero at the boundary wall.

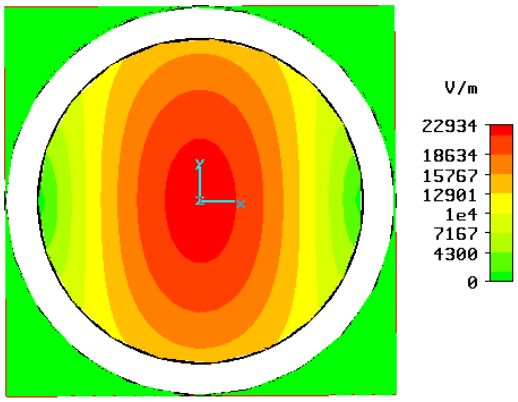

Figure 5.7 ***TE_{11} field distribution at the opening of a smooth walled circular waveguide***

With the waveguides in a horizontal configuration and a 1 mm gap between the apertures as shown in figure 5.8a the S_{21} was calculated, figure 5.8b. The orientation of the waveguides was changed to a vertical configuration, again with a 1mm gap (i.e. in electrical contact). The crosstalk results for this orientation can be seen in figure 5.9b. As before with the rectangular waveguide array there is an increase in crosstalk although it is not as dramatic as the rectangular waveguide results this is because the field does taper slightly in the E plane for the circular waveguides.

(a)

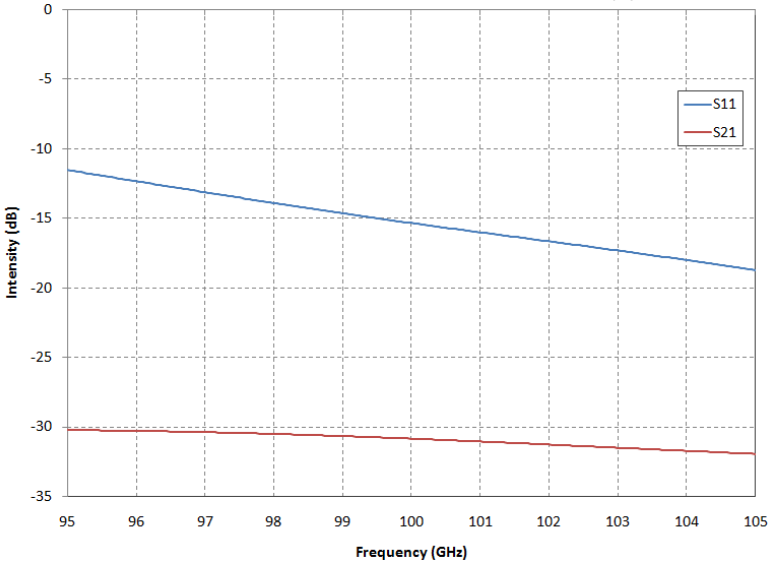

(b)

Figure 5.8 *(a) Horizontal configuration to measure crosstalk between circular waveguides with 1 mm gap (b) S_{11} (blue) and S_{21} (red) of waveguides shown in (a) above*

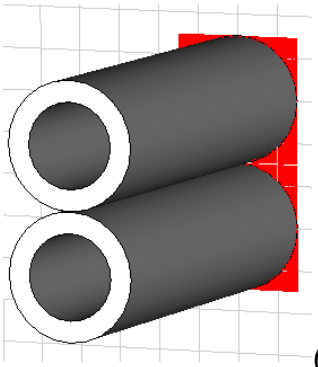

(a)

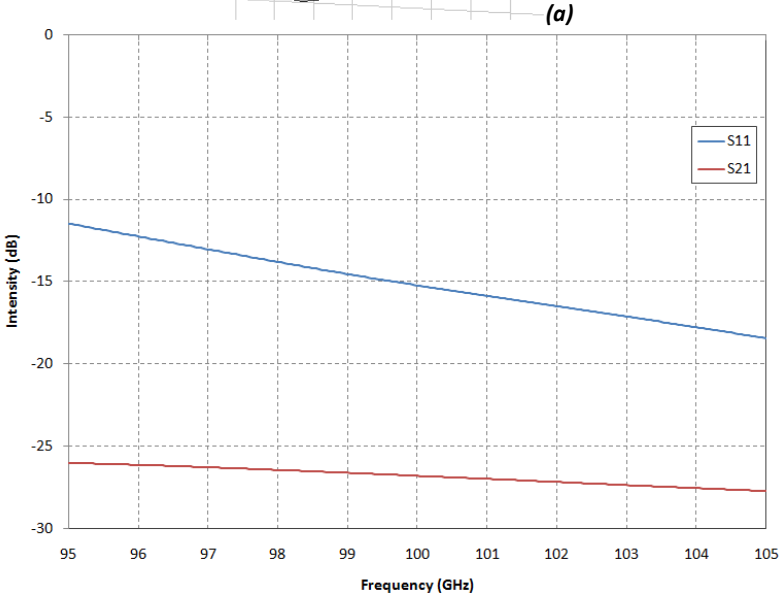

(b)

Figure 5.9 *(a) Vertical configuration to measure crosstalk between circular waveguides with 1 mm gap (b) S_{11} (blue) and S_{21} (red) of waveguides shown in (a)*

The separation between waveguides was then increased so it was comparable to the radiation wavelength to investigate the effects this had on the crosstalk. The results for both configurations are shown in figure 5.10 with a gap of 4 mm. As expected the crosstalk decreases although this increased distance may lead to other unwanted complications as before. As mentioned in section 3.2 the aperture field of a single moded smooth walled conical horn is essentially the TE_{11} mode with a spherical wave front due to the flare of the horn and the field distribution has a similar tapered field. Thus the orientation of conical horns in an array will have similar trends in the crosstalk between elements. As corrugated conical horns produce nearly symmetric beam patterns (section 3.1.2), orientation will have little or no effect although due to the geometries conical horns do not pack as tightly together in an array as pyramidal horns (i.e. the packing density is geometrically lower).

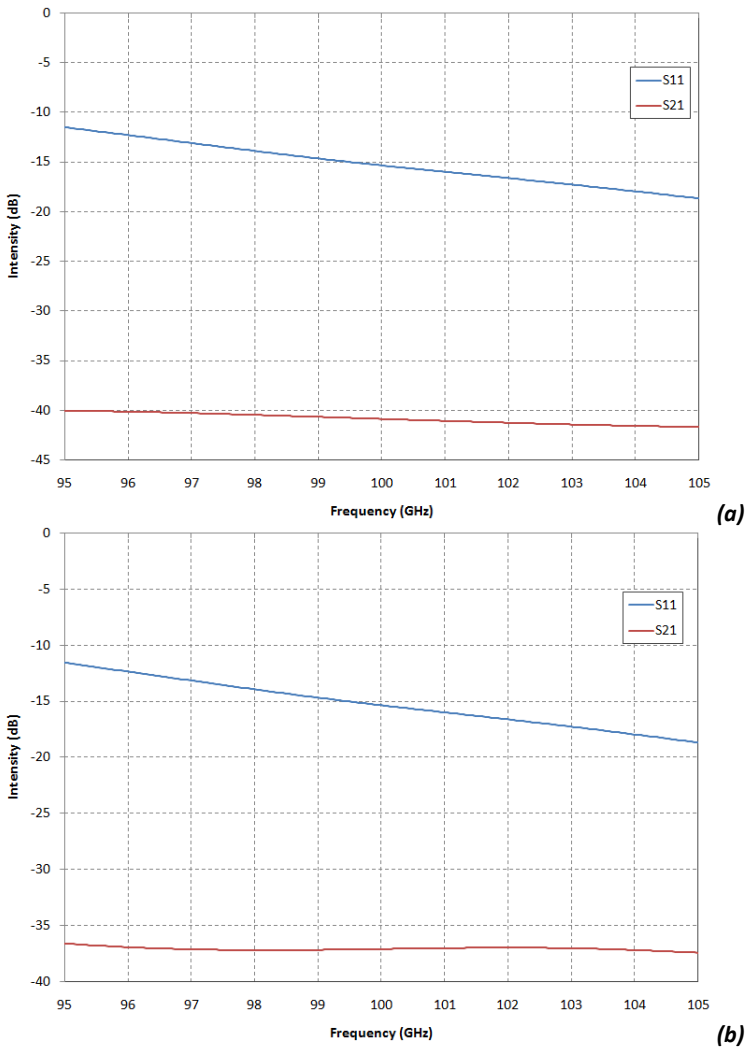

Figure 5.10 ***(a) S parameters of circular waveguides in horizontal configuration with a gap of 4 mm***
(b) S parameters of circular waveguides in vertical configuration with a gap of 4 mm

5.4 VNA crosstalk measurements

5.4.1 Waveguide crosstalk

A vector network analyser (VNA) which is capable of measuring both phase and amplitude was used to measure crosstalk between two WR-10 waveguides in a horizontal configuration, as the separation distance between waveguides was increased, with both waveguides transmitting and receiving power. The results were compared against CST and μWW models. Due to the flange around the waveguide opening it was not possible to have the waveguides closer than 16.5 mm apart. Operating over the 75 GHz to 110 GHz band this is ≈ 5.5 times the mid wavelength, thus measurements where the separation distance was comparable to the received radiation wavelength, as in sections 5.2 and 5.3, were not possible. With the waveguide apertures the minimum distance apart (16.5 mm) in the same plane, the flange around each of the waveguides are in electrical contact. With head one of the VNA providing an excitation signal at waveguide one and head two exciting waveguide two the S_{21} parameter measured by the VNA is the signal received at port 2 due to the signal transmitted at port one, this is the crosstalk between the waveguides. The S_{11} parameter is also measured, this is simply the reflected power received at port one due to the signal from port one and similarly the S_{22} is also measured. The separation distance was increased to 23.5 mm, S_{11} and S_{21} measurements were again taken. The S parameters for each distance can be seen in figures 5.11 and 5.12, the measured results are compared against CST models of the same setups. It can be seen from the figures that the levels of crosstalk power in the measured and modelled results are in good agreement. Standing wave effects can be seen in the measured results (solid line) unlike in the modelled results (dotted line). This can be explained by the fact that the model assumes the waveguides to be perfect electrical conductors surrounded by a vacuum, this is not the case in the measured results, although reflections are minimised using absorbing material surrounding the experimental set up they cannot be cancelled out completely and this leads to the effects observed in the measurements. Also the influence of currents flowing over the flange surface is not modelled accurately. Standing waves are discussed in more detail in chapter 6.

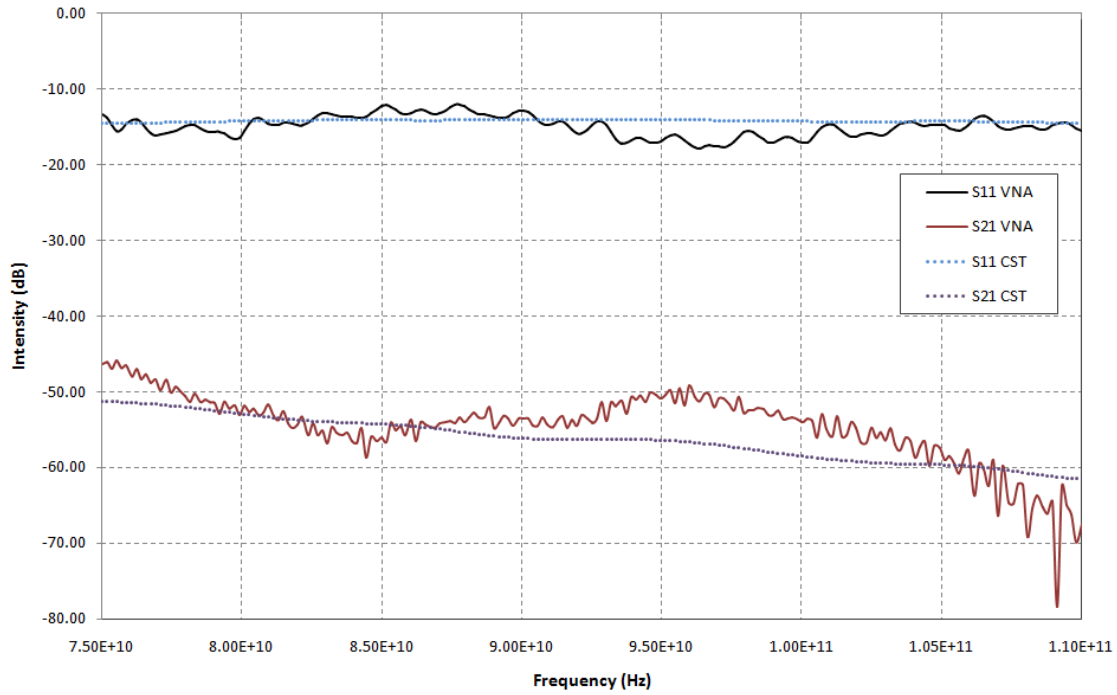

Figure 5.11 ***S parameters of two WR-10 waveguides separated by a distance of 16.5 mm, experimental results (solid line) compared against CST model (dotted line)***

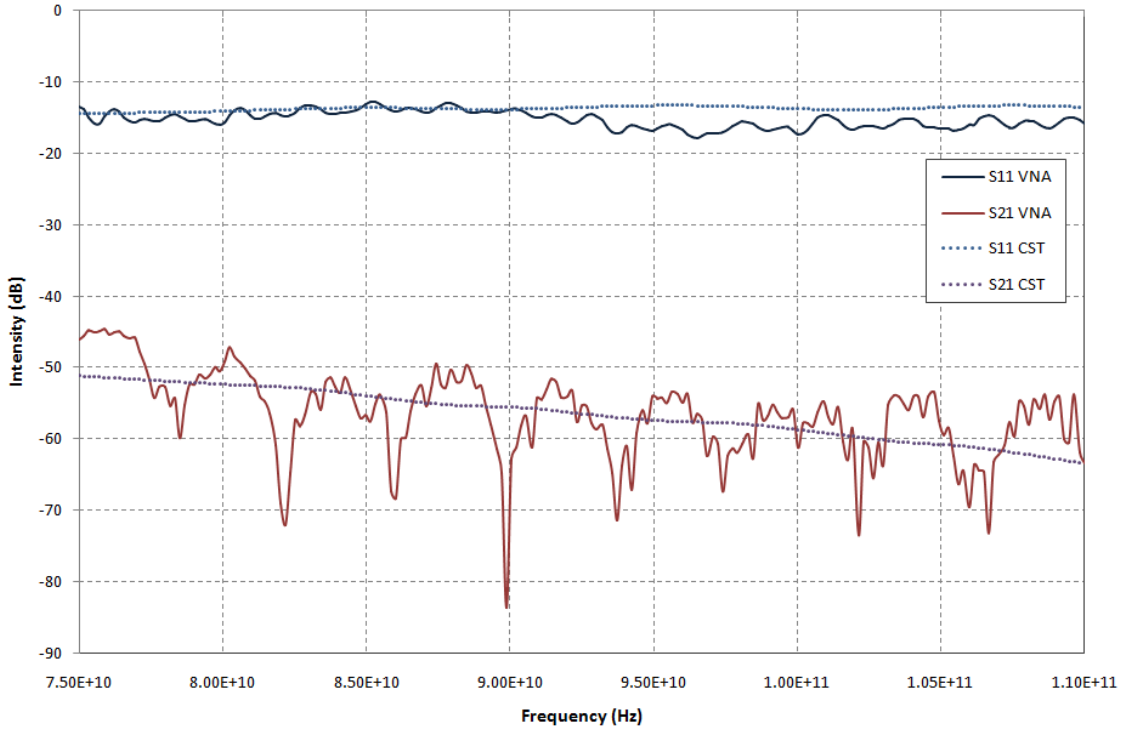

Figure 5.12 ***S parameters of two WR-10 waveguides with the separation distance between apertures increased to 23.5 mm***

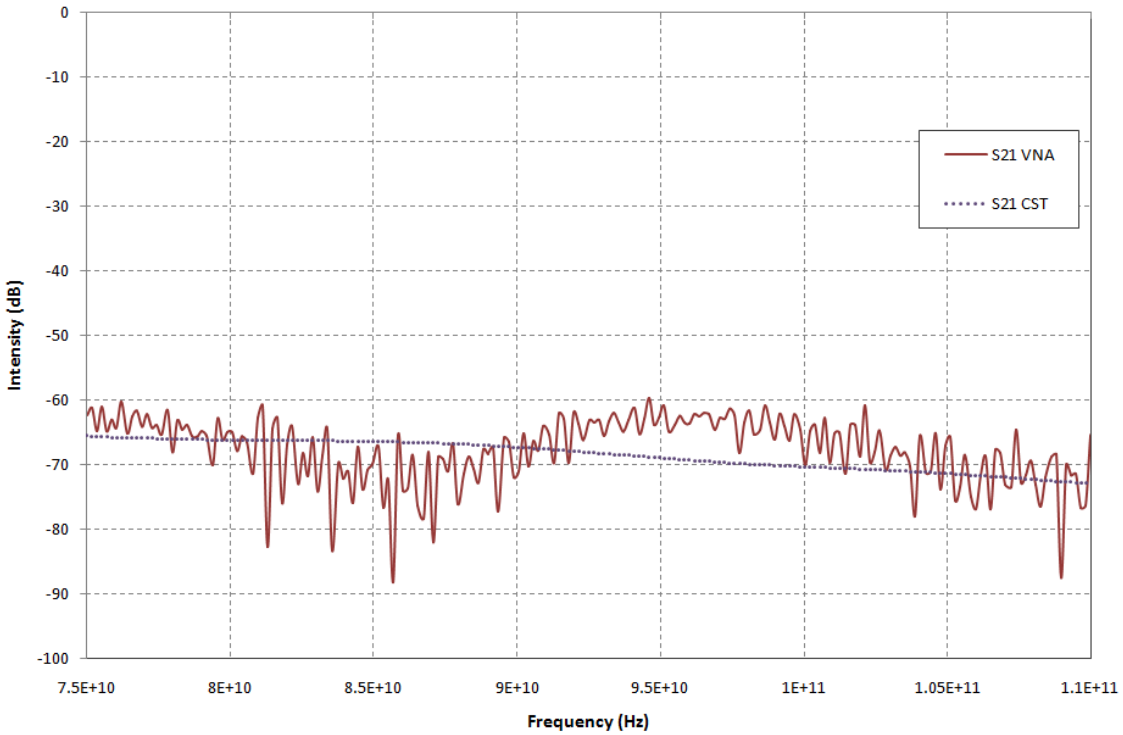

Figure 5.13 ***Crosstalk between two WR-10 waveguides with a separation distance between apertures of 60 mm***

The distance between waveguides was then increased further to 60 mm, 98 mm and 160 mm. Measurements of the S_{11} and S_{21} parameters were taken with each increase in distance. At 60 mm there is still good agreement between the levels of measured and modelled (figure 5.13) but beyond this the experimentally measured results began to level off with these further increases as the extremely low levels of crosstalk power became undistinguishable from noise caused by the surroundings ($\approx$ -70 dB), while the modelled results predict further decreases in the crosstalk between waveguides due to the idealised nature of the model (the measurements are limited to the dynamic range of the VNA itself). These results can be seen in figures 5.14a (VNA measurements) and 5.14b (CST model).

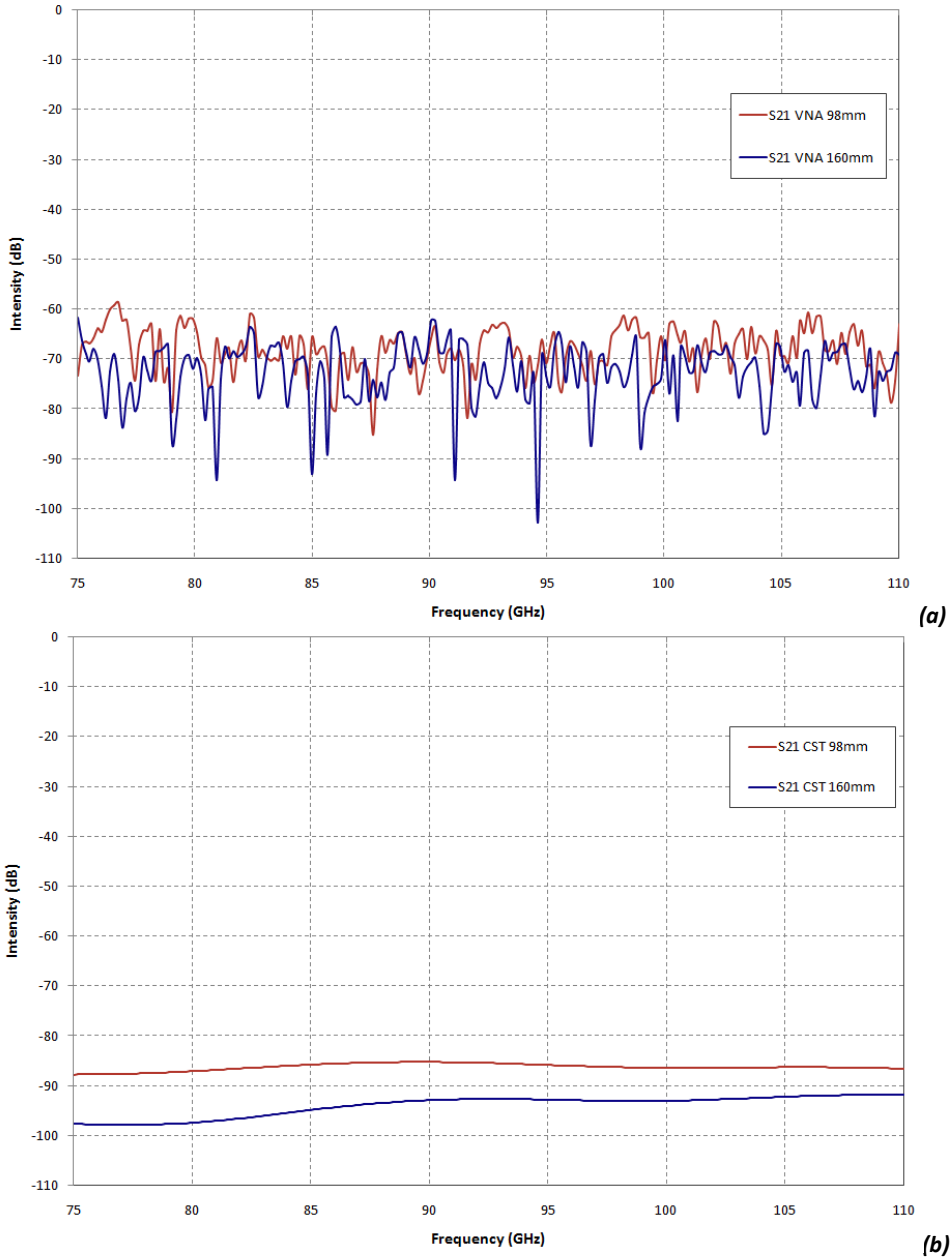

Figure 5.14 ***(a) Experimentally measured crosstalk between two WR-10 waveguides for large distances where crosstalk becomes indistinguishable from noise***
(b) CST model crosstalk between two WR-10 waveguides for large distances

Models of the waveguides at a distance of 23.5 mm apart were also produced within µWW to investigate the crosstalk between them. The µWW model was limited in that for radiation from to apertures within µWW the waveguides must be joined by use of a slot array element from the µWW library as only one radiation element can be used in the analysis, thus the free space between the waveguides is not accurately reproduced in the model. The µWW model compared against VNA measurements can be seen in figure 5.15. While good agreement is seen between the S_{11} reflected power at the waveguide, the µWW model S_{21} parameter is noticeably ~ 5 dB higher suggesting the

slot array element is causing unwanted reflections at the surface. In many practical arrays such as the SAFARI array (section 5.5) the array elements are in electrical contact at the array entrance and as such the slot array element used to simulate the entire array radiating to free space is of use in these types of array, however here it is unwanted and causes inaccuracies in the model.

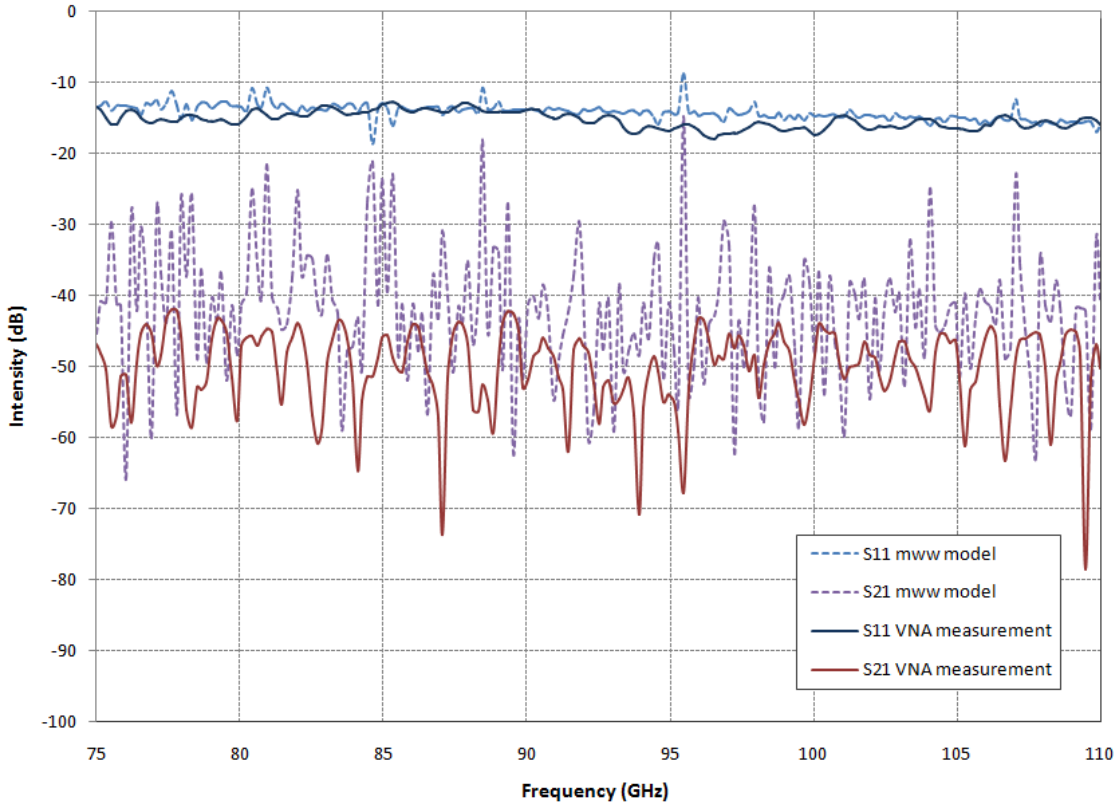

Figure 5.15 ***S_{11} and S_{21} measured versus µWW modelled results for two waveguides 23.5 mm apart.***

5.4.2 Horn antenna crosstalk

The crosstalk between two identical W-band pyramidal horn antennas was also investigated using a Vector Network Analyser. The horns are designed to receive radiation over the frequency band 75 GHz to 110 GHz, with dimensions aperture width 27 mm, aperture height 20 mm and slant length 63.5 mm fed by a standard WR-10 waveguide of length 11.2 mm. Port one feeds the waveguide of horn one and port two feeds the waveguide of horn two. With the horns parallel and the apertures in the same plane the horns were placed side by side touching and orientated horizontally as the S_{21} parameter was measured from 75 to 110 GHz, due to the thickness of the walls of the horn there is a separation of 3 mm between the horn apertures. In the

horizontal configuration very low crosstalk power levels are measured (~ -70 dB) even at this minimum distance, with the separation distance increased to 3 cm, 6 cm and 9 cm there is little change in the measured crosstalk. Due to the high directionality of the horns beam pattern the low levels of crosstalk are indistinguishable from noise caused by the surroundings even at small distances. The orientation of the horns was then changed to a vertical configuration again with the horns touching. The S_{21} or crosstalk between the two horns for each orientation with a 3 mm distance between apertures can be seen in figure 5.16. With the waveguides in the vertical configuration crosstalk levels are noticeably higher and are now distinguishable from the noise, this is due to the tapered field distribution in the H plane at the horn aperture. With the waveguides still in the vertical configuration the separation distance was increased to 30 mm and again the low levels of crosstalk falls below the noise threshold.

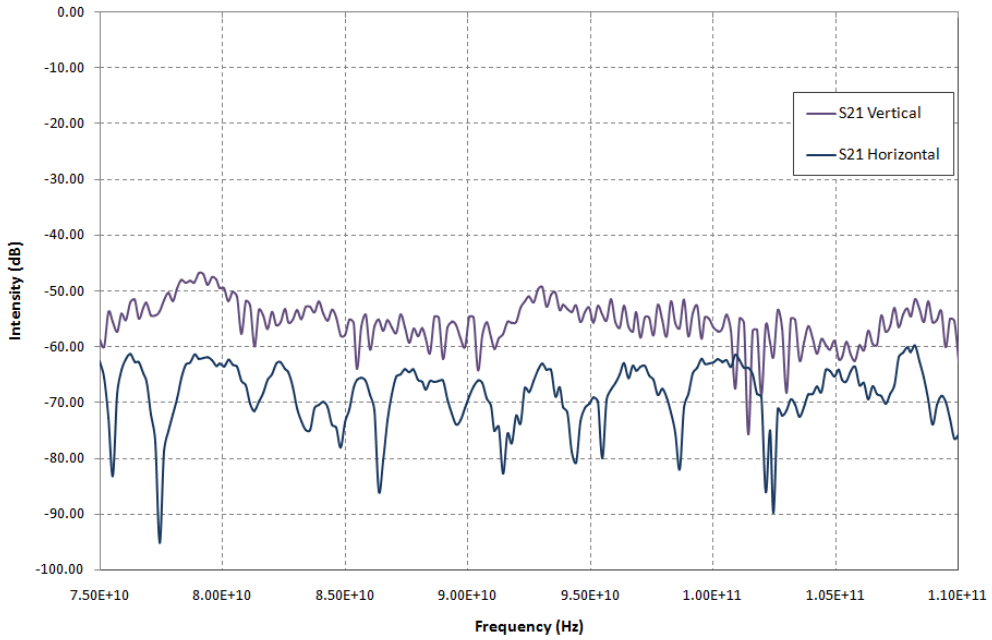

Figure 5.16 ***Experimentally measured crosstalk between two identical pyramidal horns with a 3mm gap between apertures in a vertical configuration (purple line) and a horizontal configuration (blue line)***

The crosstalk between two identical corrugated horns was analysed in a similar way to the pyramidal horns above. The horns are designed to operate over the 75 GHz to 110 GHz waveband, with an aperture radius of 7.13 mm, waveguide radius of 1.53 mm, length 64.8 mm and 81 corrugations. The S_{21} was measured with the horns in both horizontal and vertical orientations, with a minimum separation distance of 4.5

mm (due to the wall thickness) and then increased to 30 mm and 50 mm. In each case, regardless of orientation, noise was too high for crosstalk levels to be measured, due to the horns high directionality, symmetrical beam pattern and low side lobe structure, thus making them desirable candidates for high performance arrays.

5.5 SAFARI crosstalk

A single isolated SAFARI horn was discussed in section 4.4, the geometry of which can be seen in figure 5.17. The SAFARI horn antennas have a square aperture and are essentially two flared square waveguide sections with differing flare angles coupled together. The horn array is made by wire cutting the negative of the feedhorn array on an aluminium mandrel, copper is electroformed around the mandrel and the mandrel can then be chemically etched from the electroformed horns leaving the feedhorn array, thus the mandrel is destroyed and can only be used once.

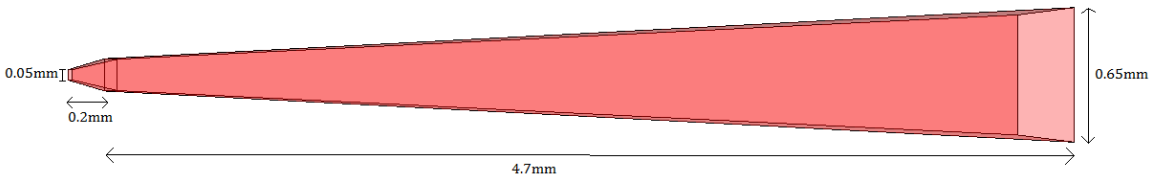

Figure 5.17 Geometry of the SAFARI S-band horn antenna

The width of the horn aperture is 0.65 mm. At the entrance to the array each aperture is separated by a distance of 0.19 mm this is determined by the cutting wire diameter used to cut the mandrel and is a fundamental limit on the entrance aperture fill factor. Although work is underway by the RAL space/Cardiff who are investigating the addition of a tri-angular profile grid to be separately fabricated and placed at the array aperture, this will minimise the distance between horn apertures while also adding length to the horn, this is still in the testing stage. Each antenna in the array is coupled to a cavity with a TES absorber inside, with each absorber constituting a single pixel. The goal is to efficiently couple incident radiation to the TES detectors.

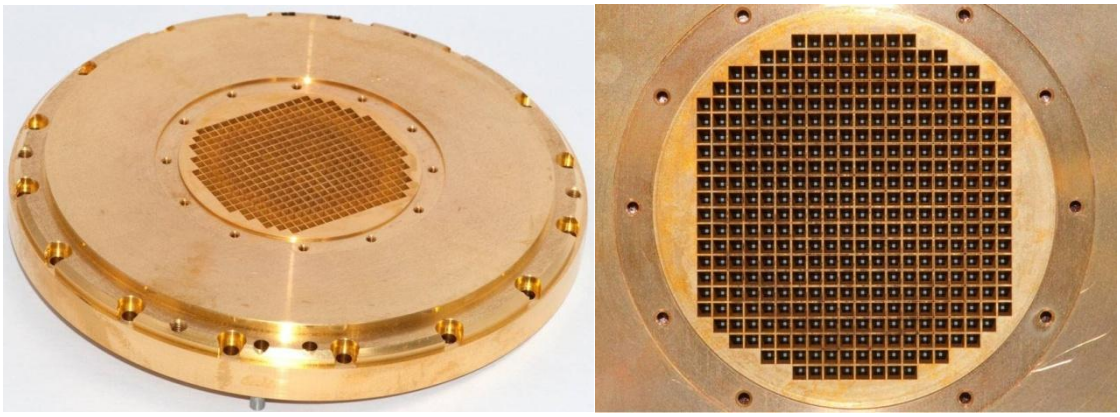

Figure 5.18 *An example of the SAFARI horn array [Griffin Technical note to ESA]*

At the array entrance incident radiation is coupled to each antenna but as was described is section 5.1 mutual coupling causes some of the intended radiation for one horn to be scattered and received by its neighbouring horn. Two SAFARI horns were modelled side by side with this 0.19 mm distance between them, as shown in figure 5.19, both horns radiate to free space. The S_{21} in this model refers to the power received at port 2 (placed at the throat of horn two) due to a signal transmitted at port one (at the throat of horn one), this is the crosstalk between the two horns.

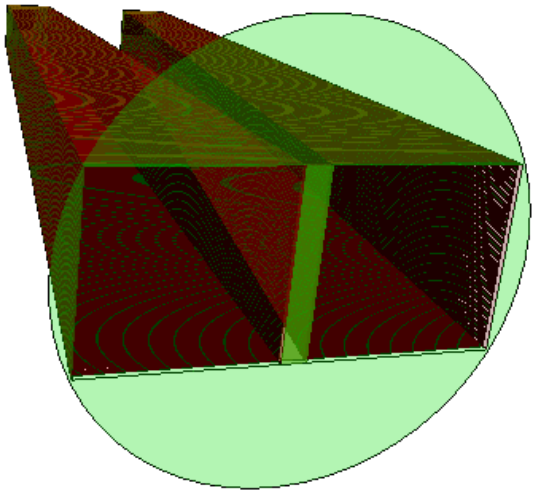

Figure 5.19 *SAFARI S-band horns modelled as part of an array in µWW*

Over the 4.285 - 5.0 THz waveband the crosstalk levels of the TE_{10} and TE_{01} modes are shown in figure 5.20. Crosstalk between higher order modes is shown in figure 5.21.

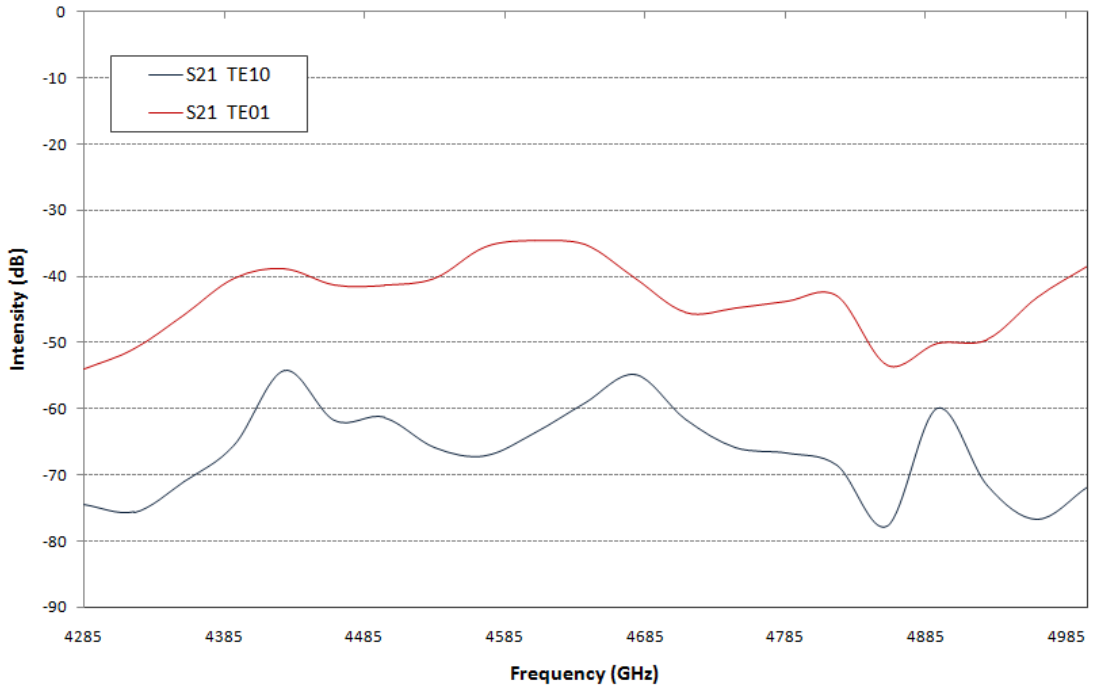

Figure 5.20 ***TE_{10} and TE_{01} mode crosstalk within the SAFARI array***

The TE_{01} mode has a similar field distribution to the TE_{10} mode but in the opposite polarisations - it is tapered in the E-plane but has a uniform distribution in the H-plane. Thus the results seen in figure 5.20 follow on from those investigated in the preceding sections - the increased levels of crosstalk power between the TE_{10} mode are due to its aperture field distribution and orientation within the array. Other propagating modes have lower contributions and the dominant mode contributes most crosstalk power. The return loss or the S_{11} for the horn itself is more significant in terms of reflected levels of power. Figure 5.21 shows extremely low levels of crosstalk power ($< -300\ dB$) between scattered higher order modes. The multi-moded propagation within the SAFARI horns proved computationally exhaustive, while symmetry settings could be used to reduce the computational load these symmetry settings also eliminated the higher order modes that were of interest. While crosstalk results were produced over the lower frequency end of the spectrum. The high operating frequencies and multi-moded propagation proved computationally unfeasible within µWW without the use of a much more powerful computer.

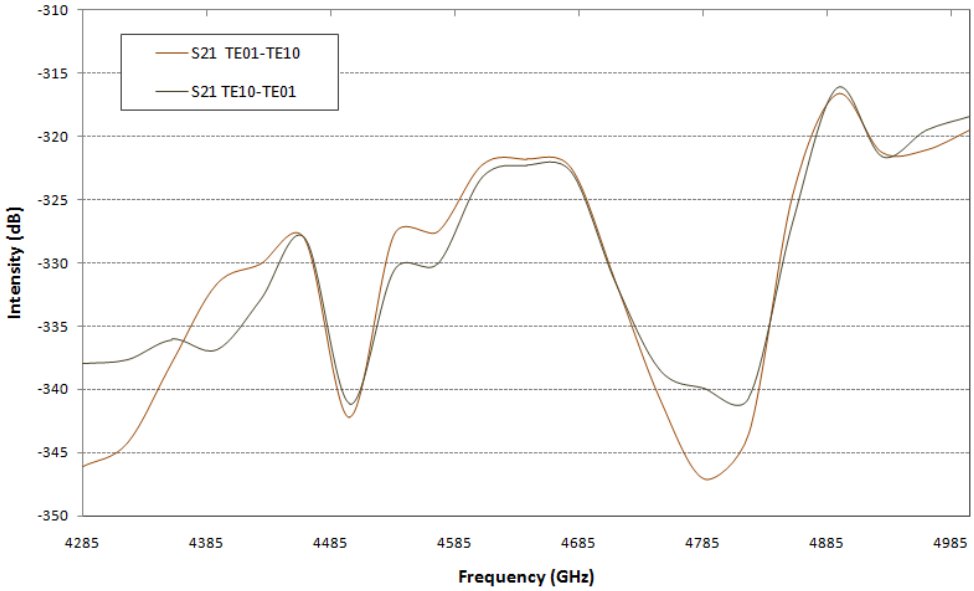

Figure 5.21 ***Crosstalk between scattered higher order modes in the SAFARI array***

5.6 Conclusion

This chapter has dealt with the analysis of mutual coupling or crosstalk between elements of an array. This coupling between array elements was demonstrated first within simple waveguide structures and the effect on the levels of crosstalk power in relation to the waveguide orientation were investigated and found to be effected by the field at the aperture, this and the crosstalk levels of power in relation to the separation distance were discussed for both circular and rectangular apertures. The analysis was then extended to VNA measurements of crosstalk between two standard WR-10 waveguides as the separation distance was increased, as expected crosstalk levels decreased and the finite integration technique used within CST was found to accurately reproduce these findings. The effects of orientation on the measurement of crosstalk levels between two single moded pyramidal horns was found to follow on from that discussed earlier in which due to the tapered field distribution at the aperture crosstalk is seen to increase with the horns in a vertical configuration. Finally the crosstalk between two SAFARI horns was analysed. Low levels of power leakage between adjacent horns was observed and had a much smaller value than the inherent S_{11} or return loss value within the horn structure itself. As the horn antenna is an inherently directional structure the amount of power that a neighbouring horn will feel is low between horn apertures.

CHAPTER 6

Multiple Reflections in Quasi-optical systems

6.1 Introduction

Partial reflections and standing waves occur within quasi-optical systems when signal is reflected off a component surface back along the optical path. The reflected signal has the potential to be reflected several times before reaching the detector where a superposition of signals is detected, that may be constructively or destructively interfering depending on the phase difference, and a modulation of the signal is observed. They are a common occurrence in quasi-optical systems particularly those with on-axis components such as lenses or dielectrics. Two horns facing each other aperture to aperture coupled either via intermediate optics or free space will exhibit standing wave effects. It is the latter, coupling via free space and also within closed cavities that is the subject of this chapter. Partial reflections potentially cause the return loss (S_{11}) at the throat of a horn to be higher while in systems such as high resolution spectral line receivers in the terahertz frequency range, reflections cause a baseline ripple on the spectra that is difficult to distinguish from wide lines [Murphy 2002] which must be accounted for at the calibration stage.

Firstly two horns aperture to aperture with no free space gap, so as to form a closed cavity, are investigated. Such a cavity will exhibit a high Q factor. A high Q factor indicates a low rate of energy loss relative to stored energy - much of the power is trapped within the system, the standing wave effects are prominent with sharp peaks. With the introduction of free space between the horns the system becomes a lower Q cavity as not all power is trapped within the system. Such systems are common in quasi-optics, such as where a second scanning horn may be used for near field measurements.

6.2.1 Multiple reflections within a corrugated cavity

Two horns with the same aperture dimensions placed aperture to aperture effectively form a closed cavity, with both horns transmitting and receiving radiation at the throat of the horn there are many complex multiple reflections occurring within the cavity or the tapered flares of both horns. A cavity formed by horn antennas was analysed experimentally using the VNA for both corrugated and pyramidal horns and compared against modelled results of the same set up, with the aim to see if these complex multiple reflections occurring within the cavity can accurately be predicted in models. µWW and SCATTER were used to model the cavity, both use the well known mode matching technique described in section 2.4 but were developed independently, this provides verification to the mode matching code developed at NUI Maynooth. The analysis of multiple reflections between horns was extended to the case where the horn apertures were moved apart so they are no longer touching and the radiation from one horn is coupled to the next horn via free space, this is described in the following section.

Firstly a cavity formed by two identical corrugated horn antenna placed aperture to aperture was investigated. The corrugated horns are designed to operate over the 75 - 110 GHz waveband with dimensions of length 64.8mm, aperture radius 7.1345 mm and throat radius 1.535 mm. The corrugated horns used in the VNA measurements are fed by a standard WR-10 waveguide coupled to the throat of the conical corrugated horn antenna via a transition region. For the purposes of modelling this transition to a rectangular waveguide was unable to be included and the horns are fed by single moded conical waveguides. An excitation signal is provided at the throat of each horn. The model assumes each section of the corrugated horn (corrugation/flared section) is replaced by a uniform section of waveguide, overall the profile of a single horn increases from throat to aperture, the profile is then reversed at the aperture of the first horn with the profile now decreasing from aperture to throat of the second horn to form the closed cavity model, illustrated in figure 6.1. There is a perfect transition between the apertures of the two horns with no leakage to free space (this was not entirely possible in measurements).

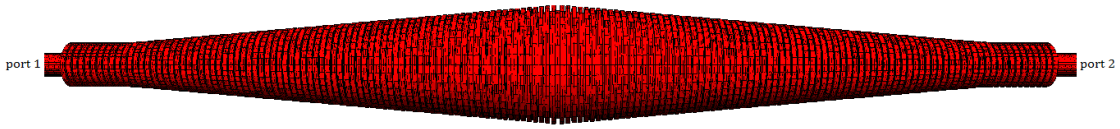

Figure 6.1 ***Two corrugated horn antennas aperture to aperture forming a closed cavity modelled in Microwave Wizard.***

The scattering matrix formulation of the mode matching technique provides a full multi-moded description of the internal behaviour of the cavity. Information about forward and backward travelling radiation is contained within scattering matrices describing each section, the matrices describe the scattering of power between adjacent modes within the cavity. The scattering matrices are then cascaded together to give the transmission (S_{21} and S_{12}) and reflection (S_{11} and S_{22}) properties of the entire cavity. In the SCATTER model 40 modes (20 TE and 20 TM) were used in the analysis and similarly 40 modes were used in the µWW model. Comparisons of the reflection and transmission properties of the cavity obtained using both mode matching models are shown in the following figures. It can be seen that although the precise details in the standing wave profile predicted by both models are not in exact agreement there is in fact good agreement between the levels of reflected and transmitted power in both of the mode matching models of the cavity. The S_{11} and S_{22} parameters shown in figures 6.2 and 6.3 respectively display very similar characteristics in both models due to the symmetry of the cavity. As µWW automatically assumes $S_{21} = S_{12}$ due to the symmetry of the system only the S_{21} parameter is calculated within µWW and shown here for both models in figure 6.4.

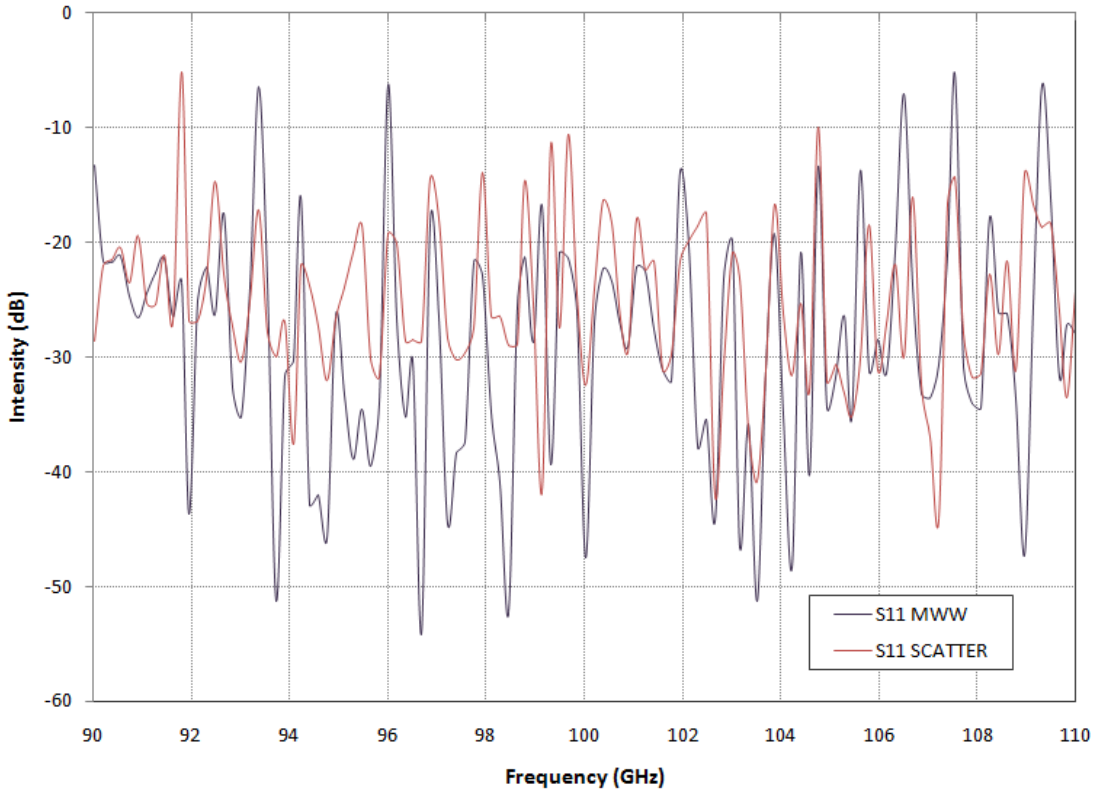

Figure 6.2 S_{11} *reflection properties at port 1 of the corrugated horn cavity modelled in both µWW (blue line) and SCATTER (red line)*

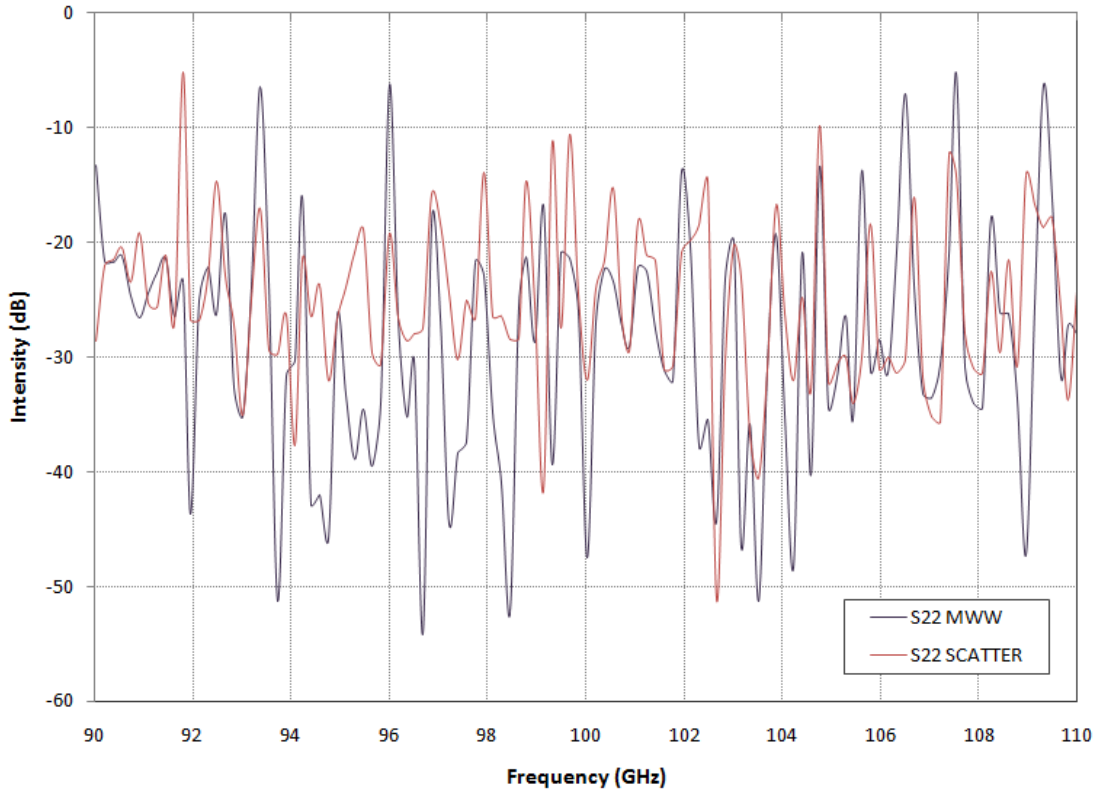

Figure 6.3 S_{22} *reflection properties at port 2 of the corrugated horn cavity modelled in both µWW and SCATTER*

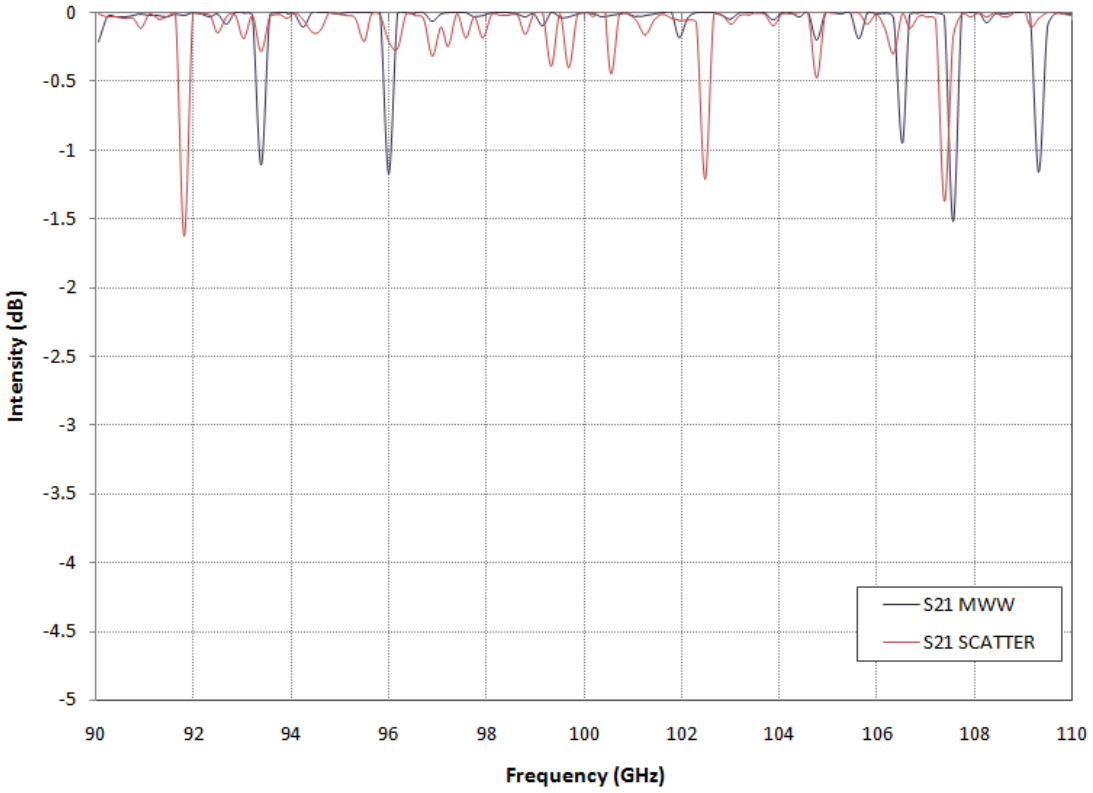

Figure 6.4 ***S_{21} transmission properties of the corrugated horn cavity modelled in both µWW and SCATTER***

It can be concluded that the two independent techniques do predict similar levels of behaviour. The large spectral features observed across the W band are indicative of a high Q cavity where the resonant dips in transmission are sharp and deep suggesting it is a highly resonant structure with lots of trapped power and complex interaction between reflected and transmitted components.

Using the Vector Network Analyser in the laboratory the reflection and transmission properties of the corrugated horn cavity were investigated experimentally. The assumption is made that the model or geometry file describing the horn in the model above is accurate and describes well the as built horn. In the model the waveguide taper from WR-10 rectangular waveguide to circular is not included but is present in the cavity composed of two horns in the lab. Head one of the VNA feeds the throat of horn one (this can be thought of as the transmitter) and head two feeds the throat of horn two (the detector) so the $S_{21}(= S_{12})$ parameter is the transmitted power through the system, same as with the models or simulations above. The results of measured versus modelled are shown in figures 6.5 - 6.7. Again very good agreement between the levels of reflected power can be seen in figures 6.5

and 6.6 for both measured and modelled S_{11} and S_{22} parameters even though the exact profile of the features do not agree entirely. The measured transmission properties of the cavity shown in figure 6.7 show some agreement with the modelled levels although the measured S_{21} is noticeably ~ 0.5 dB lower than the modelled predictions. This is believed to be due to problems in aligning the apertures of the horn exactly in measurements and some power may of leaked out at the interface, while the transition from aperture to aperture was modelled perfectly without losses in both models. The model predicts a number of resonances (transmission dips) across the band which are reproduced in the measurements . The locations of these resonances are not simulated correctly - precise calibration of the VNA cannot be guaranteed also a complete model with waveguide transition may affect the resonant structure profile.

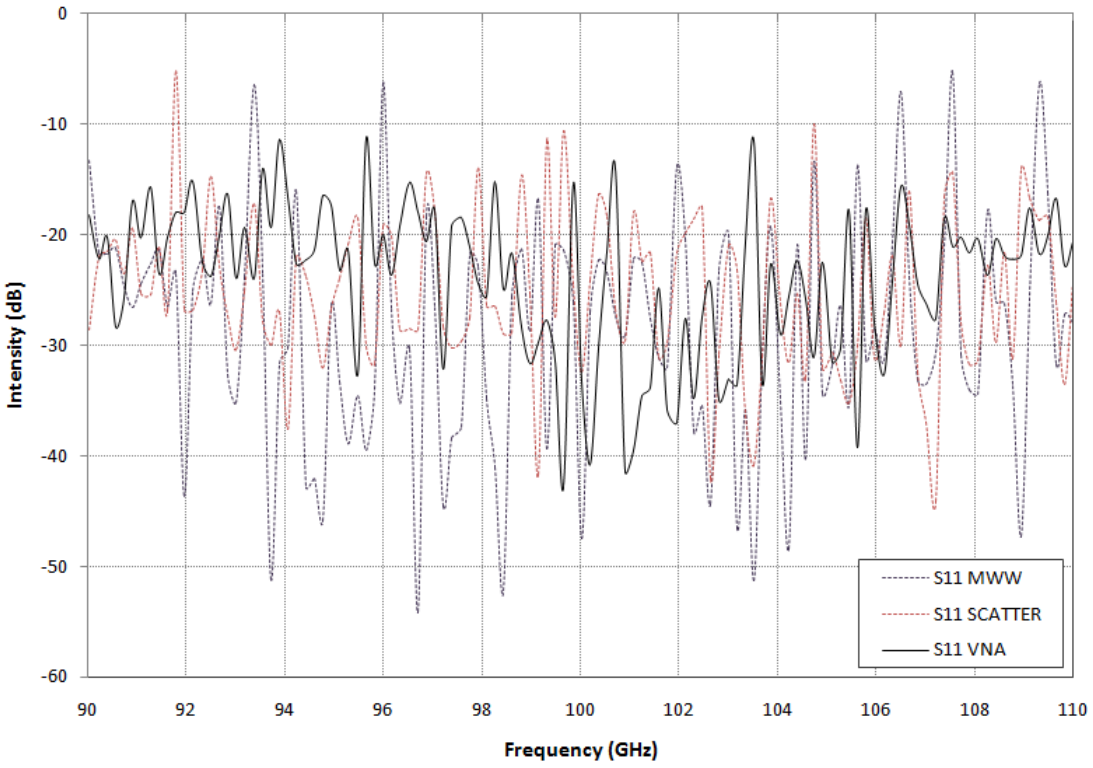

Figure 6.5 ***S_{11} reflection properties at port 1 of the corrugated cavity, measured (solid line) versus modelled (dotted lines)***

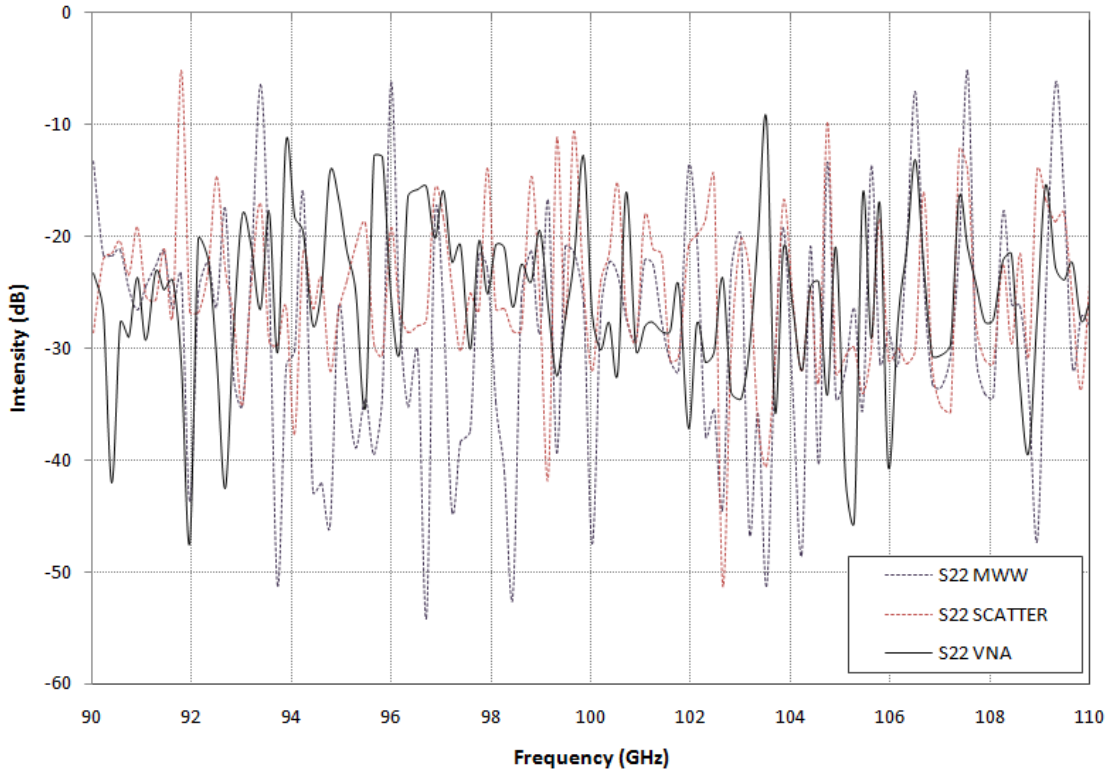

Figure 6.6 ***S_{22} reflection properties at port 2 of the corrugated cavity, measured (solid line) versus modelled (dotted lines)***

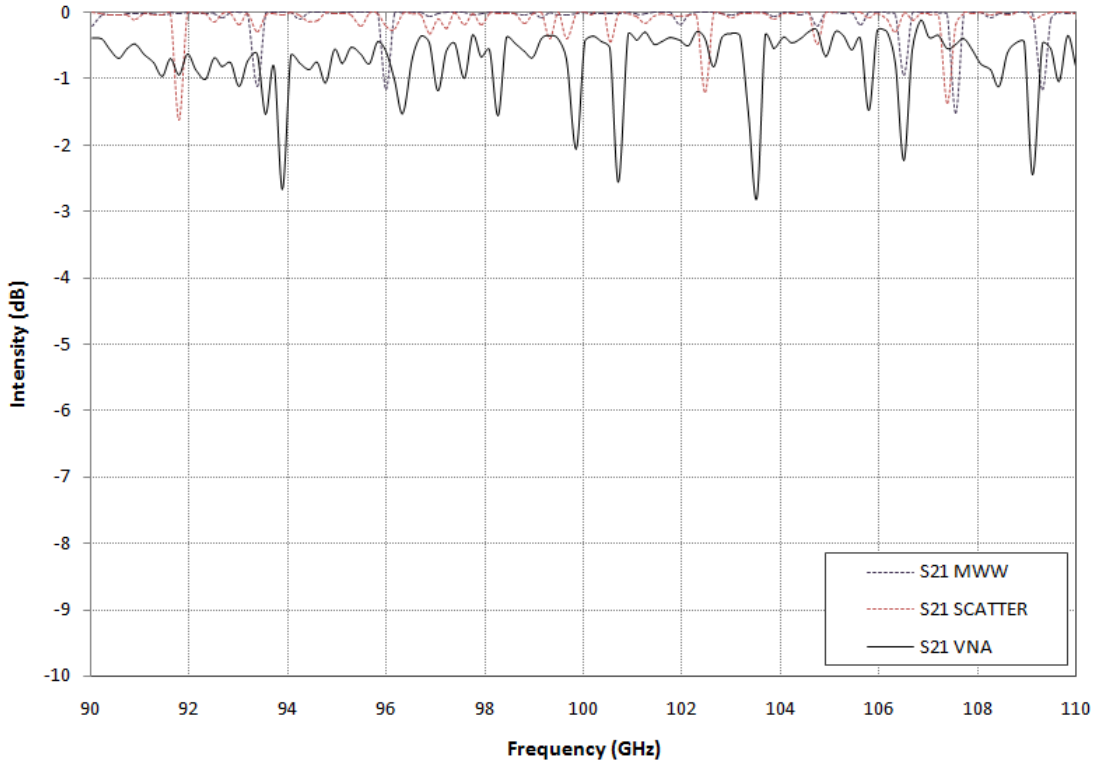

Figure 6.7 ***S_{21} transmission properties of the corrugated cavity, measured (solid line) versus modelled (dotted lines)***

6.2.2 Pyramidal horn cavity

Two identical pyramidal horns of dimensions A = 27 mm, B = 20 mm and slant length 63.5 mm fed by a WR-10 waveguide of length 11.2mm designed to operate over the 75 - 110 GHz waveband, whose far-field patterns were analysed previously in chapter 4 using both GBMA and the mode matching technique, where placed aperture to aperture so as to form a closed cavity as with the corrugated horns in section 6.2. Multiple reflections within the system were analysed both experimentally using the VNA and theoretically with mode matching models.

As was mentioned in chapter 4 the analysis of pyramidal horns within µWW is computationally exhaustive and so a full analysis of the transmission and reflection properties of a cavity formed by two pyramidal horns was computationally unfeasible due to memory constraints. The system was simplified to a one port system in which port one feeds the waveguide at the throat of horn one while the waveguide of horn two is terminated by use of a shorted waveguide, all power is theoretically trapped within the cavity. A comparison of the measured and modelled results is shown in figure 6.8. As in the preceding sections similar trends in the results are seen, with the µWW mode matching model accurately predicting the levels of reflected power although the exact profile is not reproduced but are representative overall.

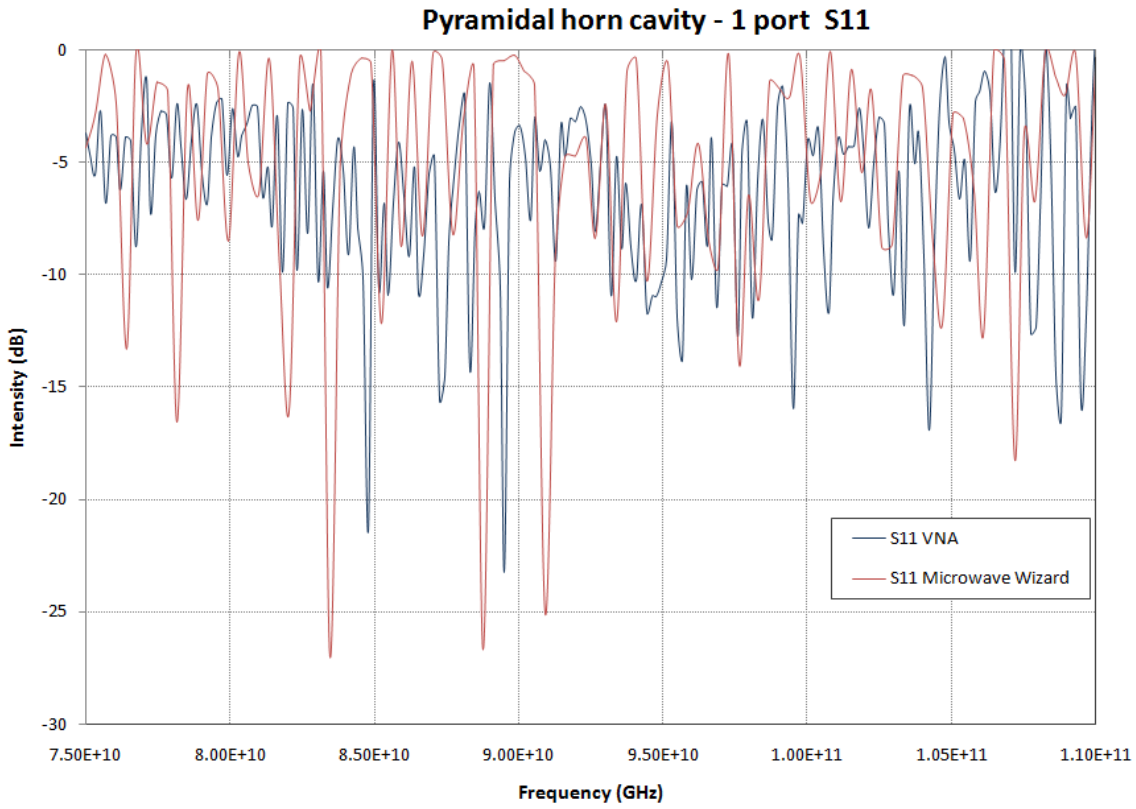

Figure 6.8 ***Power reflected at the port of a cavity formed by pyramidal horns and a shorted waveguide.***

6.3 Reflections between corrugated horns coupled via free space

The analysis of multiple reflections between corrugated horns facing each other aperture to aperture was then extended by introducing free space between the horn apertures as shown in figure 6.9. Radiation propagates through horn one (left to right) after leaving the aperture of the horn the wave is no longer confined and due to the spreading of the beam not all transmitted power is received at the aperture of horn two and subsequently the detector at the throat of horn two. Compared to the situation above the levels of power coupling will be lower due to the loss of radiation into free space and so we expect to see a lower Q cavity existing between the horns as not as much power is trapped. Vice versa if horn two is transmitting with horn one receiving the same is true. The power coupling between the throat of each horn (S_{21}) is what is of interest here for various aperture separation distances. Such systems comprising of two horn antenna facing each other are commonly used in quasi-optics such as in near field measurements of horn antenna beam characteristics using a scanning horn.

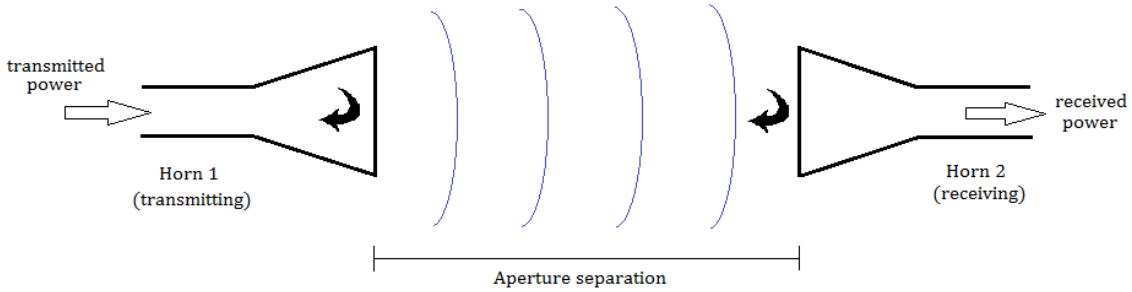

Figure 6.9 ***Illustration of two horns facing each other with radiation transmitted from one horn coupled to the receiving horn via free space***

A mode matching model of the set up is no longer adequate at describing the system as the propagation through free space is not described in the mode matching model. Instead a model merging the techniques of mode matching and Gaussian beam mode analysis was used. The internal electromagnetic behaviour of the horn is still described in the same way as before with the power scattering between modes within the horn described by scattering matrices cascaded together to give the overall transmission and reflection properties of the horn, now however at the aperture of the horn the waveguide modes are transformed to free space Gaussian modes that propagate through free space before being transformed back at the aperture of horn two to waveguide modes where the mode matching technique is again applied to the propagation within horn two, a detailed description of the theory can be found in [Trappe 2005]. The mode matching technique provides an accurate description of the field at the aperture of the horn in terms of TE and TM waveguide modes, in the plane of the aperture the waveguide modes are transformed to Gaussian modes by use of a transformation matrix that requires the computation of overlap integrals. The electric field at the aperture written in terms of TE and TM modes can be given in cylindrical coordinates by [Murphy 2002]

$$e_{1l}^{TE} = \frac{J_0\left(\frac{p'_{1l}r}{a}\right)i + J_2\left(\frac{p'_{1l}r}{a}\right)[\cos 2\phi i + \sin 2\phi j]}{\sqrt{2\pi a^2\left(J_1\left(\frac{p'_{1l}r}{a}\right)^2 - J_2\left(\frac{p'_{1l}r}{a}\right)^2\right)}} \tag{6.3.1}$$

$$e_{1l}^{TM} = \frac{J_0\left(\frac{p_{1l}r}{a}\right)i + J_2\left(\frac{p_{1l}r}{a}\right)[\cos 2\phi i + \sin 2\phi j]}{\sqrt{2\pi a^2\left(J_2\left(\frac{p'_{1l}r}{a}\right)^2\right)}} \tag{6.3.2}$$

where p_{1l} is the *lth* zero of $J_1(z)$, p'_{1l} the *lth* zero of $J'_1(z)$ and a is the radius of the aperture. The modes are normalised so that $\int_A \left|e_l^{TE/TM}\right|^2 2\pi r dr$ is equal to unity. The associated Laguerre Gaussian mode set given by equation 6.3.3 are used to describe the free space modes due to the symmetry of the system. The waveguide modes of a conical horn will only couple to the associated Laguerre Gaussian modes of degree 0 and 2.

$$\begin{pmatrix}\psi_n^{\alpha,cos}(r,\phi)\\ \psi_n^{a,sin}(r,\phi)\end{pmatrix} = \psi(r,\phi)_n^{\alpha} exp\left((-ikz + i(2n+\alpha+1) \times arctan\left(\frac{\pi W^2}{\lambda R}\right)\begin{pmatrix}cos(\alpha\phi)\\ sin(\alpha\phi)\end{pmatrix}\right.$$

$$= \sqrt{\frac{2(2-\delta_{0n})n!}{\pi W^2(n+\alpha)!}}\left(\frac{2r^2}{W^2}\right)^{\frac{\alpha}{2}} L_n^{\alpha}\left(\frac{2r^2}{W^2}\right) exp\left(\frac{-r^2}{W^2}\right) exp\left(-ik\left[\frac{r^2}{2R}\right]\right)$$

$$\times exp\left(-ikz + i(2n+\alpha+1) arctan\left(\frac{\pi W^2}{\lambda R}\right)\begin{pmatrix}cos(\alpha\phi)\\ sin(\alpha\phi)\end{pmatrix}\right) \quad (6.3.3)$$

The beam radius *W* and phase radius of curvature *R* have their usual meanings (given in chapter 2), and $arctan\left(\frac{\pi W^2}{\lambda R}\right)$ is the zero order phase slippage. α is an integer representing the degree of the Laguerre polynomial. Each waveguide mode is transformed to the corresponding free space mode using

$$e_m^G = \sum_n T_{nm}^0 \psi_n^0 i + T_{nm}^2 \psi_n^2 \left[\cos 2\phi i + \sin 2\phi j\right] \quad (6.3.4)$$

where $T_{nm}^0 = \int_A (\psi_n^0 \hat{\imath})^* (e_m^G)\, r dr d\phi$ and $T_{nm}^2 = \int_A (\psi_n^2 \hat{n})^* (e_m^G)\, r dr d\phi$

$\hat{n}$ is the unit vector $\hat{n} = \cos 2\phi i + \sin 2\phi j$. The total electric field at the horn aperture in terms of Laguerre Gaussian modes is given by

$$e_{total} = \sum_n B_n^0 \psi_n^0 i + B_n^2 \psi_n^2 \left[\cos 2\phi i + \sin 2\phi j\right] \quad (6.3.5)$$

This gives the coefficients of the Laguerre modes of order 0 and 2, B^0 and B^2

$$B_m^0 = \sum_m T_{nm}^0 A_n \quad and \quad B_m^2 = \sum_m T_{nm}^2 A_n \quad (6.3.6)$$

In terms of a scattering matrix used in the mode matching technique the transformation to free space has the form

$$[S] = \begin{bmatrix} S_{11} & S_{12} \\ S_{21} & S_{22} \end{bmatrix} = \begin{bmatrix} 0 & T^+ \\ T & 0 \end{bmatrix} \quad (6.3.7)$$

T^+ is the conjugate of T. The transformation matrix $[T]$ is the $[S_{21}]$ matrix component of $[S]$ that transforms the modes at the aperture. When transforming the modes from Laguerre Gaussian to waveguide modes at the aperture of the second horn $[S_{12}] = [S_{21}]^{T^+}$. This model can be extended to describe more complex optical systems such as propagation through lenses, reflections from mirrors and truncation effects etc. as they can easily be incorporated into the Gaussian beam mode analysis by use of ABCD matrices.

Using the theory described above a model predicting the coupling between the transmitted power at the throat of horn one to the received power at the throat of horn two was achieved. Experimental measurements of the same system described by the model were taken using the VNA. With head two of the VNA which is feeding the second horn placed on a movable stage the separation distance between the horn apertures was able to be varied while keeping the horns well aligned. As the separation distance between apertures increases less and less power is expected to be coupled between the two horns as power is leaked into free space. Distances of 3mm, 10 mm and 20 mm were analysed and compared against the model, the results can be seen in figures 6.10 - 6.12. Again the levels of transmitted power are in good agreement in both the measured and modelled systems although the profiles of the standing wave effects are not in exact agreement. It has been shown in the analysis of both the closed cavity and the free space propagation between horns that while overall levels of reflected and transmitted power within systems where complex multiple reflections are taking place can be accurately reproduced using mode matching and GBMA techniques, exact details of the resonant features caused by multiple reflections within the system are not entirely reproducible by these models.

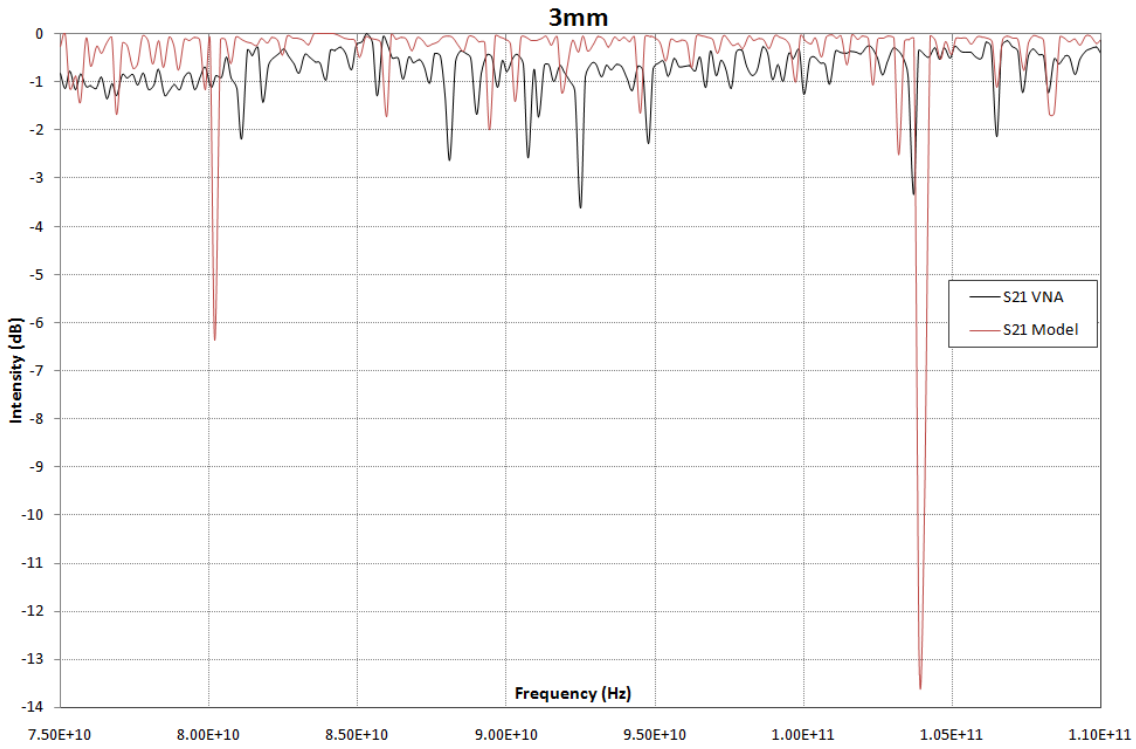

Figure 6.10 ***Modelled compared against measured coupled power between two corrugated horns illustrated in figure 6.8 separated by a distance of 3 mm over the 75-110 GHz range***

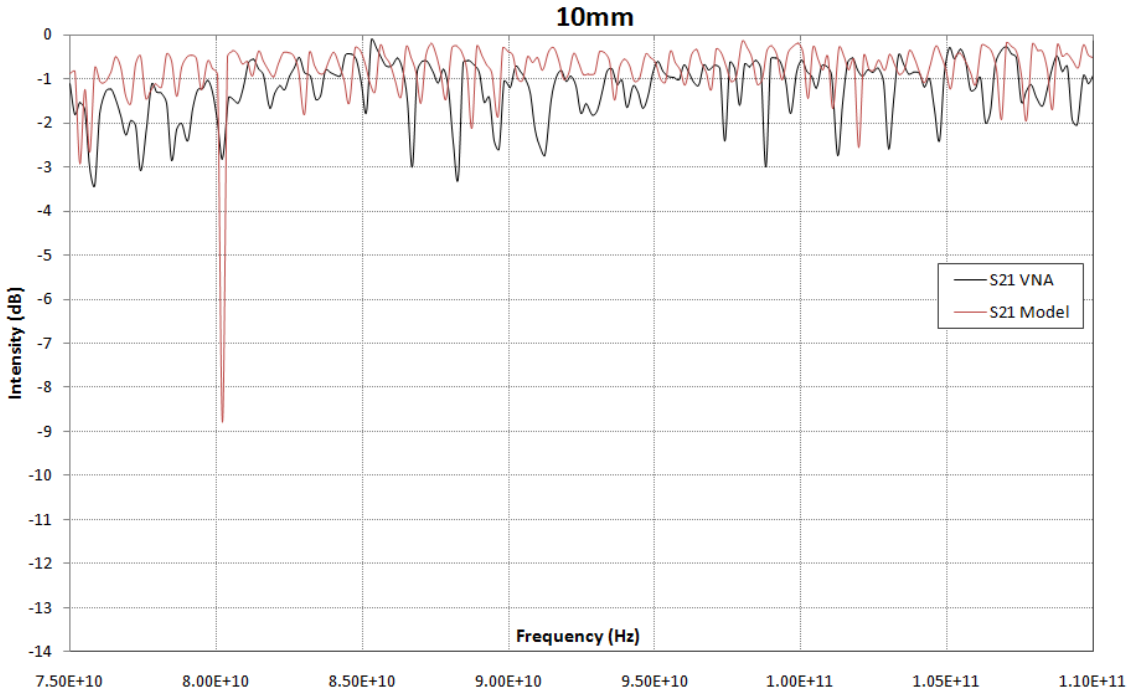

Figure 6.11 ***Coupled power between corrugated horns as the separation distance is increased to 10 mm, modelled versus measured results***

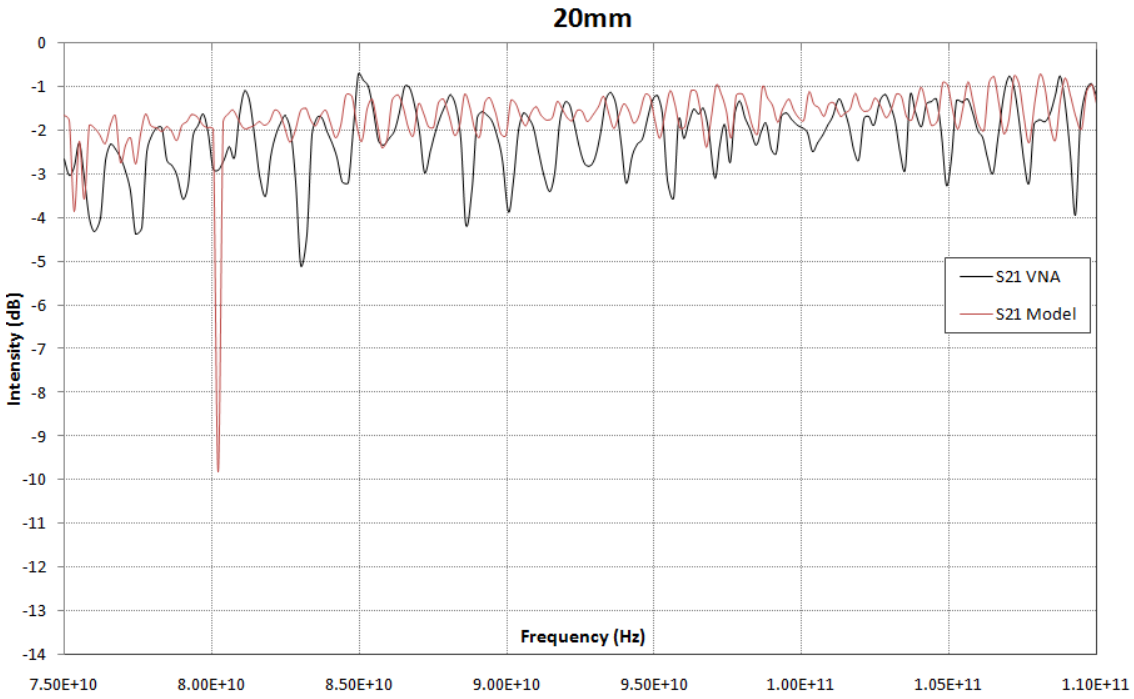

Figure 6.12 ***Coupled power between corrugated horns for a separation distance of 20 mm, modelled versus measured results***

6.4 Conclusion

In this chapter multiple reflections and standing wave effects common in many quasi-optical systems were analysed both experimentally and modelled. Firstly a high Q factor cavity, formed by horns placed aperture to aperture was analysed using the mode matching technique within both Microwave Wizard and SCATTER. Both models are based on the same underlying technique, the reflected and transmitted power levels at the cavity ports are in good agreement between the two models although it is demonstrated that the exact profile of the resonant features caused by multiple reflections within the cavity are not in exact agreement. The models were compared against VNA measurements taken in the laboratory. Again overall levels of reflected and transmitted power are in agreement although resonant feature locations are not exactly matched. It was concluded from the analysis that the complex interactions caused by multiple reflections within the cavity are difficult to predict within models due to their complex nature although the modes are representative overall. The subtle differences between the horn design and the actual manufactured horn which is

difficult to measure also seems to have an influence on the profile of the multiple reflection spectrum. The analysis was extended to standing wave effects within two corrugated horns coupled via free space for varying distances. The system has a lower Q factor as not all power in trapped in the system. The model describing the system uses the matching technique to describe propagation through the horn, at the aperture waveguide modes are transformed to free space modes that are propagated through free space and vice versa at the second horn aperture. Again the overall reflection and transmission power levels at the ports is reproducible within the model although the complex nature of the reflections makes the resonant features difficult to predict accurately.

6.5 Final conclusion

Throughout this thesis characteristics of horn antenna operating at terahertz frequencies as well as effects present within quasi-optical systems due to the antennas presence - crosstalk and multiple reflections, have been investigated using various methods and software packages. Conclusions have been drawn from the data regarding the suitability and accuracy of the various techniques to particular systems. The more precise electromagnetic analysis of the mode matching and finite integration techniques are found to produce accurate results although both are limited, due to their rigorous nature, by memory constraints on most computers. Microwave Wizard is particularly useful in the analysis of conical horns although runs into problems when applied to pyramidal structures due to their imposed boundary conditions. Gaussian beam mode analysis was found to be a good first approximation of results and computationally efficient.

As mentioned in the introduction chapter the terahertz waveband was once called the terahertz gap due to a lack of knowledge surrounding the area. The recent explosion of interest in the terahertz region due to its wide range of applications has lead to the need for the development of software packages that will accurately analyse these systems while borrowing techniques and software from millimetre and infrared regimes. This has lead to the wide range of methods for analysing such systems. Development of packages specifically designed for the analysis of terahertz systems, such as SCATTER are much needed as the application of packages designed to analyse millimetre wavelengths is not always computationally efficient.

References

Balinis C. A., Antenna theory, Analysis and design, Third edition, Wiley, 2005

Clarricoats P. J. D. and Olver A. D, Corrugated horns for microwave antennas, Peter Peregrinus (for IEEE), 1984

Clarricoats P. J. B. and Saha P. K., Propagation and radiation behaviour of corrugated feeds, Part 2 Corrugated conical horn feed, Proc. IEEE, 118, pp 187-199, 1971

Colgan R., Electromagnetic and quasi-optical modelling of horn antennas for FAR-IR space applications, PHD Thesis, 2001

Components. 2013. [ONLINE] Available at: http://www.radiometer-physics.de/rpg/html/Products_Components.html. [Accessed 25 October 2012].

COrE Mission - . 2013. COrE Mission - . [ONLINE] Available at: http://www.core-mission.org/. [Accessed 26 February 2013].

Corrugated Horns. 2013. [ONLINE] Available at: http://www.millimeterwave.com/corr.html. [Accessed 25 October 2012]

CST MICROWAVE STUDIO® 4 – Advanced Topics, 2002

CST Computer Simulation Technology . 2013. 3D EM Field Simulation. [ONLINE] Available at: http://www.cst.com. [Accessed 26 February 2013].

Gleeson E., Single and multi-moded corrugated horn design for cosmic microwave background experiments, PhD Thesis, 2004

Goldsmith P. F., Quasi-optical systems: Gaussian beam quasi-optical propagation and applications, IEEE Press, 1998

Griffin D., Technical Note 5 supplied to ESA as part of Technical Research Programme – Array Fabrication and Characterisation Agency Contract No. 22359/09/NL/CP “TES Spectrometer”

Haung Y., Boyle K., Antennas from theory to practice, Wiley, 2008

Herschel Science Centre. 2013. [ONLINE] Available at: http://www.herschel.esac.esa.int. [Accessed 26 February 2013].

Kraus J.D., Marhefka R. J., Antennas: For all applications, Third edition, McGraw-Hill, 2002

Kühn E. and Hombach V., Computer aided analysis of corrugated horns with axial or ring-loaded radial slots, IEE Conf. Proc., International conference on antennas and propagation, 1983

Lee C. S., Lee S.W., Chaung S. L., Plot of modal field distributions in rectangular and circular waveguides, IEEE Transactions on microwave theory and techniques, March 1985

Mauskopf P. D. et al., A TES focal plane array for SPICA-SAFARI, 21st International symposium on space terahertz technology, Oxford, March, 2010

Mician. 2013. Waves are our business | Mician. [ONLINE] Available at: http://www.mician.com. [Accessed 26 February 2013].

Murphy J. A., Aperture efficiencies of large axisymmetric reflector antennas fed by conical horns, IEEE Transactions on antennas and propagation, 36, No.4, April 1988

Murphy J. A. and Egan A., Examples of Fresnel diffraction using Gaussian modes, Eur. J, Phys,. 14, pp 121-127, 1992

Murphy J. A., Trappe N., Withington S., Gaussian beam mode analysis of partial reflections in simple quasi-optical systems fed by horn antennas, 2002

Olver A. D. et al, Microwave horns and feeds, IEEE press, 1994

Planck. 2013. ESA Science and technology: Planck. [ONLINE] Available at: http://www.planck.esa.int. [Accessed 26 February 2013].

Q-par. 2013. Lightweight Antennas — Q-par. [ONLINE] Available at: http://www.q-par.com/products/horn-antennas/lightweight-antennas. [Accessed 25 October 2012].

Ramo S., Whinnery J. R., Van Duzer T., Fields and waves in communication electronics, Third edition, Wiley, New York, 1994

Rudge A. W., Milne K., Olver A. D., Knight, The hand book of antenna design, Volume 1, P., Peter Perigrinus Ltd, 1982

SPICA. 2013. ESA Science and Technology: SPICA. [ONLINE] Available at: http://sci.esa.int/spica. [Accessed 26 February 2013].

SPICA. 2013. JAXA website. [ONLINE] Available at: http://www.ir.isas.jaxa.jp /SPICA/SPICA_HP/ippan-4_English.html. [Accessed 26 February 2013].

SPICA assessment study report (SRE-2009-6). 2013. ESA Science & Technology: SPICA assessment study report (SRE-2009-6). [ONLINE] Available at: http://sci.esa.int/science-e/www/object/index.cfm?fobjectid=46024#. [Accessed 26 February 2013].

Stutzman W. L and Thiele G. A., Antenna theory and design, Third edition, 2012

Trappe N., Murphy J. A., Withington S., Jellema W., Gaussian Beam Mode Analysis of Standing Waves Between Two Coupled Corrugated Horns, Antennas and Propagation, IEEE Transactions on, 53, Issue 5, Page(s):1755 – 1761 May 2005.

White D., The development of efficient CAD software for terahertz optical design and analysis, PhD thesis, 2006

Wright. 2013. WSU THz-Ultrafast Photonics Website. [ONLINE] Available at: http://www.wright.edu/~jason.deibel/intro.htm. [Accessed 24 October 2012].

Wylde R., Millimetre wave Gaussian beam mode optics and corrugated feed horns, IEEE, 1984